学位論文

Development of remote sensing algorithm for atmospheric aerosol properties by multi-wavelength multi-pixel method

(多波長マルチピクセル法による

大気エアロゾルのリモートセンシングアルゴリズムの開発)

平成 26 年 7 月　博士（理学）申請

東京大学大学院理学系研究科

地球惑星科学専攻

橋本　真喜子

Abstract

Aerosol particle or aerosol is a liquid or solid particle floating in the atmosphere, and affects the earth's radiation budget through scattering and absorbing solar radiation. The satellite remote sensing is one of aerosol measurement methods, and has an advantage of monitoring the global aerosol properties for long period. It is difficult, however, to retrieve the properties of optically thin aerosol layers, because the observation is strongly affected by surface reflectance. In particular, there are many types of surface that also change in time over land, and this surface variation makes it difficult to correct the effect of surface reflectance. After development of a correction method of surface albedo by Kaufman et al., (1989,1997b), aerosol properties such as aerosol optical thickness (AOT) or Ångstrom exponent (AE) over land have become retrieved (Remer et al., 2005). In the 2000s, aerosol retrieval methods in desert region were developed using near UV to blue visible wavelengths where dust and carbonaceous aerosols have a strong light absorption (Hsu et al., 2004, 2006; Fukuda et al., 2013). However, there remains a challenging problem that is the case of spatially heterogeneous surface such as urban area, while urban area is a source region of air pollutants or anthropogenic aerosols (Chu et al., 2002; Chu et al., 2003; Hermandez et al., 2007). Air pollution particles have not only scattering but also absorbing of solar light and affect the earth's climate and public health, so understanding of urban aerosol properties is an important task. Even on global scale, the earth's surface is never homogeneous with various soil types, vegetation covers, etc over land and with white caps, sun-glint, suspended ocean particles, etc over ocean. It is, therefore, useful to develop a flexible satellite algorithm for aerosol retrieval that can work over general types of the earth's surface.

For this purpose, I have developed a new satellite remote sensing algorithm to retrieve the aerosol optical characteristics using multi-wavelength and multi-pixel information of satellite imagers. In this algorithm, a new inversion scheme was established by combining the MAP method (Maximum a posteriori method, Rodgers, 2000) with the Phillips-Twomey method (Phillips, 1962; Twomey, 1963) to introduce a smoothing constraint to the state vector. Retrieved parameters in the algorithm are aerosol optical parameters, such as AOTs of fine mode and coarse mode (sea salt or dust) particles, a volume soot fraction in fine mode particles (SF), and ground surface albedo at each observed wavelength. I simultaneously retrieve all the parameters that characterize pixels in each of horizontal sub-domains consisting the target area under an assumption that aerosol parameters are slow functions of horizontal coordinates over the sub-domain compared to those of surface albedos. In the past studies, aerosol properties are generally retrieved pixel by pixel, and simultaneous analysis of multi-pixels has not been conducted yet. Furthermore, I constructed the

algorithm in a way to numerically solve the non-linear inverse problem by an iteration method to search the optimum solution in incorporation with a radiative transfer model without use of look-up table method (LUT) that are often used in satellite imager data analysis. Then, the algorithm has become flexible enough to treat various conditions of different aerosol properties and surface conditions without significant change of the code.

I conducted numerical simulations for the retrieval of aerosol properties and ground surface albedo for GOSAT/TANSO-CAI imager data to test the algorithm for several types of surface such as vegetation, desert, sea water, snow and urban-like. I assumed that urban-like surface is spatially heterogeneous surface, and that the other surfaces are uniform in the analysis region. The result of the experiment showed that AOTs of fine mode and coarse mode (dust), soot fraction (SF) and ground surface albedo are successfully retrieved within errors of 0.03, 0.05, 5% and 5%, respectively, in assumed urban-like region. This result indicates that the present method is superior to the pixel-by-pixel analysis for aerosol retrievals over spatially heterogeneous surface areas including high reflectance surface, such as urban areas that it was difficult to be analyzed by pixel by pixel methods.

Then, I applied this algorithm to GOSAT/TANSO-CAI imager data. I analyzed data in urban regions in the East coast of the United States (76-77°W/38.7-39.4°N) and in France (2.15-2.50°E/48.68-48.88°N). I compared retrieved and surface-observed AOTs at the CAI pixel closest to an AERONET (Aerosol Robotic Network) site in each region. Comparison at several sites in urban area indicated that AOTs retrieved by this method are in agreement with AERONET AOT with an error of ±0.066. As for light absorption by aerosols, I evaluated the single scattering albedo calculated from satellite-retrieved AOT and SF, and found that they showed a seasonal tendency consistent with that of AERONET-observed SSA and surface-measured BC concentration (Song et al., 2013) in summer and winter at Beijing. I have also tried simultaneous retrieval of clouds and aerosols, which also has not been done in the past. A case study found that the area of large optical thickness by cloud particles was consistent with that identified by human eyes from the RGB imagery.

By this new algorithm, it has become possible to retrieve AOT and an absorption parameter (SF) simultaneously in a spatially heterogeneous surface region composed of dark and bright surface areas, such as urban area where the aerosol estimation had been difficult. I like to validate the present algorithm through applying to more data from CAI for various types of surface conditions over the globe. I will also apply the algorithm to other satellite data, such as ADEOS-II/GLI and MODIS. Challenging work for global analysis is to speed up the computation by the algorithm by use of various technique such as neural-network and/or adjoint techniques. In

the future, several new satellites (GOSAT2/TANSO-CAI2, GCOM-C1/SGLI and HIMAWARI 8 and 9) with multi-angle and polarization measurement functions will be launched, so that it is also important to develop multi-angle and polarization algorithms to be applied to data from these future new satellites.

Acknowledgment

I would like to express my deepest gratitude to Prof. Teruyuki Nakajima of Atmosphere and Ocean Research Institute (AORI), the University of Tokyo, for his continuous guidance, invaluable suggestion and advice.

I also express my gratitude to Prof. Tamio Takamura of Center for Environmental Remote Sensing, Chiba University, Prof. Oleg Dubovik of Laboratoire d'Optique Amosphérique, Université des Sciences et Technologies de Lille, Dr. Monica Campanelli of Consiglio Nazionale delle Ricerche, Istituto Scienze dell'Atmosfera e del Clima, Dr. Huizheng Che of Key Laboratory of Atmospheric Chemistry (LAC), Institute of Atmospheric Composition, Chinese Academy of Meteorological Sciences (CAMS), CMA, Dr. Pradeep Khatri of Center for Environmental Remote Sensing, Chiba University, and Dr. G. Pandithurai of Centre for Climate Change Research Indian Institute of Tropical Meteorology.

I am grateful to Dr. Hideaki Takenaka of the University of Tokyo for providing segmentation data of observation, helpful advice and discussion. I am also grateful to Dr. Satoru Fukuda of the Japan Aerospace Exploration Agency (JAXA) for providing segmentation data of observation. I wish to express my gratitude to Dr. Daisuke Goto, Dr. Haruo Tsuruta, Dr. Toshiro Inoue and Dr. Junya Uchida for their helpful comments. I also thank laboratory and radiation group members for their advice.

GOSAT/TANSO-CAI imager data used in this study is provided by he Ministry of the Environment (MOE), the National Institute for Environmental Studies (NIES), and the Japan Aerospace Exploration Agency (JAXA). The ancillary data used in this study for OMI ozone amount are provided by Goddard Earth Sciences Data and Information Services Center (GES DISC); for surface pressure and water vapor amount by NCEP, for aerosol properties of ground based observation by AERONET NASA GSFC and SKYNET. Figures in this paper are produced by the Generic Mapping Tools (GMT) software, Grid Analysis and Display System (GrADS), and GNUPLOT.

I appreciate laboratory staffs for their kind support. I also thank all the members of AORI for providing the great environment for research. Finally, I give heartfelt thanks to my family for their support and understanding.

Contents

Chapter 1 General introduction

In this chapter, I present background and objective of this study.

1.1 Aerosol and its impact to the atmosphere

In the atmosphere, small liquid and solid particles are floating, and I call those *aerosol particles* or *aerosols*. The aerosols have a variety of sizes (10^{-3} to 10μm), shapes and compositions, and can be classified in natural and anthropogenic based on their origin. For example, yellow sand floating over East Asia in the springtime; smoke (mist and organic carbon or soot) from biomass burning and volcanic ash are natural aerosols; and black carbon (BC) or soot emitted from the combustion of fossil fuels such as industrial activities or diesel cars, and from cooking or fireplace are anthropogenic aerosols. Aerosols can also be classified in terms of their sizes, that is, in the fine particle and coarse particle. The aerosol particles often take a bimodal size distribution, of which one peak consists of fine mode particles and the other of coarse mode particles as shown in Fig. 1.1.1.

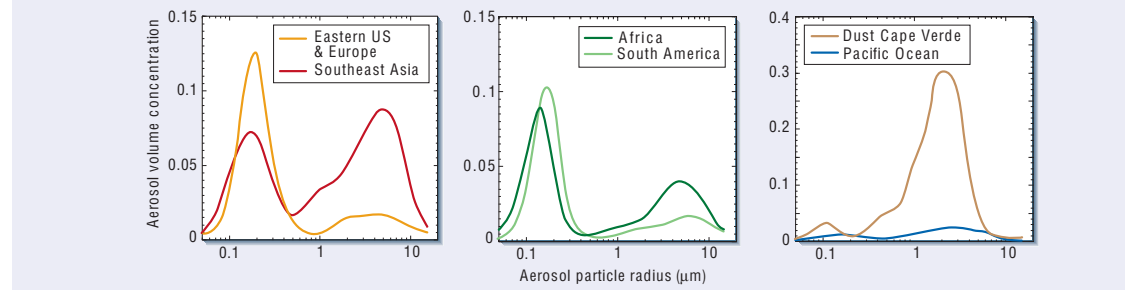

Analysis\Aerosol type	Regional pollution aerosol				Biomass burning			Dust	Oceanic
AERONET analysis	East. US	Europe	SE Asia	Cen. Am.	Boreal forest	Trop. forest	Savanna Africa–S.A.	Sahara–Saudi Arabia	Pacific Ocean
Time of the year	Jun–Sep		Jan–Apl	Jan–Dec		Jun–Nov		Jan–Dec	Jan–Dec
Average AOT	0.20		0.20	0.30	0.25–0.45		0.25–0.5	0.2–0.4	0.06
AOT_τ	94%		95%	90%	95%		92%	25%	67%
% absorption of AOT	3%	6%	12%		7%		12%	5%	2%

Figure 1.1.1 Regional variability of aerosols. The figure shows systematic multi-year measurements by the Aerosol Robotic Network (AERONET) and in situ measurement for four aerosol types. (1) Eastern United States & Europe, and southeast Asia (polluted area), (2) Africa and South America (biomass burning), (3) Atlantic Ocean (dust), (4) The Pacific Ocean (maritime aerosol). The unit of size distribution is $\mu m^3/\mu m^2$. (Kaufman et al., 2002)

Many of fine particles are originated by anthropogenic causes and are found downwind of populated region (i.e. urban area). On the other hand, many of coarse particles are found in desert or

ocean area, and are originated by natural causes (Kaufman et al., 2002; Dubovik et al., 2002). Polluted aerosols or urban aerosols include elemental carbon (called black carbon (BC), or soot) that accounts for light absorption of the aerosol. Generally, there is a tendency that the density of black carbon (or soot) is high in urban region rather than in the ocean or desert region (Kawamura, 2008).

The aerosol scatters and absorbs the solar light, and affects the energy budget of the earth. It is pointed out that the black carbon aerosol emitted from biomass burning and regional pollution exerts a significant global climate effect (Kaufman et al., 2002). Figure 1.1.2 shows the radiative forcing of climate between 1750 and 2011 from IPCC AR5 (2013).

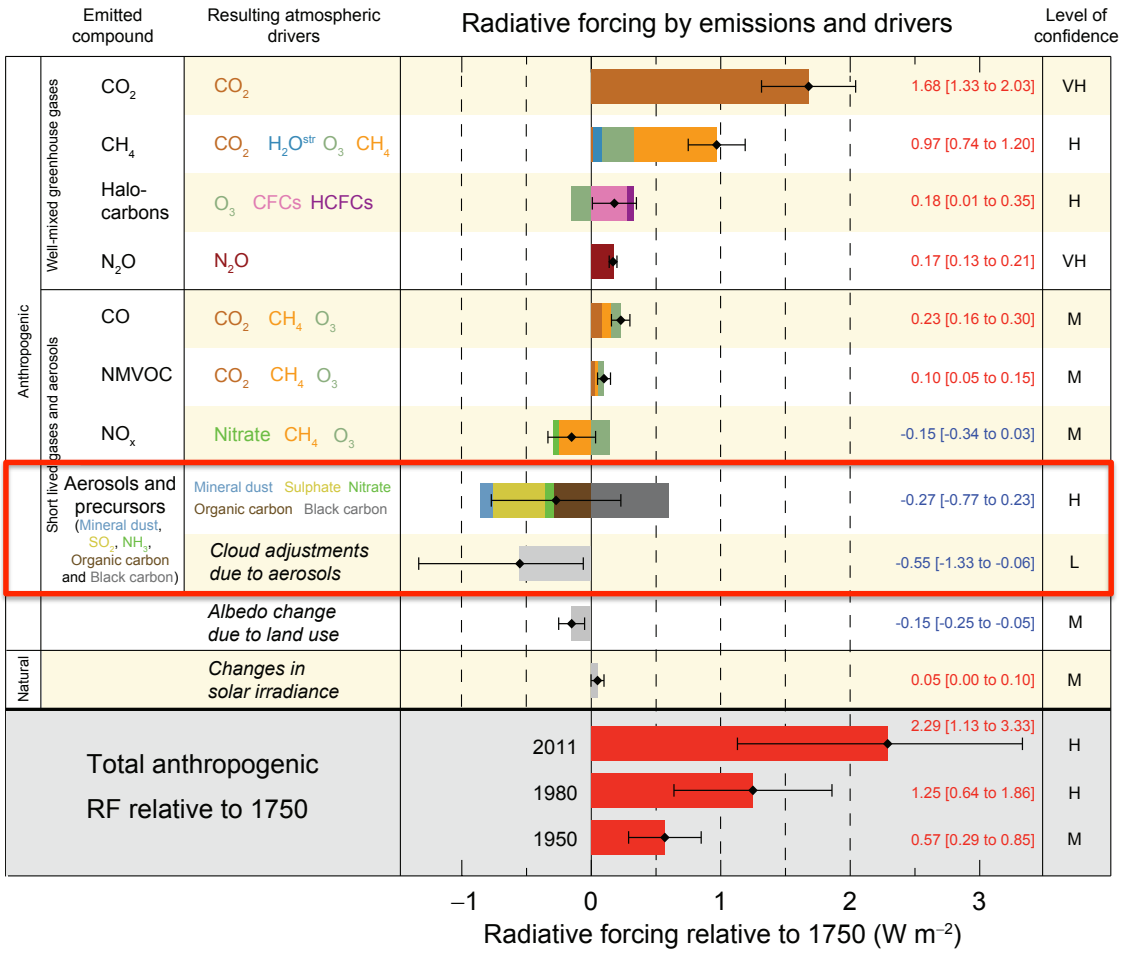

Fig. 1.1.2 Radiative forcing of climate between 1750 and 2011 (IPCC AR5, 2013). Added red square highlights aerosol direct and indirect effects.

IPCC AR5 (2013) reports "The total anthropogenic RF for 2011 relative to 1750 is 2.29 [1.13 to 3.33] W m^{-2}, and it has increased more rapidly since 1970 than during prior decades. The total anthropogenic RF best estimate for 2011 is 43% higher than that reported in AR4 for the year 2005.

This is caused by a combination of continued growth in most greenhouse gas concentrations and improved estimates of RF by aerosols indicating a weaker net cooling effect (negative RF)", and "The RF of the total aerosol effect in the atmosphere, which includes cloud adjustments due to aerosols, is –0.9 [–1.9 to −0.1] Wm^{-2}, and results from a negative forcing from most aerosols and a positive contribution from black carbon absorption of solar radiation. Aerosols and their interactions with clouds have offset a substantial portion of global mean forcing from well-mixed greenhouse gases. They continue to contribute the largest uncertainty to the total RF estimate."

To assess the impact of aerosols on the global climate, a long-term and global measurement approach is necessary, because aerosols vary widely from region to region. Remote sensing approaches, such as satellites and ground-based optical measurements, are effective in this regard, because it can observe column-integrated optical cross sections of aerosols in the atmosphere that are indispensable for evaluation of the radiative forcing of aerosols and, specifically, the satellite remote sensing can observe global aerosols.

Aerosol optical thickness (AOT, τ) and single scattering albedo (SSA, ω) are important parameter to assess the aerosol impact on the climate as defined as

$$\tau_{e,s,a} = \int_0^\infty \sigma_{e,s,a}(z)\,dz,\ \ \sigma_e = \int_0^\infty Q_e(x,m)\pi r^2 n(r)\,dr\,, \tag{1.1.1}$$

$$\omega = \sigma_s / \sigma_e\,, \tag{1.1.2}$$

where subscripts, e, s and a, denote extinction, scattering and absorption, respectively; σ_e, σ_s and σ_a are extinction, scattering and absorption coefficients; z is vertical height; Q_e is the Mie extinction efficiency factor given in terms of size parameter, x, and complex refractive index, m; r and $n(r)$ are the aerosol particle radius and number size distribution. The radiance (L_{TOA}) and apparent reflectance (R) of top of atmosphere (TOA) are approximately written in single scattering approximation as follows,

$$L_{\mathrm{TOA}}(\Theta) = \frac{\mu_0 F_0}{\pi}\frac{\omega}{4(\mu+\mu_0)}P(\Theta)\left\{1-\exp\left[-\tau\left(\frac{1}{\mu}+\frac{1}{\mu_0}\right)\right]\right\}, \tag{1.1.3}$$

$$R(\Theta) = \frac{\pi L(\Theta)}{\mu_0 F_0} = \frac{1}{4\mu\mu_0}\omega\cdot\tau\cdot P(\Theta)\,, \tag{1.1.4}$$

where Θ is the scattering angle, μ and μ_0 are cosines of satellite and solar zenith angles, respectively; F_0 is the extraterrestrial solar irradiance.

1.2 Overview of aerosol observation by satellites

There are several satellites monitoring aerosols from space. I show several satellite sensors that have been used to retrieve aerosol properties with their reported accuracy of AOT in Table 1.2.1 (Kaufman et al., 2002; IPCC AR4; Lee et al., 2009). α is Ångstrom exponent (AE) that is a parameter of aerosol particle size; AI (Aerosol Index) is an index for aerosol amount estimated by a UV absorption property of aerosol. Present retrieval accuracy of aerosol optical thickness (AOT, τ_{aer}) is reported as in a range of 5-30% (±0.05±0.2AOT) (Kaufman et al., 2002; Chu et al., 2003; Lee et al., 2009). SSA has not been retrieved globally.

Table 1.2.1 Several satellite sensors for retrieval of aerosol properties.

Satellite sensor	Operation Period	Number of bands (Wavelength μm)	Product	Accuracy of τ_{aer}
AVHRR	1979-present	5 (0.63,0.87,3.7,10.5,11.5)	τ_{aer}, α	10%, 3.6% (ocean)
TOMs	1979-present	6 (0.309-0.36)	AI, τ_{aer}	20~30%
ATSR-2/AATSR	1996-present	4 (0.47-0.86)	τ_{aer}, α	30%
SeaWiFS	1997-present	8 (0.765,0.865 for ocean, 0.41,0.67 for land)	τ_{aer}, α	5~10% (ocean)
MODIS	2000-present	12 (0.41-0.86)	τ_{aer}, α	±0.03±0.05τ_{aer}, (ocean) ±0.05±0.2τ_{aer}, (land)
OMI	2004-present	3 (0.27-0.5)	AI, τ_{aer}	30%
MISR	2000-present	4 (0.47-0.86)	τ_{aer}, α	10~20%
CALIPSO	2006-present	2 (0.532,1.064)	Aerosol vertical profile	-
POLDER-3	2005-present	8 (0.44-0.91)	τ_{aer}, α	30%
TANSO-CAI	2009-present	4 (0.38,0.674,0.87,1.6)	τ_{aer}	-

1.3 Historical background of satellite remote sensing for aerosols

Satellite remote sensing for aerosols utilizes the feature that aerosols noticeably scatter and absorb the sunlight around the visible spectral region. A satellite sensor observes backscattered sunlight reflection ($R_{satellite}$) which is a sum of contributions from the path radiance reflection ($R_{atmosphere}$) and the earth's surface reflection ($R_{surface}$),

$$R_{satellite} = R_{atmosphere} + R_{surface} . \quad (1.3.1)$$

Thus, satellite signals have to be corrected to remove surface reflectance before aerosol retrieval. Furthermore, there are many types or different reflectance surfaces on the earth, especially over land, and this fact makes aerosol retrieval from satellite be more difficult (Kaufman et al., 1987, 2001; Remer et al., 2005; Hsu et al., 2004).

The AVHRR (Advanced Very High Resolution Radiometer) and TOMS (the Total Ozone Mapping Spectrometer) series are pioneering satellites that have been observing aerosols. Aerosol information has been successfully derived from both sensors, such as aerosol optical thickness (AOT, τ) from AVHRR (Stow et al., 1997) and UV-absorbing aerosol index (AI) from TOMS (Herman et al., 1997).

First success retrieval of global aerosols using satellite data is over ocean (Stow at el., 1997; Higurashi and Nakajima., 1999), because the reflectance of the ocean surface is low and they could correct the capillary wave effect using a function of wind velocity to correct the ocean surface reflectance developed by Cox and Munk, (1954, 1956). Stow et al. (1997) retrieved Aerosol optical thickness (AOT) using channel 1 (visible) data of NOAA-11/AVHRR over ocean. Higrashi and Nakajima (1999) developed a two-channel method with a look-up table method (LUT) using NOAA-11/AVHRR data. They first retrieved Ångström exponent (AE), whish is an index of the aerosol particle size, and AOT at wavelength 500 nm over the global ocean simultaneously, as shown in Fig. 1.3.1. After that, they developed four-channel method, and classified aerosols into four types (sulfate, carbonaceous, mineral dust and sea salt) by size and absorption at blue wavelengths using SeaWiFS four-channel data (Higurashi and Nakajima, 2002). Their algorithm first classifies aerosol into small and large particle by two-channel method using channel-6 and -8 (the center wavelengths are 670 and 865 nm for the SeaWiFS sensor), then classified them into absorbing and non-absorbing aerosols using the difference in the apparent aerosol reflectances between channel 1 and 2 (the center wavelengths are 412 and 443 nm).

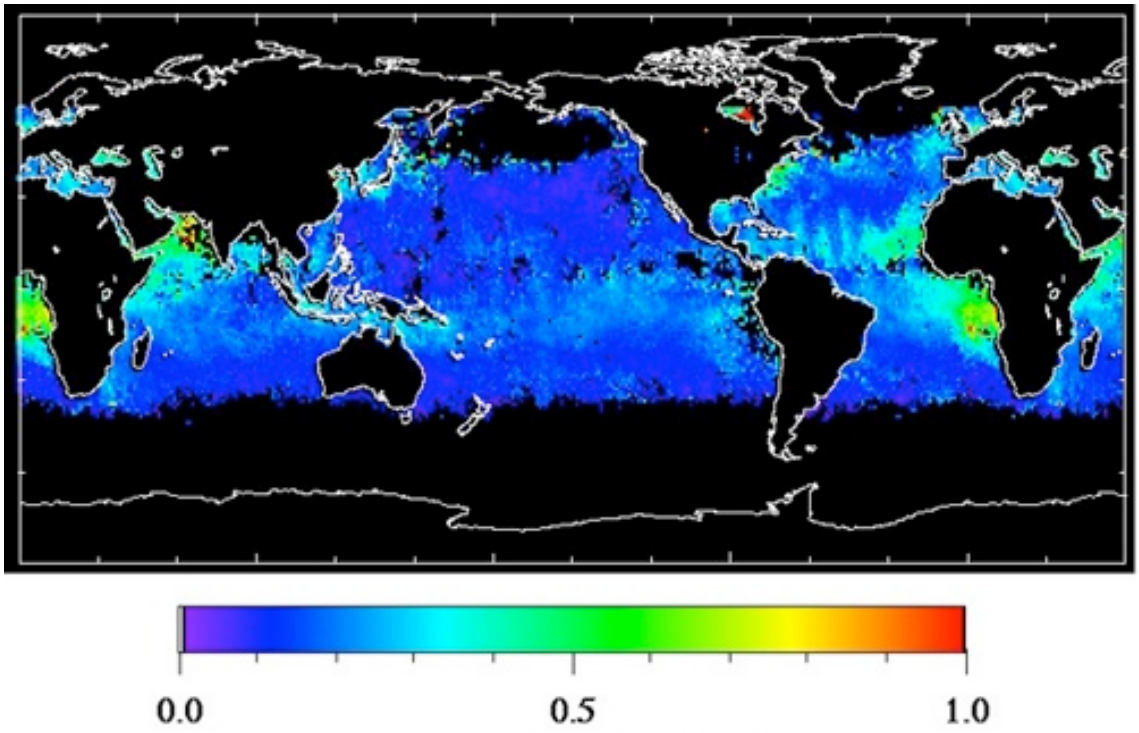

Figure 1.3.1a Distribution of Aerosol optical thickness (AOT) at wavelength 500nm. Monthly mean value of July, 1990. (Higurashi and Nakajima, 1999)

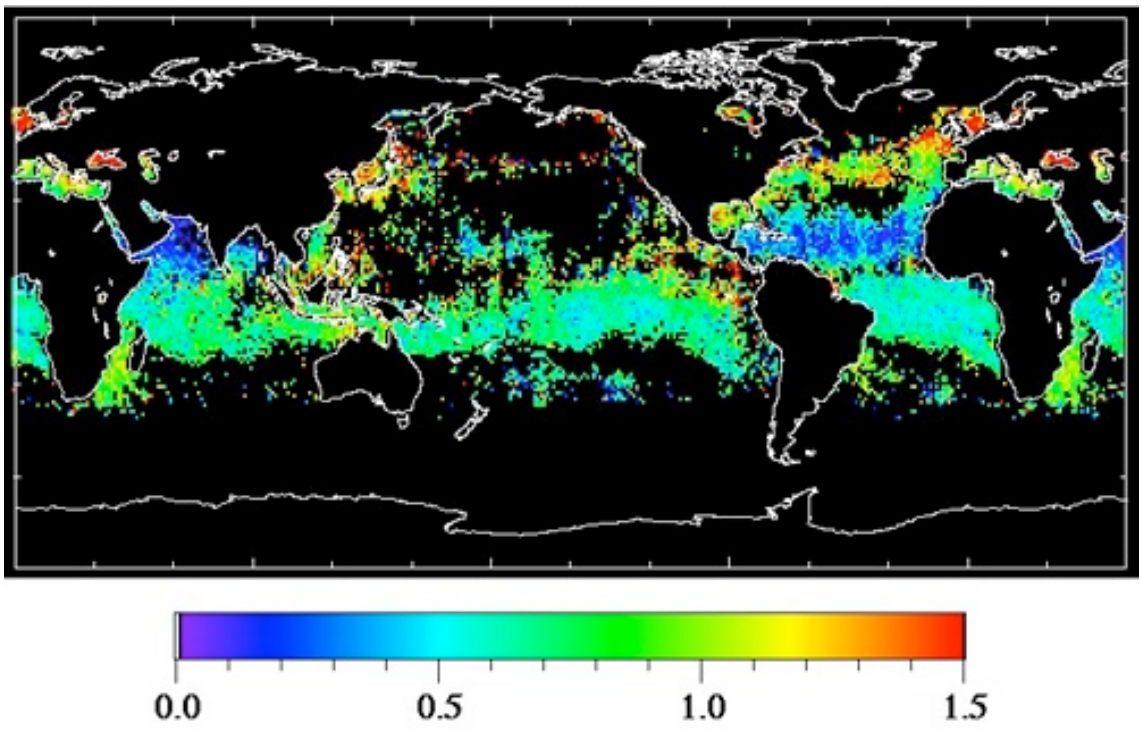

Figure 1.3.1b Same as Figure 1.3.1a but for distribution of Aerosol Ångström Exponent (AE).

Development of aerosol remote sensing over land needed more time as compared to the ocean algorithm development, because land surface reflectivity is larger and more variable temporally or spatially than that in the ocean surface case. Spectral and angular dependence of the surface reflectivity has to be understood and evaluated before aerosol remote sensing (e.g., Leroy et al., 1997; Wanner et al., 1997; Soufflet et al., 1997). Aerosol remote sensing over land was firstly developed over low surface albedo areas like a dense vegetation area using the correction method of surface reflectivity developed by Kaufman et al. (1997a). They estimated the surface albedo at a target wavelength (VIS: visible wavelength) using that at a wavelength in near infrared (NIR) spectral region, such as 1.6 or 2.13 μm, which are less susceptible to aerosol loading, as follows,

$$A_g(\mathrm{VIS}) = k \cdot A_g(\mathrm{NIR}), \tag{1.3.2}$$

where A_g(VIS) and A_g (NIR) are values of the surface albedo at VIS and NIR wavelengths, and k is a proportional constant to be determined empirically.

Using this correction method of surface albedo, Remer et al. (2005) retrieved AOT and fine mode fraction ($\eta=\tau^{\mathrm{fine}}/\tau^{\mathrm{total}}$) from the data of MODIS (the Moderate-resolution Imaging Spectro-radiometer) on board the NASA's Terra and Aqua satellites over dark land. This method is called the dark target method. In their algorithm, they first determine the mean surface reflectance in 10-km boxes corresponding to 20 by 20, or 400 pixels for each box. The mean surface reflectance at 0.47 and 0.66μm ($\overline{A}_g(0.47\mu\mathrm{m})$ and $\overline{A}_g(0.66\mu\mathrm{m})$) are derived by measured surface reflectance of MODIS channel at 2.13 μm, A_g(2.13μm) in the following conditions: the A_g(2.13μm) should be in the range of $0.01 \le A_g(2.13\mu\mathrm{m}) \le 0.25$; The darkest 20% and brightest 50% of A_g(0.66μm) are discarded; There should be at least 12 pixels that satisfied the conditions in the 20 by 20 box. Then arithmetic means are calculated as

$$\overline{A}_g(0.47\mu\mathrm{m}) = \left\langle 0.25 \cdot A_g(2.13\mu\mathrm{m}) \right\rangle_{\text{10-kmBOX}}, \tag{1.3.3}$$

$$\overline{A}_g(0.66\mu\mathrm{m}) = \left\langle 0.50 \cdot A_g(2.13\mu\mathrm{m}) \right\rangle_{\text{10-kmBOX}}. \tag{1.3.4}$$

Next they chose a aerosol model from library models (pure non-dust, pure dust and mixed) using the ratio between $\overline{R}(0.66\mu\mathrm{m})$ and $\overline{R}(0.47\mu\mathrm{m})$, where $\overline{R}$ is the measured mean top-of-atmosphere (TOA) reflectance, and following criteria:

$\overline{R}(0.66\mu\mathrm{m}) / \overline{R}(0.47\mu\mathrm{m}) < 0.72$ then pure non-dust, (1.3.5)

$\overline{R}(0.66\mu\mathrm{m}) / \overline{R}(0.47\mu\mathrm{m}) > 0.9 - 0.01(\Theta - 150°)$ then pure dust, (1.3.6)

$$0.72 \le \bar{R}(0.66\mu\text{m}) / \bar{R}(0.47\mu\text{m}) \le 0.9 - 0.01(\Theta - 150°) \quad \text{then mixed,} \tag{1.3.7}$$

for data of scattering angles in a rage of Θ = 150° to 168°. When a selected aerosol model is mixed, $\eta = \tau^{\text{fine}} / \tau^{total}$. In this procedure, model values of the apparent reflectance and AOTs at wavelengths of 0.47 and 0.66μm are approximately inferred by the following single scattering approximation formula and LUT prepared for the single scattering approximation (Kaufman et al., 1997a) as,

$$\bar{R}_\lambda = \omega_\lambda \cdot \tau_\lambda \cdot P_\lambda, \tag{1.3.8}$$

where λ denotes wavelength (here 0.47 and 0.66μm); ω_λ and P_λ are single scattering albedo and aerosol phase function assuming the selected aerosol model. Then, they retrieve values of AOT and fine mode fraction using a full LUT, which includes the full multiple scattering effects different from the one used in the model selection procedure by single scattering approximation, for the chosen model. Finally, they interpolate the values at 0.47 and 0.66μm to AOT at a standard wavelength of 0.55μm, which is often used in global climate modeling and analysis. For retrieval over the ocean, they apply Tanré et al. (1997) and Levy et al. (2003) based on a LUT constructed using the algorithm of Ahman and Frasers (1982). It is pointed out that the estimated errors of retrieved AOT are ±0.05±0.20AOT over the land and ±0.03±0.05AOT over the ocean. Figure 1.3.2 shows AOT values retrieved from MODIS dark target method, and we can see the global AOT values over both ocean and land are retrieved in most regions of the globe. However, it is found that there are no retrievals in a high surface reflectance region such as polar and arid or desert regions.

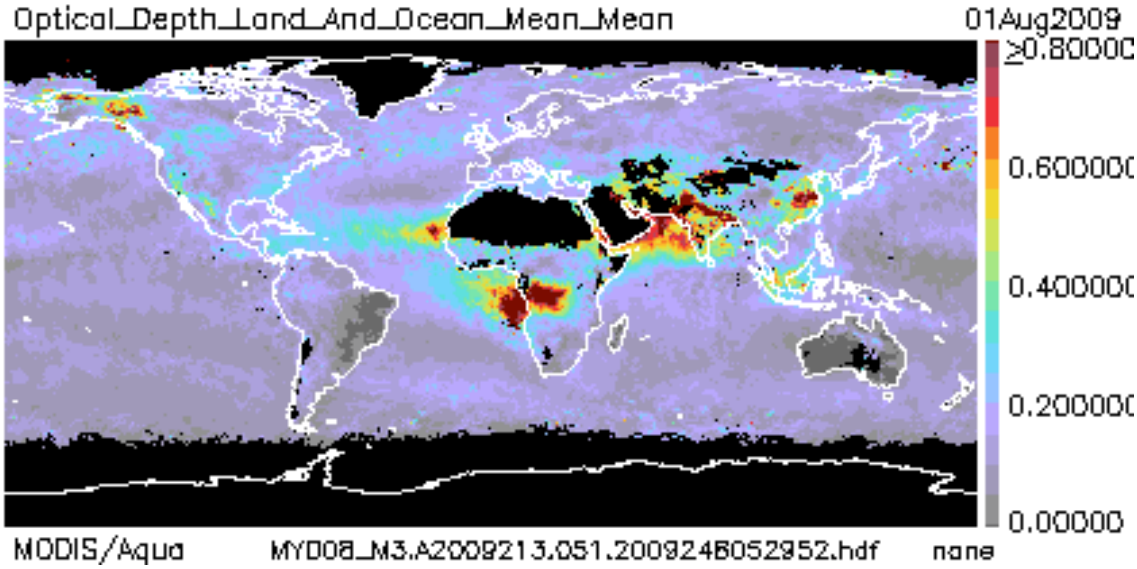

Figure 1.3.2 AOT distribution as derived from MODIS data by the dark target method. (http://modis-atmos.gsfc.nasa.gov/IMAGES/)

For the desert region, the aerosol retrieval from satellite needed to wait until 2000s when algorithms were developed utilizing near ultraviolet (NUV) to blue (< 0.5μm) wavelengths, where the surface reflectance is comparably low. Hsu et al. (2004, 2006) retrieved aerosol optical properties (AOT and aerosol type) over arid or desert region, such as the Sahara Desert and Arabian Peninsula, using two blue wavelengths, 0.412 and 0.470μm (or 490μm), as shown in Fig. 1.3.3. Their algorithm is known as the Deep Blue method, and is applied to MODIS and SeaWiFS sensor data. The agreement between AERONET (Aerosol Robotic Network), which is ground-based observation network, is not small as compared to the case of the dark target method, but is within 30%. Fukuda et al. (2013) also retrieve AOT using data at 0.38μm, a NUV wavelength implemented in the TANSO-CAI imager sensor on board the GOSAT satellite. They developed a correction method of the surface reflectance at 0.38μm by a similar relation to Eq. (1.3.2) but with 0.38μm and 0.67μm (Band 1 and 2 of the CAI sensor). They found that the NUV (0.38μm) reflectance does not have a good statistical correlation with that of NIR (2.1μm). They name the algorithm a modified-Kaufman method.

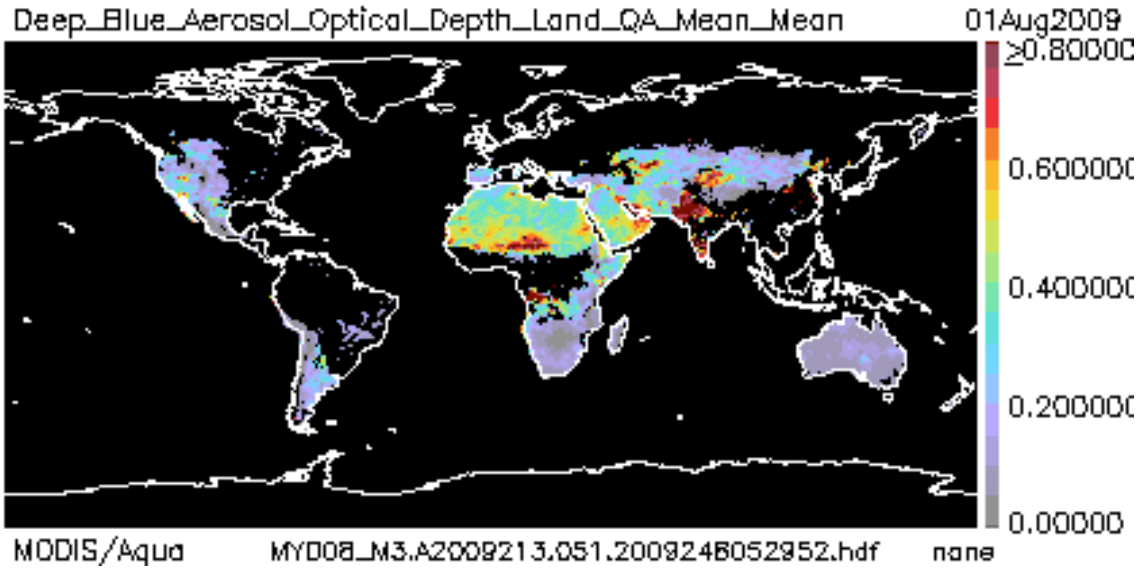

Figure 1.3.3 AOT distribution as derived from MODIS data by Deep Blue method. (http://modis-atmos.gsfc.nasa.gov/IMAGES/)

1.4 Aerosol remote sensing over inhomogeneously-distributed surface and its problem

There remains a challenging problem for the case of inhomogeneous surface. Common

recognition of researchers is that aerosol remote sensing is difficult over the region where various types of ground surface are mixed like urban area (Fig. 1.4.1). In the past studies, therefore, they tried to select homogeneous land surface by a spatial inhomogeneity test before applying an aerosol retrieval algorithm. Over the land, however, the surface reflection is never constant and undergoes spatial and temporal variation. Especially, the urban surface is complex with high and low reflectances, so that the urban aerosol properties have not been yet accurately retrieved from satellites (Chu et al., 2002; Hernandez et al., 2007). Chu et al. (2002) pointed out that MODIS AOT is overestimated as compared with AETONET-measured AOT in urban area. Hernandez et al. (2007) also reported that the current MODIS AOT retrieval system is accurate over dark and fairly uniform land cover types, but there are inherent weaknesses which make the system less useful for aerosol monitoring over urban area. They also showed that MODIS AOT is remarkably overestimated in the northeast coast of the United States, that is an urban area, compared with AETONET AOT. Figure 1.4.2 shows a comparison between MODIS AOT and AERONET AOT over a AERONET New York site where is the northeast coast of the United States (Hernandez et al., 2007). The red points are matchups between values from AERONET and from the closest MODIS pixel to the site, and it is found that MODIS AOTs are overestimated. On the other hand, the blue points are results of matchups between AERONET AOT and the minimum AOT within a 40km box. They claimed that this matchup method is rationalized by a reasonable assumption that the minimum AOT will occur for pixels over dark surfaces such as dense vegetation area (Hernandez et al., 2007). However, this result clearly indicates that the past algorithms do not retrieve the aerosol properties over inhomogeneous urban areas.

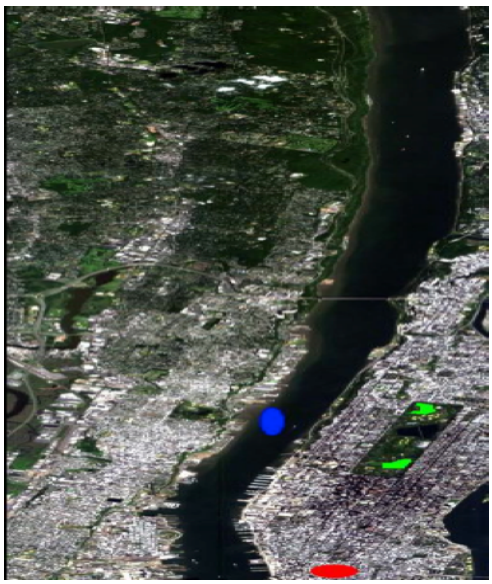

Figure 1.4.1 Surface image of urban area in Northeast of United States. (Hernandez et al., 2007)

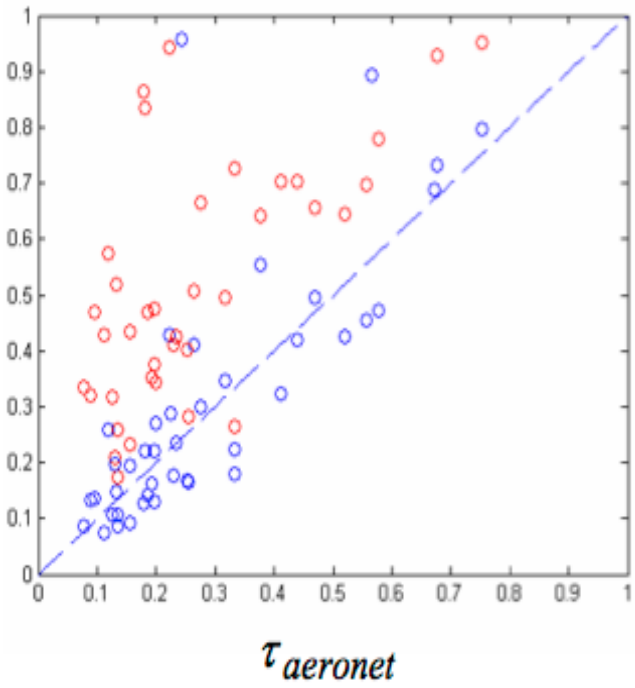

Figure 1.4.2 Intercomparison between AERONET and MODIS AOT (Hernandez et al., 2007)

There are new challenges of land aerosol remote sensing by modern satellite sensors, such as ADEOS-II/POLDER (Polarization and Directionality of the Earth's Reflectance), Terra/MISR (Multi-angle Imaging Spectroradiometer), CALIPSO/CARIOP (Cloud-Aerosol Lidar with Orthogonal Polarization), etc, with their new functions of multi-angle, polarization measurement, and active lidar sensing. POLDER uses a combination of spectral channels (0.44-0.91μm) with several viewing angles, and can measure the polarized radiance. The polarized radiance does not depend too much on the land surface reflection, so that it is possible to retrieve aerosol properties under various land conditions. The resolution of POLDER is, however, coarse as about 6×7km, so that aerosol remote sensing over heterogeneous land surface is questionable. MISR obtains images at four bands (443, 558, 672, and 866 nm) with resolution 275m at nadir and off-nadir with 5 along-track viewing angles. AOT over heterogeneous land is retrieved from MISR data using empirical orthogonal functions derived from the spectral contrast by multi-angle observations. However, they reported that the accuracy is 10~20% (Kahn et al., 2005), and that the range of and a number of measured wavelengths is not enough to retrieve accurate AOT over bright area. On the other hand, CALIOP is an active sensor with a lidar, so that it is able to retrieve the vertical aerosol

profiles without effect of land surface reflection. However, their aerosol sensing is limited only to nadir direction, so that spatially dense and temporally frequent aerosol measurement is not possible by CALIOP.

In the above situation, in late years, the local area comparison of aerosol products between AERONET and satellite has been conducted from 2011 to understand the problems and accuracy of satellite-retrieved aerosol properties by making observations at multiple locations in urban area (NASA DRAGON project; http://aeronet.gsfc.nasa.gov/new_web/dragon.html), as shown in Fig. 1.4.3. They established a mesoscale gridded network of sun photometers that encompasses urban, agricultural and mountain landscapes over the Washington DC metropolitan area (Fig. 1.4.4). They optimized the grid spacing in the gridded network in order to validate or collaborate inversion products in conjunction with aircraft in situ measurements, and validate satellite retrievals for 50m to 10km pixel resolution.

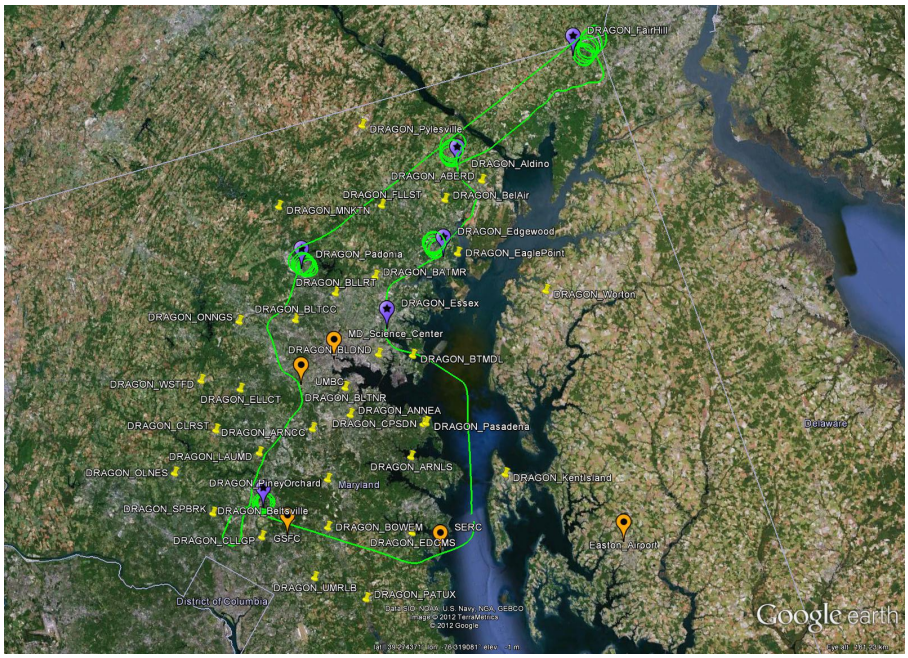

Fig 1.4.3 A map of AEROENT sites (yellow, purple and orange). The network was established for six weeks operation over the Washington DC-Baltimore metropolitan area from July 1 to August 15, 2011. The network was strategically located to take advantage of DISCOVER-AQ in situ and airborne resources (green).

(http://aeronet.gsfc.nasa.gov/new_web/DRAGON-USA_2011_DC_Maryland.html)

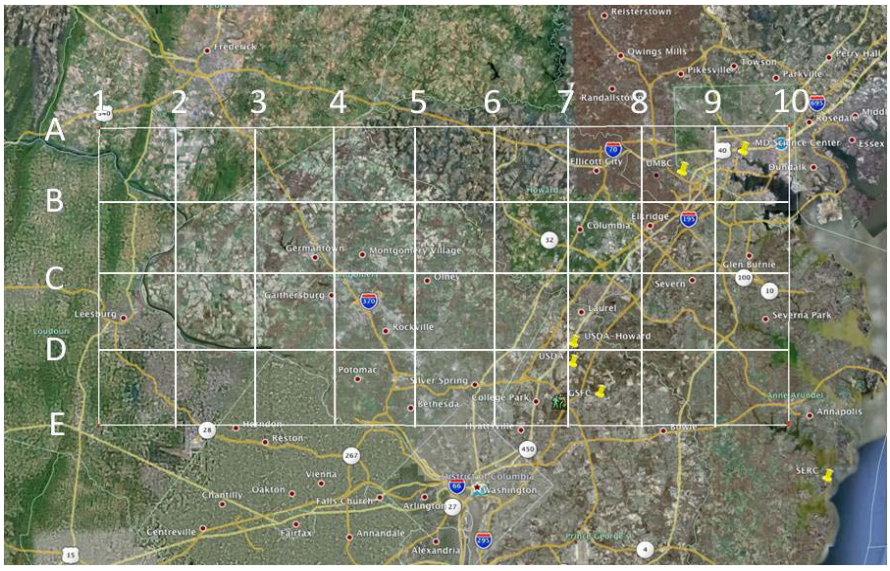

Figure 1.4.4 Proposed grid box over the Washington DC-Baltimore of NASA DRAGON project. (Holben et al., DRAGON white Paper)

The results from field experiments with such dense surface networks in urban regions are currently being analyzed and will depict in near future the accuracy of satellite remote sensing over urban areas. It should be pointed out, however, a challenge must be made to develop a new algorithm that can work over heterogeneous surface to fully utilize the data from such spatially dense surface networks.

As mentioned above, it is the state that retrieval of accurate aerosol properties and its distribution in the urban area from satellite remote sensing are difficult problem. However, the urban area is a source region of atmospheric pollution aerosols and most of anthropogenic aerosols are emitted from urban area. Anthropogenic aerosols include both scattering and absorbing aerosol, such as sulfate, nitrate, black carbon and organic carbon (soot) released by burning of fossil fuels and biomass by traffic and industrial activities etc. These aerosols scatter and absorb the short wave and long wave radiation (direct effect), or interact with cloud as cloud condensation nucleus and change the cloud size and its lifetime (indirect effect), and then affect the earth's climate.

Total urban area account for about 0.2% of the land on the globe (Demographia World Urban Areas & Population Projections, 2014: http://www.demographia.com/) and the weight of anthropogenic aerosols (about 10%) is fewer than natural aerosols (about 90%), while it is pointed

out that the radiation effect of anthropogenic aerosol is large and a half of aerosol optical thickness is due to anthropogenic aerosols (Asano, 2005). IPCC AR5 (2013) reports that the maximum likelihood values of anthropogenic aerosol direct and indirect effect of radiative forcing are -0.27 [-0.77 to 0.23] W/m^2 and -0.55 [-1.33 to -0.06] W/m^2, respectively, but the uncertainties are still large (See Fig. 1.1.2).

Furthermore, several researches show the impact for earth's climate of anthropogenic aerosol; for example, Chen et al. (2010) estimates annual mean total column burdens of anthropogenic aerosols (sulfate, nitrate, ammonium, primary organic aerosol, secondary organic aerosol, and black carbon) for preindustrial, 20th century, and 21st century (until 2100). They point out that increases in peak concentrations are predicted over heavily industrialized and population areas such as South and East Asia, Europe, and the eastern United States, and predict the amount become over twice at the areas in 21st century compared with 20th century; and Wilcox et al. (2013) assesses anthropogenic effect (i.e. its single forcing) for temperature and precipitation until 2010 compared with 1900 by CMIP5, and the forcing in 2010 is about -0.45 [-0.6 to -0.4] K and -0.05 [-0.07 to -0.02] mm/day, respectively. Anthropogenic aerosol forcing account for over 30% of modeled variation in global and annual-mean near-surface temperature in the mid-twentieth century. Moreover, space and time variation of aerosol is very large, because the lifetime is short (~10days) and locality is large by the land use (e.g. urban, desert, vegetation or ocean).

Therefore, understanding of aerosol properties over urban area where is a source region of anthropogenic aerosols including absorbing aerosol such as BC, EC or soot is one of important task for aerosol and climate studies, and expected resolution for aerosol retrieval is as high as few kilometer to be used for assessment of the aerosols radiative forcing and their effect to the earth's climate (IPCC AR5).

1.5 Objective of this study

As reviewed by preceding sections, the aerosol properties have been retrieved over several surface types, such as sea, vegetation and desert region, using satellite observation. But, at present, the aerosol optical properties in urban areas have not been obtained by satellite remote sensing with a single pixel analysis, because the surface reflectance in the urban region is spatially heterogeneous including dark and bright surfaces. The retrieved value of AOT is not in good agreement with AOT obtained by ground-based observation, and is highly overestimated (Chu et al., 2002; Hernandez at al., 2007). Furthermore, an aerosol absorption parameter, such as SSA or volume soot fraction in aerosols (SF) has not been retrieved in urban area.

On the other hand, high spatial resolution, multi-wavelength and multi-angle observation data

have been obtained by recent imaging sensors. With this development, a comprehensive remote sensing method using multi-information, such as multi-wavelength and multi-angle, has become popularly used (Dubovik et al., 2011; Lyapustin et al., 2011), which retrieve aerosol properties combining the multiple information. Dubovik et al. (2011) have developed a method to retrieve AOT, SSA and aerosol size distribution at one pixel from POLDER multi-angle and multi-wavelength data using a maximum likelihood method (ML). Lyapustin et al. (2011) retrieved AOT and aerosol type using multi-angle or surface bidirectional reflectance factor (BRF) using an optimal method with LUT method.

Another important progress in the recent remote sensing algorithm studies is the direct use of radiation transfer calculation in the inversion problem of aerosol remote sensing taking place of LUT by the progress of computer performance (Dubovik et al., 2011). Although direct use of radiation transfer model takes a large computing time, it has the following merits for developing a flexible inversion algorithm: It is easy to change observation conditions by changing aerosol and atmospheric models, sensor viewing geometries and wavelengths; I can set a state vector with any combination of geophysical parameters and machine constants that should be retrieved from inverse problem; accurate radiation radiances are computed without interpolation error as in the LUT method to include the effects of various experimental conditions such as the realistic atmospheric conditions, multiple scattering process, polarization effects and others.

As a conclusion, I set the purpose of the present study as to derive aerosol optical properties such as AOT and absorption parameter (SF), in a region where the surface types are complicatedly mixed, such as urban area. For this purpose I develop a comprehensive remote sensing algorithm for retrieval of aerosol properties by multi-wavelength and multi-pixel method that can handle the land surface heterogeneity. At the same time I incorporate a radiative transfer model directly into the algorithm to make the algorithm flexible to handle various atmospheric and sensor conditions.

Chapter 2 Algorithm description

2.1 Introduction

A direct use of radiation transfer calculation has been employed after around 1980s for non-linear remote sensing problems supported by the progress of computing technology and development of rapid radiative transfer solvers (e.g., Nakajima et al., 1996; Dubovik and King., 2000; Dubovik et al., 2011). A rapid radiative transfer code, RSTAR, has been used in the AERONET and SKYNET operational processing system (Nakajima et al., 1996; Dubovik and King, 2000). I have adopted the similar strategy to build a new satellite remote sensing algorithm to retrieve the aerosol optical characteristics using multi-pixel and multi-wavelength information of satellite imagers. In this algorithm, the inversion method is formulated by a combination of the MAP method (Maximum a posteriori method, Rodgers, 2000) and the Phillips-Twomey method (Phillips, 1962; Twomey, 1963) to pose a smoothing constraint to the state vector. I directly incorporated a radiation transfer code, RSTAR (Nakajima and Tanaka, 1986, 1988), for numerical computation of satellite-received radiances that are needed to calculate the Jacobian matrix at each iteration step of searching the optimal solution of the state vector for the non-linear inverse problem. Retrieval parameters in the algorithm are AOTs of fine mode and coarse mode (sea salt or dust) particles, a volume soot fraction (SF) in fine mode particles, and ground surface albedo of each observed wavelength. I simultaneously retrieve all the parameters by solving the inverse problem utilizing a set of radiance data at all the pixels in a target domain by the method explained in the following sections.

2.2 Theory and definition

2.2.1 Geometry

The satellite-received solar radiation contains contributions from scattering by atmospheric molecules, particulates, and earth's surface. As shown in Fig. 2.2.1, I define the satellite observation geometry by the solar zenith angle, θ_0, and the satellite nadir angle, θ (the satellite zenith angle is given as $\theta_{sat,z} = 180-\theta$), and the relative azimuth angle between the sun and the satellite, ϕ. The scattering angle, Θ, is given by these angular variables as follows,

$$\cos\Theta = \mu\mu_0 + \sqrt{1-\mu^2}\sqrt{1-\mu_0^2}\cos\phi \quad , \tag{2.2.1}$$

where $\mu=\cos\theta$ and $\mu_0=\cos\theta_0$.

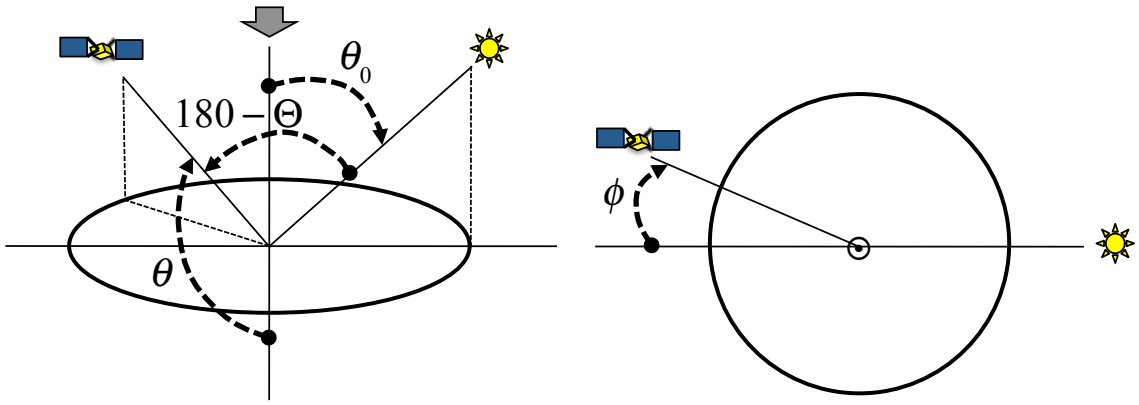

Figure 2.2.1 Definition of satellite observation geometry by solar zenith angle θ_0, satellite nadir angle θ, and the relative azimuth angle, ϕ, between the sun and the satellite. Θ is the scattering angle.

2.2.2 Relation between measured and retrieval parameters

In this section I formulate the satellite received radiance by a two stream approximation in order to understand the relation between measured and retrieval parameters. A satellite measures solar radiance backscattered to space by the earth-atmosphere system. The observed satellite signal is composed of atmospheric path radiance (1), which is an upward component of scattered solar radiance in the atmosphere, and radiance reflected by the earth's surface (2) and scattered by the atmosphere after reflected by the surface (3) as illustrated in Fig. 2.2.2.

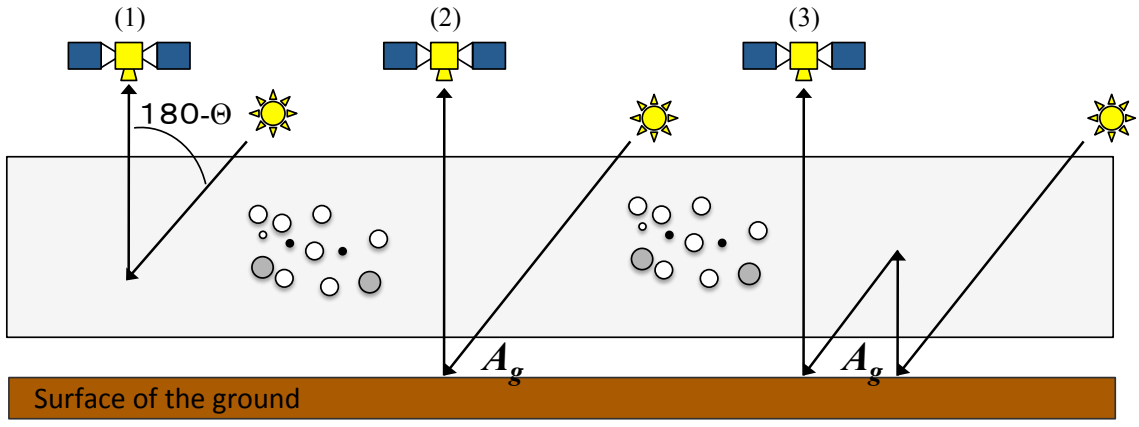

Figure 2.2.2 Illustration of the aerosol remote sensing by a satellite sensor. (1) atmospheric path radiance, (2) radiance reflected by the earth's surface, and (3) radiance scattered by the atmosphere after reflected by the surface.

These components can be expressed in simple formulae of the single scattering approximation as follows,

$$L = L_a + \frac{1}{\pi} t(\mu)(A_g + A_g \bar{r} A_g) t(\mu_0) \mu_0 F_0 + O(\tau^2), \tag{2.2.2}$$

$$L_a \approx m\omega\tau P(\Theta) F_0 + O(\tau^2), \tag{2.2.3}$$

where ω is the single scattering albedo, τ the optical thickness, $P(\Theta)$ the phase function as a function of the scattering angle Θ, A_g the ground albedo, and F_0 the extraterrestrial solar irradiance. L_a is the atmospheric path radiance (component (1) in Fig. 2.2.2) and the second term of Eq. (2.2.2) corresponds to the sum of components (2) and (3) in Fig. 2.2.2. Flux unidirectional transmissivity and reflectivity $t(\mu_0)$ and $r(\mu_0)$ and spherical (or global) albedo $\bar{r}$ are given as

$$t(\mu_0) = e^{-m_0\tau} + t_a(\mu_0) \approx 1 - m_0\tau + m_0\omega\tau\gamma^+(\mu_0) = 1 - [1 - \omega\gamma^+(\mu_0)] m_0\tau, \tag{2.2.4}$$

$$t_a(\mu_0) \equiv \frac{F^+_{\mathrm{dif}}(\mu_0)}{\mu_0 F_0} = m_0\omega\tau\gamma^+(\mu_0), \tag{2.2.5}$$

$$r(\mu_0) \equiv \frac{F^-_{\mathrm{dif}}(\mu_0)}{\mu_0 F_0} = \omega\tau m_0 \gamma^-(\mu_0), \tag{2.2.6}$$

$$\bar{r} = r(\bar{\mu}) = 2\int_0^1 r(\mu_0)\mu_0 \, d\mu_0, \tag{2.2.7}$$

where downward and upward diffuse radiative fluxes, $F^+_{\mathrm{dif}}(\mu_0)$ and $F^-_{\mathrm{dif}}(\mu_0)$, are written as

$$F^+_{\mathrm{dif}}(\mu_0) = \int_0^{2\pi} d\phi \int_0^{+1} \mu \, d\mu \, m\omega\tau P(\Theta) F_0 = \omega\tau F_0 \int_0^{+1} \mu \, d\mu \int_0^{2\pi} d\phi P(\Theta) = \omega\tau\gamma^+(\mu_0) F_0, \tag{2.2.8a}$$

$$F^-_{\mathrm{dif}}(\mu_0) = \int_0^{2\pi} d\phi \int_{-1}^{0} \mu \, d\mu \, m\omega\tau P(\Theta) F_0 = \omega\tau\gamma^-(\mu_0) F_0. \tag{2.2.8b}$$

γ^+ and γ^- are the downward and upward fractions of light scattering as give as

$$\gamma^{\pm} = \int_{M_{\pm}} \mu \, d\mu \int_0^{2\pi} d\phi P(\Theta). \tag{2.2.9}$$

In the Gaussian two stream approximation, I have

$$\gamma^{\pm}(\mu_0) = \frac{1}{2}(1 \pm \sqrt{3} g \mu_0) \quad \text{and} \quad \mu = \mu_0 = \bar{\mu} = \frac{1}{\sqrt{3}}.$$

If I define the apparent reflectance R_{sat} corresponding to the observed reflectance by a satellite,

$$R_{sat} \equiv \frac{\pi L}{\mu_0 F_0}, \tag{2.2.10}$$

then it can be related with τ, ω, P, and A_g as follows:

$$
\begin{aligned}
R_{sat} &\approx \pi m m_0 \omega \tau P(\Theta) + t(\mu)(A_g + A_g \bar{r} A_g) t(\mu_0) \\
&= A_g + \{\pi m m_0 \omega P(\Theta) - A_g \{m + m_0 - \omega[\gamma^+(\mu) m + \gamma^+(\mu_0) m_0] - A_g \omega \sqrt{3} \bar{\gamma}^-\}\}\tau . \qquad (2.2.11) \\
&= A_g + [\pi m \omega P(\Theta) - 2A_g(1 - \omega\gamma^+) + A_g^2 \omega \gamma^-] m\tau
\end{aligned}
$$

2.3 Multi-wavelength and multi-pixel method

2.3.1 Concept of Multi-wavelength and multi-pixel method

Kaufman et al. (1987) introduced a remote sensing method of aerosol absorption (or SSA) from satellite observation. The method is based on the measurement of the change in the upward radiance between clear and hazy days over a varying surface reflectance (i.e. multi-pixel information) in an assumption that aerosol optical thickness (AOT) over analysis region is homogeneous. For dark and bright surfaces, aerosols in the atmosphere respectively increase and decrease the apparent reflectance as compared with that without atmosphere. As shown in Fig. 2.3.1, there are cases where the surface albedo and reflectance of the surface-atmosphere system are equal to each other. This reflectance is called the neutral surface reflectance, R_c ($=A_{g,c}$), for which the upward reflectance is independent of AOT. This situation corresponds to the case that the second term of Eq. (2.2.11) becomes zero, i.e.,

$$
\pi m \omega P(\Theta) - 2A_{g,c}(1 - \omega\gamma^+) + A_{g,c}^2 \omega \gamma^- = 0 , \qquad (2.3.1)
$$

when the atmospheric path radiance (first term of the left hand side) becomes equal to the reduction in the attenuated surface reflection that depends on values of A_g and SSA.

Once $A_{g,c}$ is determined, the aerosol single-scattering albedo (SSA) can be evaluated by using a theoretical relation between R_c ($A_{g,c}$) and SSA as Eq. (2.3.1) in the two stream approximation. This method is called Kaufman's neutral method, and applied to data of low and high AOT days under the condition that the surface reflectance does not vary temporally and that AOT is spatially homogeneous. It should be noted, however, this method also can be applied to a satellite imager at a specific time to derive AOT and SSA if a horizontally homogeneous aerosol layer covers a heterogeneous surface of various reflectivities as illustrated by Fig. 2.3.1.

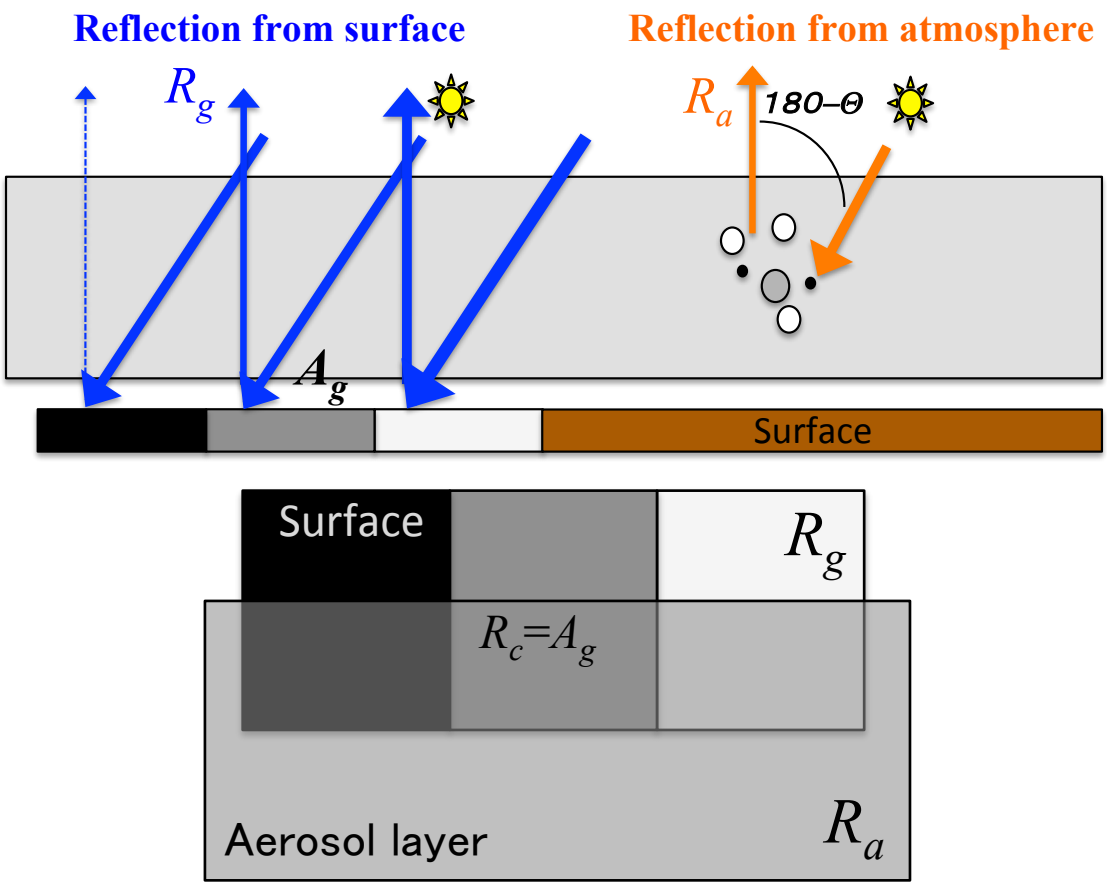

Figure 2.3.1 Illustration of a multi-pixel retrieval method for case of a homogeneous aerosol layer over a heterogeneous surface with various surface albedo A_g to derive the neutral reflectance R_c.

Also we can use different wavelengths to find a set of various surface reflectances as shown in Figs. 2.3.2 and 2.3.3; the surface reflectance has a characteristic spectrum depending on surface types and wavelengths. Therefore, we are able to derive AOT and SSA from analysis of a set of radiances at difference wavelengths. In this multi-wavelength method, we should recognize that AOT and SSA are also a function of wavelength and difficult to be estimated as compared in the multi-pixel method. However, the wavelength dependence of the AOT and SSA are largely different from those of the surface reflectance, so that the separation of the aerosol and surface information is not so difficult. It is known, for example, that AOT (τ) spectrum well follows Ångström's law as expressed by a formula of $\tau = \beta\lambda^{-\alpha}$, where β is turbidity coefficient and α is a parameter called Ångström exponent (AE).

I thus expanded the *Kaufman neutral method* applying to multi-wavelength and multi-pixel data over a heterogeneous surface. The formulation of simultaneous inversion of aerosol parameters from the multi-information data will be given in the following section.

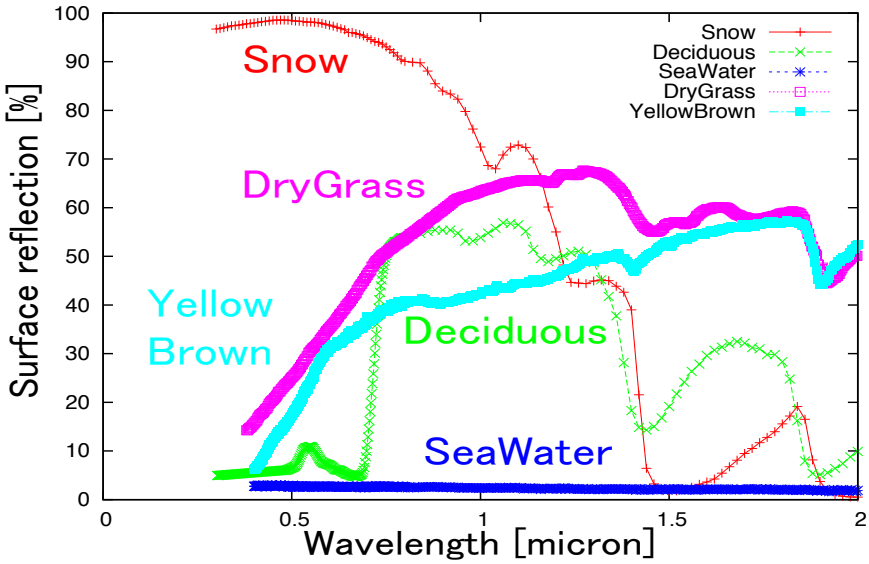

Figure 2.3.2 Spectral albedo dependence of different surfaces. (Aster spectral library: http://speclib.jpl.nasa.gov/yori)

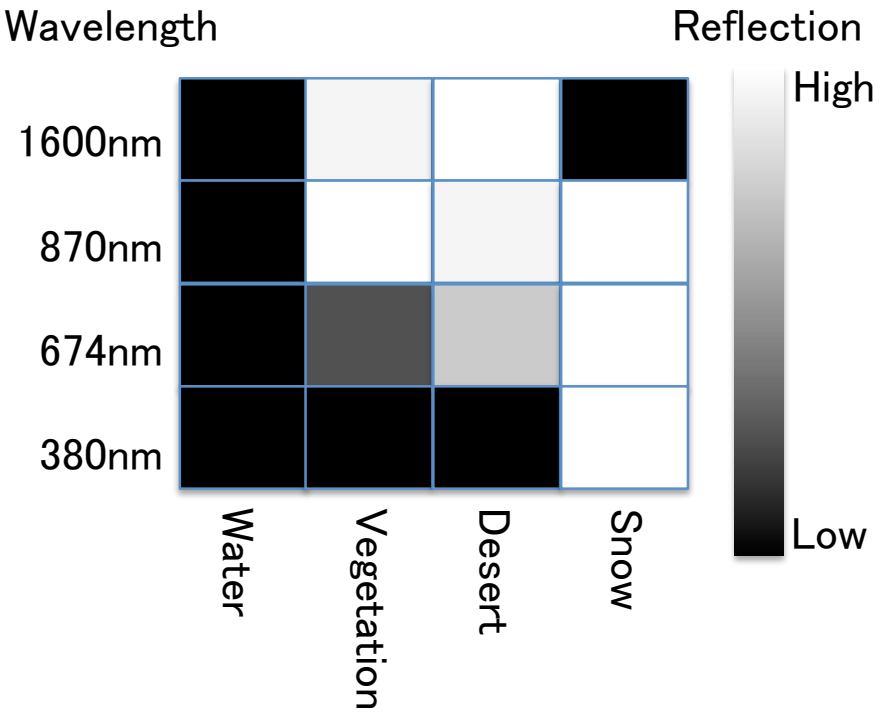

Figure 2.3.3 Image of spectral albedo of different surfaces and wavelengths

2.3.2 Assumption of aerosol optical model

To retrieve aerosol properties in stable manner by the present method, I first reduced the freedom of the information contents by prescribing the functional form of the aerosol size distribution, i.e., a bimodal log-normal volume size spectrum as follows (Fig. 2.3.4):

$$\frac{dV}{d\ln r} = \sum_{n=1}^{2} c_n \exp\left\{-\frac{1}{2}\left[\frac{\ln r - \ln r_{m,n}}{\ln S_n}\right]^2\right\}, \tag{2.3.2}$$

where V is the aerosol volume density, r and r_m is aerosol particle radius and mode radius in μm, and S_n is the standard deviation of r.

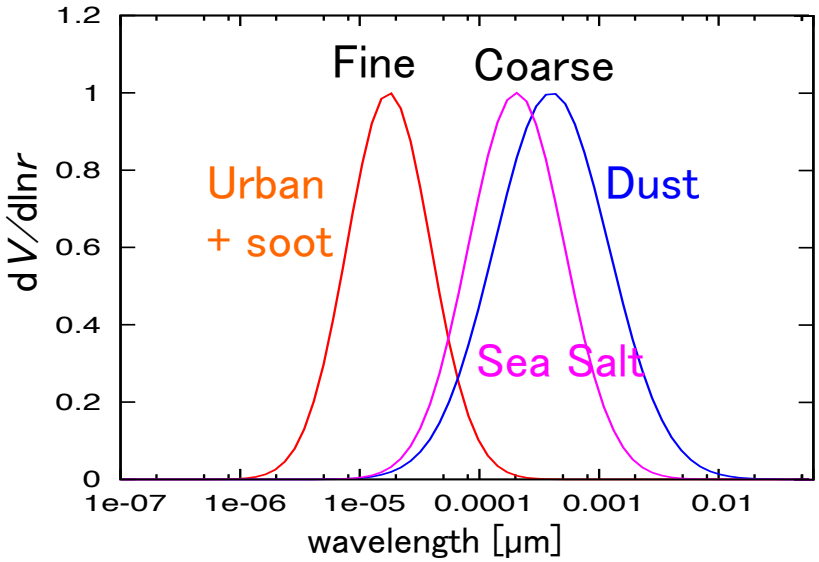

Figure 2.3.4 Normalized aerosol volume size distributions used in this study. A bimodal log-normal function with fine and coarse modes are used to approximate the size distribution. I assume dust or sea-salt aerosols is assumed for the the coarse mode.

For absorption, I define the volume Soot Fraction (SF), which is a volume ratio of soot particle to the volume of fine mode particles,

$$f_{\text{soot}} = \frac{V_{\text{soot}}}{V_{\text{fine mode}}}, \tag{2.3.3}$$

where V_{soot} and $V_{\text{fine mode}}$ are the volume densities, per atmospheric volume, of soot particles in fine mode and of fine particles. In order to roughly understand the relation between SF (f_{soot}) and SSA (ω), I note the following equations in simplified linear volume approximation of the absorption and scattering cross sections:

$$a = NQ_{abs}\pi r^2 = NQ_{abs}\frac{3}{4r}\frac{4}{3}\pi r^3 = Q_{abs}\frac{3}{4r}V\,, \tag{2.3.4a}$$

$$s = NQ_{sca}\pi r^2 = Q_{sca}\frac{3}{4r}V\,, \tag{2.3.4b}$$

$$V = V_0 + V_{\text{soot}},\ f = \frac{V_{\text{soot}}}{V},\ 1 - f = \frac{V_0}{V}, \tag{2.3.4c}$$

$$\omega = \frac{s}{s+a} = \frac{Q_{sca,0}\dfrac{(1-f)}{r_0}}{Q_{sca,0}\dfrac{(1-f)}{r_0} + Q_{abs}\dfrac{f}{r_{\text{soot}}}}, \tag{2.3.4d}$$

where a and b are an absorption cross-section and scattering cross-section, N and V are the total particle number density and volume density of aerosols here, and Q_{abs} and Q_{sca} are the absorption and scattering efficiency factor, respectively. The subscript 0 means quantities of no-absorption.

I also assume aerosols in the atmosphere are smoothly distributed without varying largely in the horizontal direction as shown in Fig. 2.3.5. In this assumption, I use the Phillips-Twomey method (Phillips, 1962; Twomey, 1963) to pose a smoothing constraint to the inverse problem so as to minimize the squares of second differential of aerosol parameters is the horizontal direction. In detail, I will describe the method in the next section (section 2.3.3).

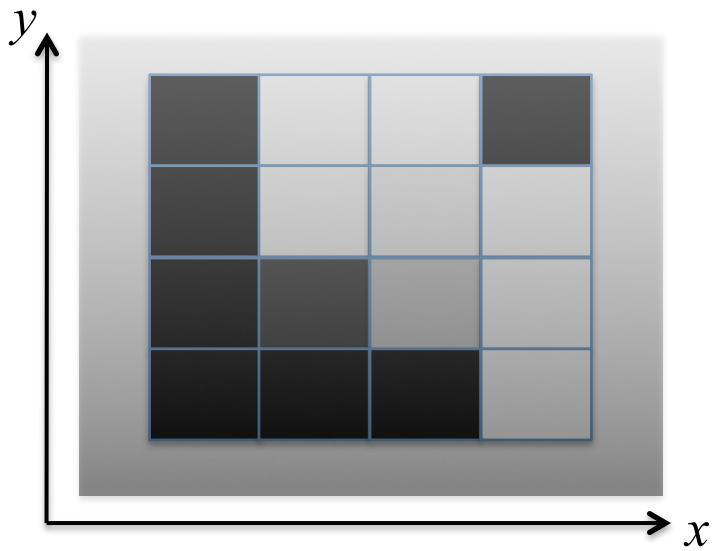

Figure 2.3.5 Heterogeneous surface and smoothly distributed aerosol layer. x and y denote horizontal coordinates.

2.3.3 Retrieval algorithm

In this section I formulate the inverse problem to retrieve the aerosol optical characteristics using multi-wavelength and multi-pixel information of satellite imagers. Pixels of satellite imagery are almost regularly arrayed as shown in Fig. 2.3.6. Let us define the observation vector by a set of measured apparent reflectances $\boldsymbol{R} = \{\{R\}_\lambda\}_x$ and the state vector by a set of geophysical parameters $\boldsymbol{u} = \{\tau_{\text{fine}}, \tau_{\text{coarse}}, f_{\text{soot}}, \{A_g\}_\lambda\}_x$, which are defined on a set of wavalengths $\boldsymbol{\lambda} = \{\lambda_i, i = 1, N_{Band}\}$ and horizontal coordinates $\boldsymbol{x} = \{x_i, y_j, i = 1, N_{domain}; j = 1, N_{domain}\}$. Then the satellite observation can be expressed by a basic formula to relate the observation vector with the state vector as,

$$\boldsymbol{R} = \boldsymbol{f}(\boldsymbol{u}) + \boldsymbol{e}, \tag{2.3.5}$$

where $\boldsymbol{f}(\boldsymbol{u})$ denotes a radiative transfer model (forward model), $\boldsymbol{e}$ is the error vector caused by several error sources (measurement error, modeling error in radiance etc. In detail, $\boldsymbol{u}$ is the vector of retrieved parameters in this algorithm, for example,

$u_{p=1}$: aerosol optical thickness (AOT) of fine mode (AOT fine, τ_{fine}),
$u_{p=2}$: AOT of coarse mode (sea salt) particles (AOT seasalt, τ_{seasalt}),
$u_{p=3}$: AOT of coarse mode (dust) particles (AOT coarse, τ_{coarse}),
$u_{p=4}$: a volume soot fraction in fine mode particles (f_{soot}),
$u_{p=5}$ - $u_{p=\text{N}p}$: ground surface albedo of each observed wavelength ($A_{g,\lambda}$, λ=1,N$_w$).

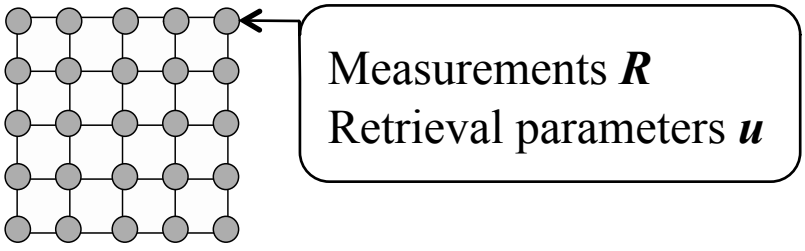

Figure 2.3.6 Array of satellite observation pixels. Each pixel has aerosol information, $\boldsymbol{u}$, and measured reflection information, $\boldsymbol{R}$, are defined on a set of wavelengths.

In this satellite algorithm, the inversion method is an optimal method of a combination of the MAP method (Maximum a posteriori method, Rodgers, 2000) and the Phillips-Twomey method

(Phillips, 1962; Twomey, 1963). I simultaneously retrieve all the elements of the state vector that are defined on the array of pixels and the set of wavelengths by seeking the inverse function of $\boldsymbol{f}$ in Eq. (2.3.5). First, I base this approach on the MAP method as defined by Rodgers (2000). This method is based on the Bayesian theory,

$$P(\boldsymbol{u} \mid \boldsymbol{R}) = \frac{P(\boldsymbol{R} \mid \boldsymbol{u})P(\boldsymbol{u})}{P(\boldsymbol{R})}, \tag{2.3.6}$$

where $P(\boldsymbol{a} \mid \boldsymbol{b})$ means the conditional probability density function of $\boldsymbol{a}$ when the event $\boldsymbol{b}$ occurs. The Bayesian theory tells us that the conditional probability of happening the state vector $\boldsymbol{u}$, when the observation $\boldsymbol{R}$ occurs, can be related with the conditional probability of $\boldsymbol{R}$ when the state vector $\boldsymbol{u}$ happens in conjunction with the probability of the state vector and that of observation vector in the statistical universe. In the MAP method, $\boldsymbol{u}$ is chosen so that the posterior probability $P(\boldsymbol{u} \mid \boldsymbol{R})$ becomes maximum under the condition that a priori information ($\boldsymbol{u}_a$), which is given by climatology etc, is already given. Assuming P follows the Gaussian distribution around the means, I can derive the following formulae for the MAP method:

$$\begin{aligned} P(\boldsymbol{R} \mid \boldsymbol{u}) &= P(\boldsymbol{f}(\boldsymbol{u}) + \boldsymbol{e} \mid \boldsymbol{u}) \\ &= P(\boldsymbol{e}) = \frac{1}{(2\pi)^{-m/2}\sqrt{|\mathbf{S}_e|}} \exp\left\{-\frac{1}{2}[\boldsymbol{u} - \boldsymbol{f}(\boldsymbol{u})]^{\mathrm{T}} \mathbf{S}_e^{-1} [\boldsymbol{u} - \boldsymbol{f}(\boldsymbol{u})]\right\}, \end{aligned} \tag{2.3.7}$$

$$P(\boldsymbol{u}) = \frac{1}{(2\pi)^{-n/2}\sqrt{|\mathbf{S}_a|}} \exp\left[-\frac{1}{2}(\boldsymbol{u} - \boldsymbol{u}_a)^{\mathrm{T}} \mathbf{S}_a^{-1} (\boldsymbol{u} - \boldsymbol{u}_a)\right], \tag{2.3.8}$$

where $\mathbf{S}_e$ and $\mathbf{S}_a$ are the measurement error covariance matrix and a priori covariance matrix. Organizing this non-linear equation such that $P(\boldsymbol{u} \mid \boldsymbol{R})$ becomes maximum, I obtain the following cost function,

$$\boldsymbol{\phi}_{\mathrm{MAP}} = [\boldsymbol{R} - \boldsymbol{f}(\boldsymbol{u})]^{\mathrm{T}} \mathbf{S}_e^{-1} [\boldsymbol{R} - \boldsymbol{f}(\boldsymbol{u})] + (\boldsymbol{u} - \boldsymbol{u}_a)^{\mathrm{T}} \mathbf{S}_a^{-1} (\boldsymbol{u} - \boldsymbol{u}_a). \tag{2.3.9}$$

For the condition of spatial smoothness of aerosol properties, I imposed the smoothing constraint to aerosol optical properties using Phillips-Twomey method, which solves a problem so that the vector is determined as a smooth function. In this method, I minimize the square of the second derivative of the solution, $\boldsymbol{u}$, for the spatial coordinates, $\boldsymbol{x}$, as

$$\int_{Nx} (u'')^2 \, dx = \min \int_{Nx} (u'')^2 \, dx, \tag{2.3.10}$$

$$\gamma \sum_k \left(u_{k-1} - 2u_k + u_{k+1}\right)^2 + \sum_k e^2 \rightarrow \text{minimum}, \tag{2.3.11}$$

where γ denotes smoothing factor or Lagrange multiplier, the second term is summation of errors. Then, the cost function of the smoothness condition is give as follows,

$$\phi_{\text{P-T}} = \sum_{ix} \gamma \left| \boldsymbol{B}_{ix} + \mathbf{D}_{ix} \boldsymbol{u} \right|^2 , \tag{2.3.12}$$

$$\boldsymbol{B}_x = \begin{bmatrix} \boldsymbol{u}_0 & 0 & 0 & \cdots & 0 & \boldsymbol{u}_{Nx+1} \end{bmatrix}^{\mathrm{T}} , \tag{2.3.13}$$

$$\boldsymbol{B}_y = \begin{bmatrix} \boldsymbol{u}_0^{\mathrm{T}} & 0 & 0 & \cdots & 0 & \boldsymbol{u}_{Ny+1}^{\mathrm{T}} \end{bmatrix}^{\mathrm{T}} , \tag{2.3.14}$$

$$\mathbf{D} = \begin{bmatrix} -2 & 1 & 0 & 0 & 0 & \cdot & \cdot & \cdot \\ 1 & -2 & 1 & 0 & 0 & \cdot & \cdot & \cdot \\ 0 & 1 & -2 & 1 & 0 & 0 & \cdot & \cdot \\ 0 & 0 & 1 & -2 & 1 & 0 & 0 & \cdot \\ \cdot & \cdot & \cdot & \cdot & \cdot & \cdot & \cdot & \cdot \end{bmatrix} , \tag{2.3.15}$$

where Eq. (2.3.12) is a vector representation of Eq. (2.3.11), $\boldsymbol{B}_{ix}$ and subscript *ix* mean the boundary conditions and the horizontal coordinates (x, y); T the transpose; **D** is the second differential coefficient matrix. As for the boundary condition to spatial direction, I use the values of the state vector for neighboring sub-domains, that are already retrieved in the sequence of the sub-domain by sub-domain analysis, for the boundary values for the sub-domain under analysis as shown in Fig. 2.3.7. If there are no adjacent sub-domains, I use prescribed values at border pixels of the sub-domain under analysis as a boundary condition.

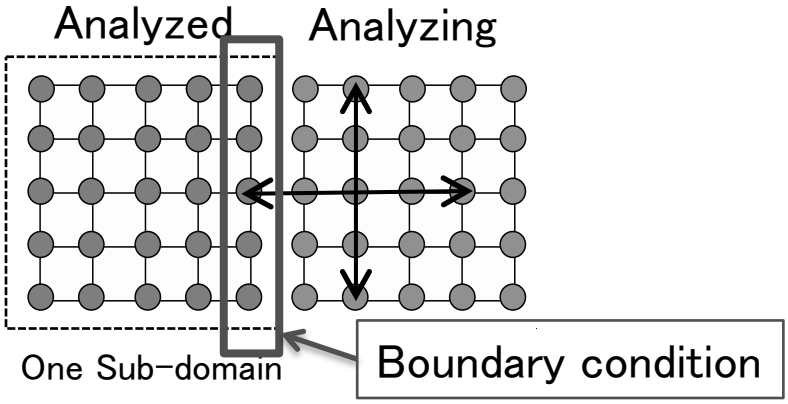

Figure 2.3.7 Boundary condition between sub-domains. Black circle denotes an observation point or pixel. One sub-domain bounded by dashed line indicates a sub-domain already analyzed in a sequence of the analysis, while the other is the target sub-domain under current analysis. The arrows show the analysis area around the center point. Values surrounded by a solid square are used for the boundary condition for the target sub-domain.

Then, the cost function to be minimized is expressed as the sum of those of MAP method and of Phillips-Twomey method:

$$\boldsymbol{\phi} = \boldsymbol{\phi}_{\mathrm{MAP}} + \boldsymbol{\phi}_{\mathrm{PT}} = [\boldsymbol{R} - \boldsymbol{f}(\boldsymbol{u})]^{\mathrm{T}} \mathbf{S}_e^{-1} [\boldsymbol{R} - \boldsymbol{f}(\boldsymbol{u})] + (\boldsymbol{u} - \boldsymbol{u}_a)^{\mathrm{T}} \mathbf{S}_a^{-1} (\boldsymbol{u} - \boldsymbol{u}_a) + \sum_{ix} \gamma \left| \boldsymbol{B}_{ix} + \mathbf{D}_{ix} \boldsymbol{u} \right|^2 \quad . (2.3.16)$$

The formula is a non-linear function of the state vector, so that I obtain the following equation in the tangential space to be iteratively solved by a Gauss-Newtonian method:

$$\boldsymbol{u}_{k+1} = \boldsymbol{u}_k + \left[(\mathbf{K}_k^{\mathrm{T}} \mathbf{S}_e^{-1} \mathbf{K}_k + \mathbf{S}_a^{-1}) + \sum_k \gamma_k \mathbf{H}_k \right]^{-1} \cdot \left\{ \mathbf{K}_k^{\mathrm{T}} \mathbf{S}_e^{-1} [\boldsymbol{R} - \boldsymbol{f}(\boldsymbol{u}_k)] - \mathbf{S}_a^{-1} (\boldsymbol{u}_k - \boldsymbol{u}_a) - \sum_{ix} \gamma_k (\mathbf{H}_{ix} \boldsymbol{u}_k + \mathbf{D}_{ix}^{\mathrm{T}} \boldsymbol{B}_{ix}) \right\}, \quad (2.3.17)$$

$$\mathbf{H} = \mathbf{D}^{\dagger} \mathbf{D}, \quad (2.3.18)$$

$$\mathbf{K} \equiv \nabla_x \mathbf{f}_{\mathrm{model}} = \begin{pmatrix} \mathbf{k}_{111} & \mathbf{0} & \mathbf{0} & & \mathbf{0} \\ \mathbf{0} & \mathbf{k}_{211} & \mathbf{0} & & \mathbf{0} \\ \mathbf{0} & \mathbf{0} & \mathbf{k}_{311} & & \mathbf{0} \\ & & & \ddots & \\ \mathbf{0} & \mathbf{0} & \mathbf{0} & \mathbf{0} & \mathbf{k}_{n_x n_y n_t} \end{pmatrix}, \quad (2.3.19)$$

$$\boldsymbol{\varepsilon} = \sqrt{\left(\frac{\boldsymbol{f}\left(\boldsymbol{u}_{\mathrm{retrieved},k}\right)}{R^{\mathrm{meas}}} - 1 \right)^2}, \quad (2.3.20)$$

where $\boldsymbol{u}_k$ is the solution at the k-th iteration step; **K,** the Jacobian matrix, $\partial \boldsymbol{f} / \partial \boldsymbol{u}$; $\boldsymbol{\varepsilon}$ is the root mean square error (RMSE). I use a logarithmic scale for all the parameters to prevent $\boldsymbol{u}$ from having a negative value.

Using this scheme, I retrieve aerosol properties of a certain area as defined as a sub-domain at once. In detail, I define a 5×5 pixel region, in which aerosol optical properties are distributed smoothly, as a sub-domain in the target area as shown in Fig. 2.3.8, and retrieve aerosol parameters, $\boldsymbol{u}$, at each pixel in a sub-domain. After that, I solve the next sub-domain, using the solutions already derived in the adjoining sub-domain as boundary condition to guarantee the smoothness between sub-domains.

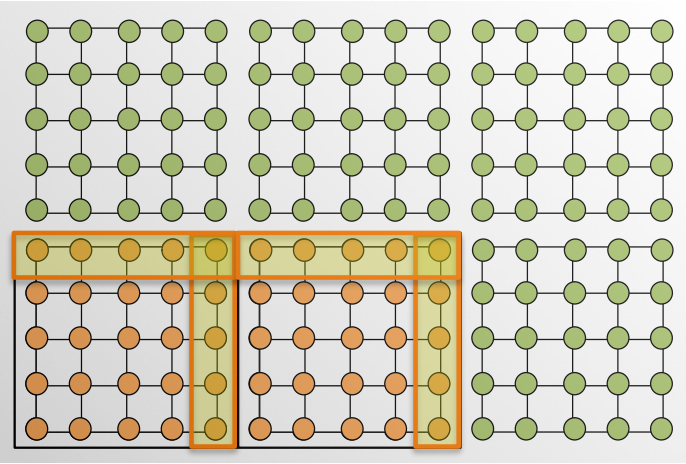

Figure 2.3.8　Target area for retrieval with a smoothly distributed aerosol layer. Green and orange points demote observation pixels. Each 5×5pixel region is defined as a sub-domain where an inversion procedure is conducted simultaneously. Orange square region represents boundary condition for neighboring sub-domains.

2.4 Description of forward model

2.4.1 Radiation transfer model

With the progress of computing technology, a direct use of radiation transfer calculation has been employed for solving non-linear remote sensing problems taking place of look up table (LUT) methods, as shown by successful examples of a flexible and accurate remote sensing (Dubovik et al., 2011). This method has being combined with radiation transfer calculation numerically solved each time in the iteration process of solution search without using LUT. The merit of directly using radiation transfer model is that it is easy to change retrieval parameters, or wavelengths, so it is possible to apply other satellite data; easy to change aerosol models in accordance with the situation; more accurate multiple scattering calculations in more realistic atmospheric conditions are available, so more accurate and flexible retrievals can be expected. However, it has also weak point that it takes a large computation time compared to that with LUT method.

I incorporate a radiation transfer model, RSTAR (Radiance System for Transfer of Atmospheric Radiation) developed at the University of Tokyo (Nakajima and Tanaka, 1986, 1988), which can simulate radiation fields in the atmosphere-land-ocean system at wavelengths between 0.167 and 1000 μm. Transfer engine is a Discrete-Ordinate method with several truncation method of particle phase function developed by Nakajima and Tanaka (1986). This model assumes a plane parallel atmosphere divided into several homogeneous sub-layers, and is capable of multiple

scattering calculations assuming atmospheric gases, aerosol particles and clouds. For the gaseous absorption, the non-linear fitting correlated k-distribution method (Sekiguchi *et al*., 2008) is used, and major seven gases (H2O, CO2, O3, N2O, CO, CH4, O2) are treated using the absorption line data of HITRAN2004. For the scattering calculation, it takes into account spherical and non-spherical particles (Dubovik et al., 2002; Yang et al., 2000, 2005; Ishimoto et al., 2010). It also takes into account hydroscopic growth of particles (Shettle and Fenn, 1979). It is implemented rapid computation methods by DM, TSM, and IMS schemes (Nakajima and Tanaka, 1988).

I implemented the radiative transfer model as the forward model. In other word, I adopted the radiative transfer model as a function of $\boldsymbol{u}$ (i.e. $\boldsymbol{f}(\boldsymbol{u})$). The radiative transfer calculation is performed in the calculations of initial values using several initial conditions and Jacobian matrix, and in the update process of retrieved reflectances by Eq. (2.3.17) using inverted values of the state vector, as shown in Fig. 2.4.1.

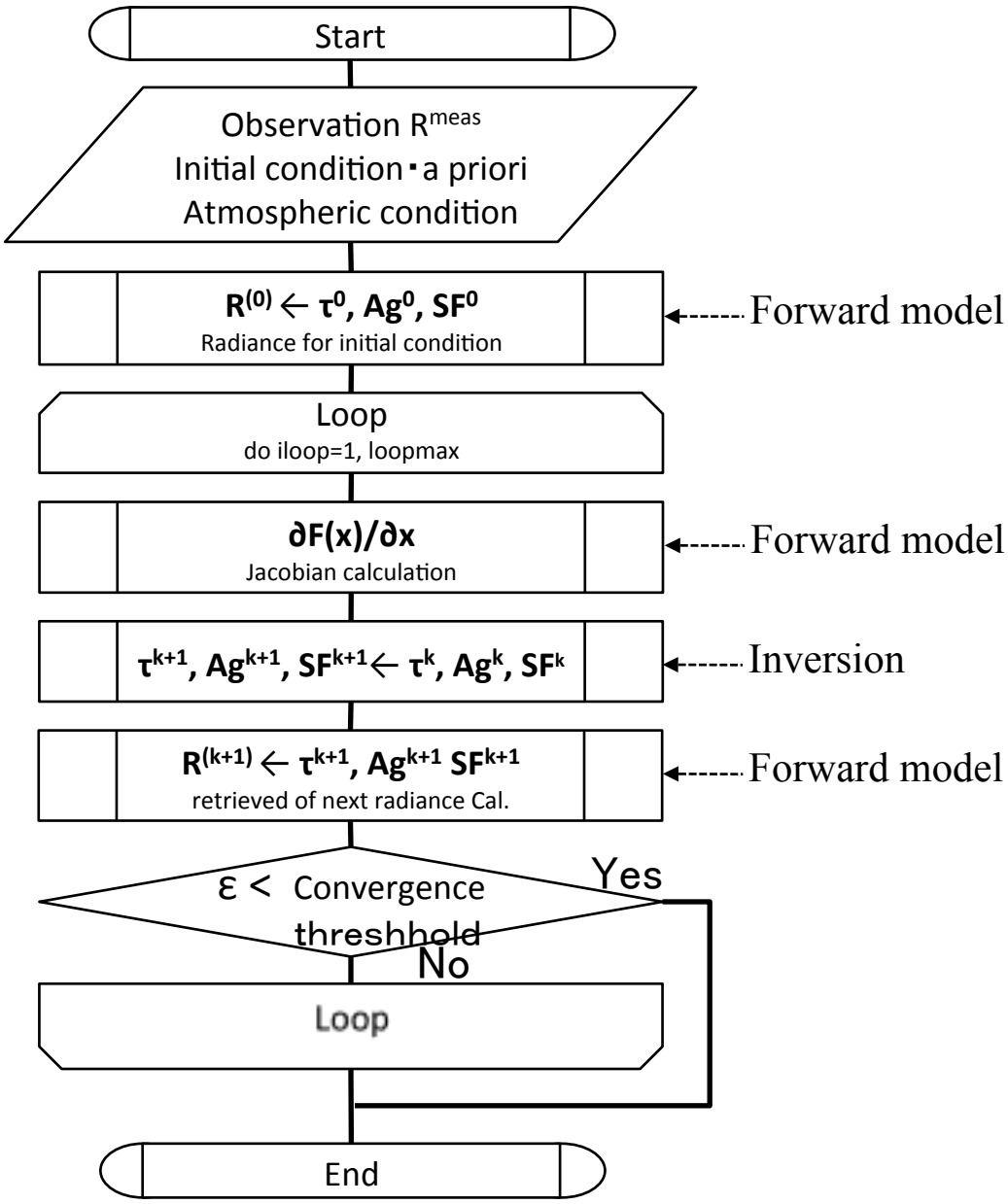

Figure 2.4.1 Flow chart of the present method.

2.4.2 Polarization Correction

I need to take into account the polarization effects for calculation of radiances in blue to near UV spectral region. Direct use of the full vector radiative transfer version of RSTAR called PSTAR (Ota et al., 2010) is one solution to this problem, but the computational burden further increases to solve the full vector radiative transfer in the iterative solution search of which computational burden is also not small. In this situation I adopt a method of applying a correction to the RSTAR-calculated radiances by a polarization correction scheme of Ogawa et al. (1989). Polarization correction is as follows,

$$L = L_{scalar} + \Delta L, \tag{2.4.1}$$

$$L(\mu, \mu_0; \phi - \phi_0; \tau, \tau_0) = L_{scalar}(\mu, \mu_0; \phi - \phi_0; \tau, \tau_0) + \Delta L(\mu, \mu_0; \phi - \phi_0; \tau, \tau_0), \tag{2.4.2}$$

$$\Delta L(\mu, \mu_0; \phi - \phi_0; \tau, \tau_0) = \sum_{m=0}^{M} \Delta L^m(\mu, \mu_0; \tau, \tau_0) \cos m(\phi - \phi_0), \tag{2.4.3}$$

where L is corrected radiance; L_{scalar} is a radiance calculated by a scalar radiative transfer code; the subscript "scalar" means radiation model-calculated quantities without polarization; ΔL, additional sky radiance caused by polarization effects.

I compared values of the apparent reflectance $R = (\pi L) / \mu_0 F_0$ calculated by RSTAR with polarization correction and by PSTAR. I compared results under following conditions: ground surface albedo A_g: 0.05, 0.5, 0.9, solar zenith angle θ_0: 0 ~ 70°, satellite zenith angle θ: 110 ~ 180°, satellite azimuth angle relative to the sun φ: 0 ~ 180 degree, and AOT τ: 0.0. The result shows that the difference between RSTAR and PSTAR radiances is within 2% in a solar zenith angle range from 0 degree to 60 degree. I show the result of the comparison with PSTAR in Appendix I.

2.5 Summary

I formulated equations and process schemes for the multi-wavelength and multi-pixel remote sensing algorithm for aerosols incorporating radiative transfer model directly. The algorithm is a combination of an optimal method (MAP method) and Phillips-Twomey method, and retrieves several aerosol parameters of all pixels in a sub-domain area simultaneously. I presented how the area of analysis is divided into sub-domains and how the sub-domain results of analysis are connected by a boundary condition between adjacent sub-domains.

I added polarization correction to the radiative transfer model, and found the difference from the radiance calculated by a full vector radiative transfer model is within 2% when the solar zenith angles are from 0 to 60°.

In the next chapter, I will show the result of numerical experiments of retrieval simulation and investigate retrieval accuracy using the present new algorithm.

Chapter 3 Numerical Test

3.1 Introduction

In this chapter, I conducted numerical experiments to test the algorithm and to investigate retrieval accuracy of aerosol properties and ground surface albedo assuming GOSAT/TANSO-CAI imager data. The important point of this test is to investigate a retrieval accuracy of aerosol properties in the land area where surface reflectance is spatially heterogeneous like urban area. The result of the experiment showed that AOTs of fine mode and coarse mode (dust), soot fraction and ground surface albedo are shown in Section 3.2. I discussed in Section 3.2.2 the accuracy of the algorithm in terms of several land surface types, especially inhomogeneous surface in the horizontal direction.

3.2 Numerical test of homogeneous and inhomogeneous surfaces

One feature of the present algorithm is the simultaneous retrieval of aerosol properties of all observed pixels involved in each of sub-domains composing the analysis area. On the other hand, previous satellite remote sensing methods retrieve aerosol parameters from information contained in radiances in one pixel. The region composed of several pixels generally includes different surface reflectance. I conducted numerical experiments and retrieved simulated observation data assuming an observation of GOSAT/TANSO-CAI imager sensor (See Chapter 4), to investigate the accuracy of retrieval parameters derived by this method with respect to both spatially homogeneous and inhomogeneous albedo surfaces.

3.2.1 Experimental Setting

For the numerical experiment, I defined a 5×5 pixel region as one sub-domain that is an area of analysis at once by this algorithm (Fig. 3.2.1).

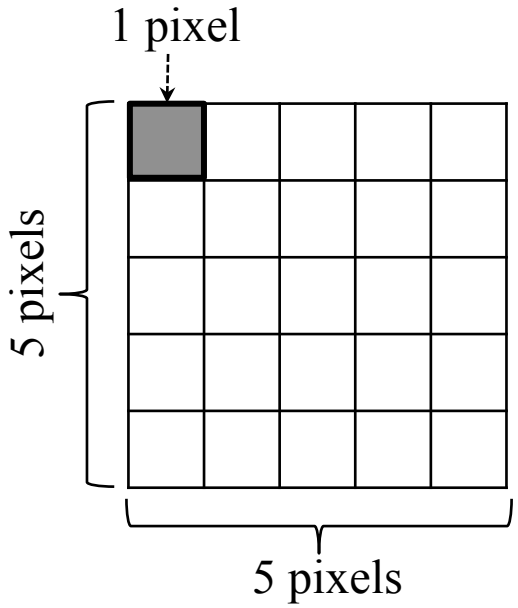

Figure 3.2.1 Definition of the sub-domain (5×5 pixel region) that is an area analyzed at once by the present algorithm

Retrieval parameters are AOTs for fine and coarse aerosol modes (AOT(fine) and AOT(coarse)), volume soot fraction (SF) and the ground surface albedo (A_g). I simulated observation data using RSTAT assuming observation by GOSAT/TANSO-CAI imager sensor. TANSO-CAI has four observation bandswith center wavelengths of 380, 674, 870 and 1600nm. I assumed monochromatic observation at all four wavelengths, and observation geometries are given as follows: solar zenith angles θ_0= 27-28°, satellite nadir angles θ= 150-152°, satellite azimuth angle relative to the solar position ϕ= 148-150°.

I set AOT(fine) = 0.1 (or 0.3), AOT(coarse) = 0.1 (or 0.3) and SF = 0.1 for aerosol parameters, and set each type of surface albedo (e.g. deciduous, dry grass, snow, sea water, desert and urban) for each wavelength, and make a simulated observation dataset for a 5×5 pixel using RSTAR.

I conducted numerical test assuming following six types of land surfaces: deciduous (or vegetation), dry grass, snow, sea water, desert and urban. The surface albedo or reflectance of each surface type except for urban are given by the Aster spectral library data (Aster spectral library; http://speclib.jpl.nasa.gov/yori) as shown in Fig. 2.3.2. For the urban region where bright and dark surfaces are mixed, I assumed heterogeneous urban-like sub-domain as shown in Fig. 3.2.2. I utilized water and snow surface albedo of Aster spectral library as representatives of dark and bright surfaces. This model might be too simplified with extremely dark and bright surfaces, but it can serve as a test model to prove the advantage of multi-pixel method. It looks like a checker board, and I hereafter called it *urban-like* or *checkerboard* surface.

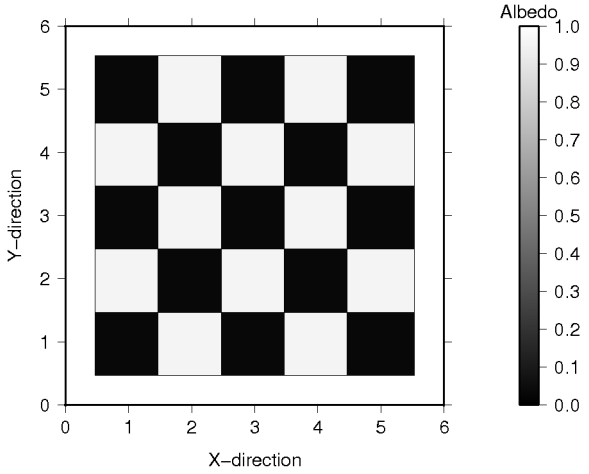

Figure 3.2.2 A sub-domain model for spatially heterogeneous urban-like surface.

In the analysis, I tested this algorithm putting several values into experimental parameters, such as error in measurement, measurement error covariance (S_e), a priori value of each retrieval parameter (u_a), a priori covariance (S_a) and smoothness factor (γ) for each retrieval parameter, to investigate the retrieval accuracies in several conditions, as listed in Table 3.2.1 and 3.2.2. I gave 0.1, 0.5 and 1.0 for the smoothness factor (γ) of the aerosol spatial distribution. On the other hand, it is not reasonable to assume that surface albedo is smoothly distributed spatially in comparison with the aerosol case; in other words, the surface albedo is spatially heterogeneous, so that I set 0 to γ for the surface albedo at all four wavelengths, although the formulation in this study allow us a non-zero value. For one set of test calculations, I prepared 50 patterns. The maximum number of iterations in solution search is set at 10 times.

Table 3.2.1 Observation error assumed in the simulated measurement reflectance (R), and given error covariance (S_e) for numerical test.

Wavelength [nm]	380	674	870	1600
Error put in R	-2% ~ +2%	-2% ~ +2%	-2% ~ +2%	-2% ~ +2%
Error covariance (S_e)	2%	2%	2%	2%

Table 3.2.2 Experimental parameters, a priori information (u_a, S_a) and smoothness factor (γ) , in numerical test

Retrieval parameters	AOT (fine)	AOT (coarse)	Soot fraction (SF, f_s)	Ag
A priori (u_a)	-150% ~ +150% of the true value	-150% ~ +150% of the true value	-150% ~ +150% of the true value	-110% ~ +110% of the true value
A priori covariance (S_a)	Δu = ±0.5	Δu = ±0.5	100%	Δu = ±0.1
Smoothness factor (γ)	0.1, 0.5, 1.0	0.1, 0.5, 1.0	0.1, 0.5, 1.0	0

3.2.2 Results and discussion of numerical experiments in areas of various surface types

I first study the convergence of solutions in the numerical tests at γ =0.1, 1.0 in indicated in Fig. 3.2.4. I define the convergence error (RMSE) as

$$\varepsilon = \sqrt{\left(\frac{f\left(\boldsymbol{u}_{\text{retrieved},k}\right)}{R^{\text{meas}}} - 1 \right)^2}, \qquad (3.2.1)$$

where $\{\boldsymbol{R}_{meas}\}$ is measured reflectances and $\{\boldsymbol{u}_{retrived,k}\}$ is a solution of the state vector in the k-th iteration. Figure 3.2.3 shows that most of all calculation conversed at about 6 time iterations with RMSE reaching a value less than 5% and close to the assumed observation error of 2%. Another noticeable fact in Fig. 3.2.4 is that the convergence of the solution is faster in the test with large smoothing condition, γ= 1.0, than that with γ= 0.1. This phenomenon can be reasoned by that the freedom of the inverse problem is smaller for γ= 1.0 than that for γ= 0.1, because the aerosol layer less varies spatially in the former case.

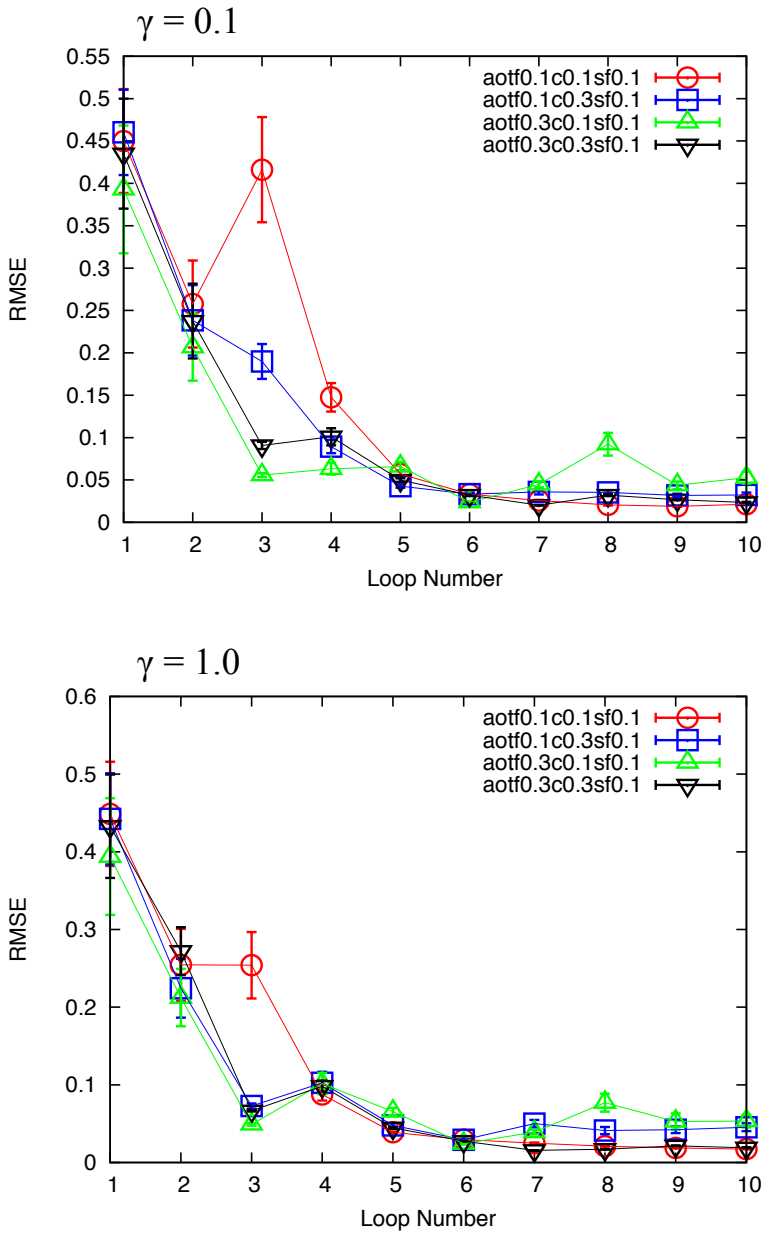

Figure 3.2.3 Top panel is averaged conversion result at GMA=0.1. Bottom panel at GMA=1.0. Error bar is the standard deviation. Given AOT sets of (fine, coarse) are (0.1,0.1), (0.1,0.3), (0.3,0.1) and (0.3,0.3). Given soot fractions are 0.1 and 0.2. Y-axis is RMSE; X-axis (Loop number) denotes means iteration number.

I study in Figs. 3.2.4 to 3.2.6 the behavior of errors included in the retrieved parameters in results of the numerical experiment in several surface types. In the figures, I show the average retrieval error (ME or $\Delta\overline{u}$) and standard deviation (σ) as defined,

$$\Delta\overline{u} = \pm\frac{1}{N}\sum_{i=1}^{N}\left|u_{retrieved,i} - u_{true}\right|$$

$$\text{if } \begin{cases} \sum_{i=1}^{N}(u_{retrieved,i} - u_{true}) > 0, \ \Delta\overline{u} > 0 \\ \sum_{i=1}^{N}(u_{retrieved,i} - u_{true}) < 0, \ \Delta\overline{u} < 0 \end{cases}, \tag{3.2.2}$$

$$\sigma = \sqrt{\frac{1}{N}\sum_{i=1}^{N}(\Delta u_{retrieval,i} - \Delta\overline{u})^2}\,, \tag{3.2.3}$$

$$N = N_{\text{pixel}} \times N_{\text{test}}\,, \tag{3.2.4}$$

where N_{pixel} and N_{test} are the number of pixel and experiment, respectively. $u_{\text{retrieved}}$ and u_{true} denote retrieved and true value of AOT(fine), AOT(coarse) and SF, respectively. I average the errors for γ =0.1, 0.5 and 1.0. From the result, differences from true vales of AOT(fine), AOT(coarse) and SF are large in snow surface type (i.e., homogeneous bright surface) for all γ cases . This result shows that it is difficult to retrieve aerosol properties accurately over all bright and homogeneous surfaces by using the present algorithm, as is usually said. On the bright or high reflectance surface, the transmitted sunlight mostly reflected at the surface, and then the reflected light is multiply scattered in the atmosphere again, so it is difficult to extract the reflectance affected by aerosols from measured reflectance. In the case of uniform surface types except, for snow surface, AOT(fine), AOT(coarse), soot fraction (SF) and surface albedo (Ag) can be retrieved within the error of 0.05, 0.05, 0.01 (~10%), 0.1 for all three γ cases, and ME does not significantly depend on γ. On the other hand, in the urban-like surface case, the retrieval error at γ =0.1 is large and similar to snow homogeneous surface, but at γ =0.5 and 1.0, the retrieval errors in aerosol properties such as AOT(fine), AOT(coarse) and SF are smaller than those at γ =0.1, and difference from true values are within 0.03, 0.05, 0.005 (~5%), 0.05. This result may be explained as that the inverse problem of the aerosol parameters becomes more stable as smoothness of the spatial aerosol distribution increases with increasing γ-value and sensitivities of the cost function to AOTs and SF increase as a result of the synergetic cooperation of information contents included in the observed reflectances over bright and dark surface as discussed in Section 2.2.2.

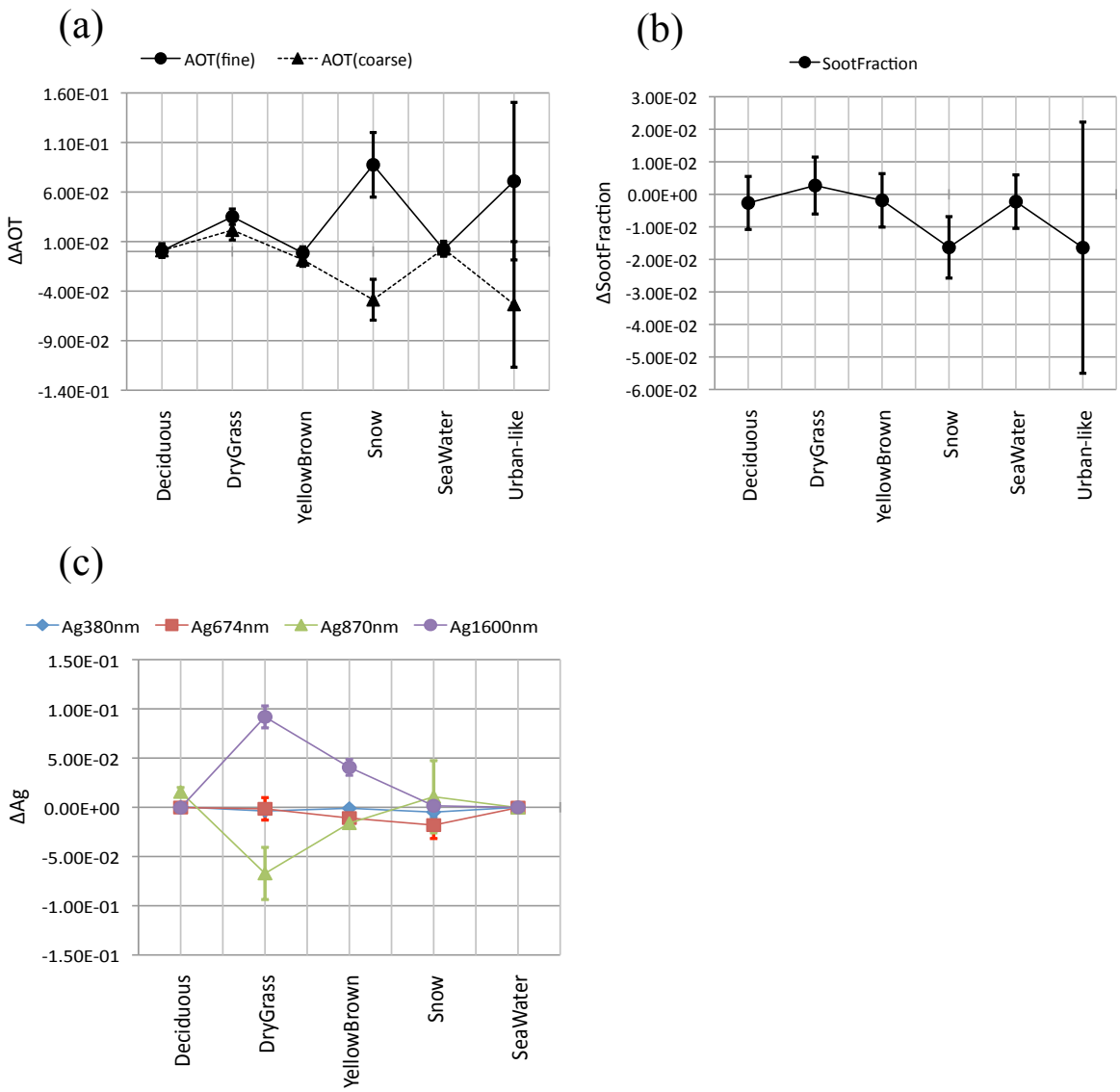

Figure 3.2.4 Mean error (ME) and standard deviation (error bar) of each retrieved parameter under different surface types (Deciduous, dry grass, yellow brown, snow, sea water and urban-like) at γ= 0.1. Results of (a) AOT(fine) and AOT(coarse), (b) Soot fraction (SF), (c) ground surface albedo (Ag) of each wavelength.

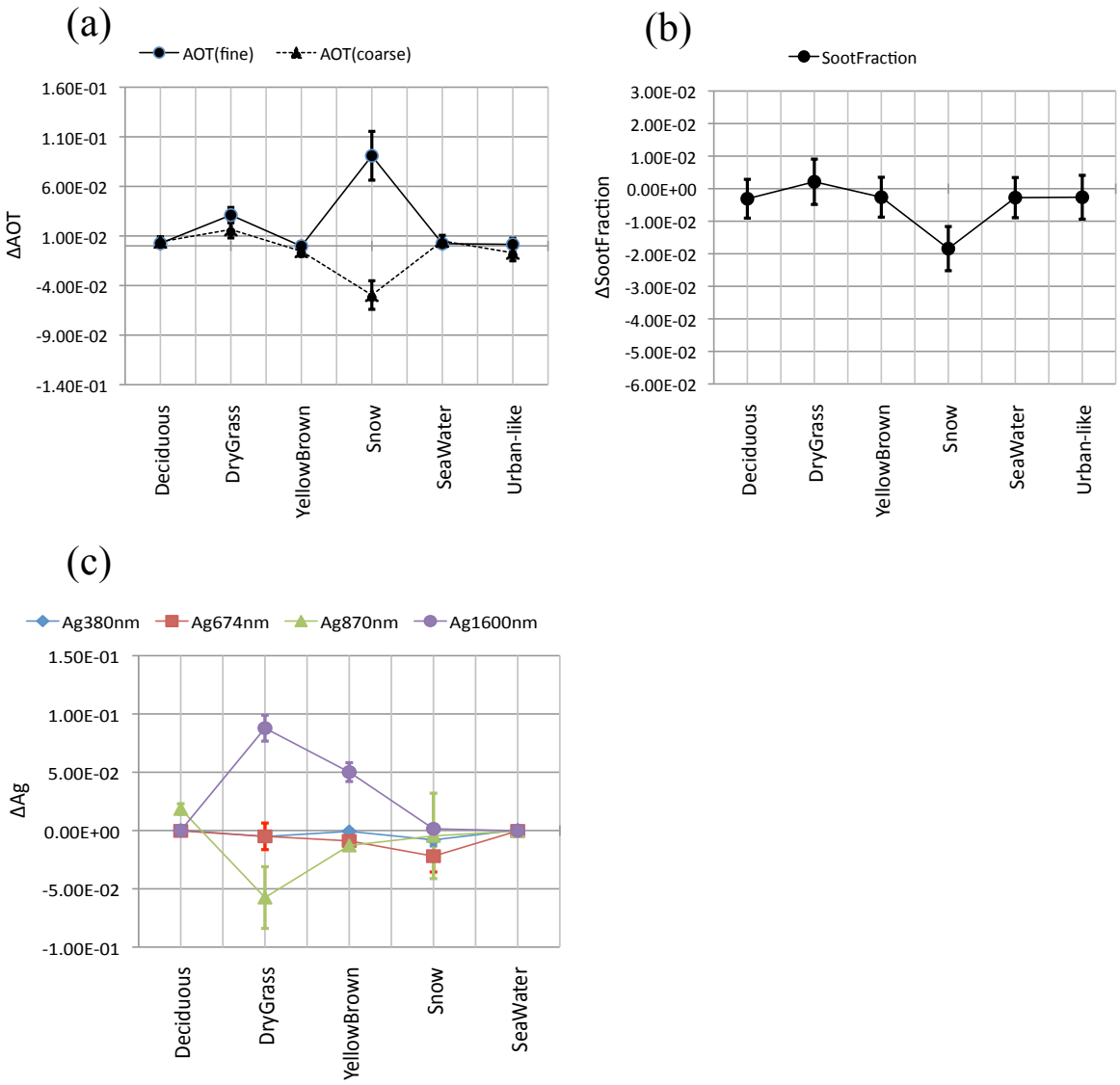

Figure 3.2.5 Same as in Fig. 3.2.4 but for gamma=0.5.

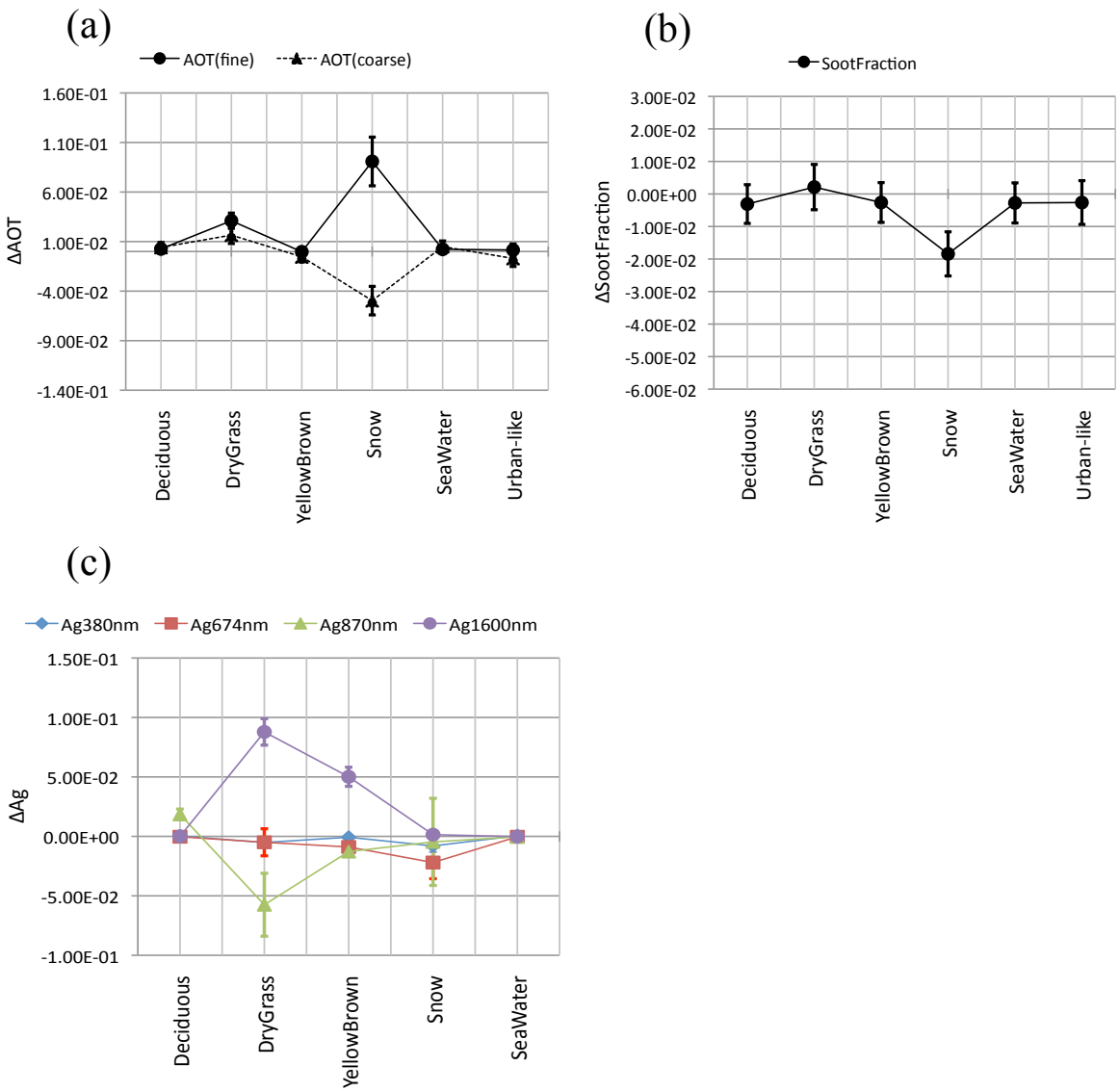

Fig 3.2.6 Same as in Fig. 3.2.4 but for gamma=1.0.

In order to study the above-stated speculation for the increased accuracy of aerosol retrievals for large γ-values, Fig. 3.2.7 shows the results of different γ in urban-like surface type. Each dot of the plot indicates all pixel results in the case of urban-like surface. The x-axis denotes percentage difference between a priori value and true value, and the y-axis of the figure is the value of difference between retrieval value and true value. If the results distribute along a line in the figure, it means that the retrieval parameter does not have a sensitivity to observed reflectance and is difficult to be retrieved. In the case of weak smoothing constraint, i.e., γ =0.1, which is similar to the case of single pixel analysis, the variation and error of AOT(fine), AOT(coarse) and SF is larger. Furthermore, the several results of SF in γ =0.1 distribute along a priori slope. The result in the case of γ =0.1 in the figure shows that AOT retrieval is difficult in the bright (snow) surface, and SF retrieval is difficult in the dark (sea water) surface and there are small sensitivity in SF in dark surface. On the contrary, it is found that the increased spatial homogeneity of aerosol properties with γ =0.5 and 1.0 help retrieved aerosol parameter to converge to the most likely values without much dependence on the a priori constraint.

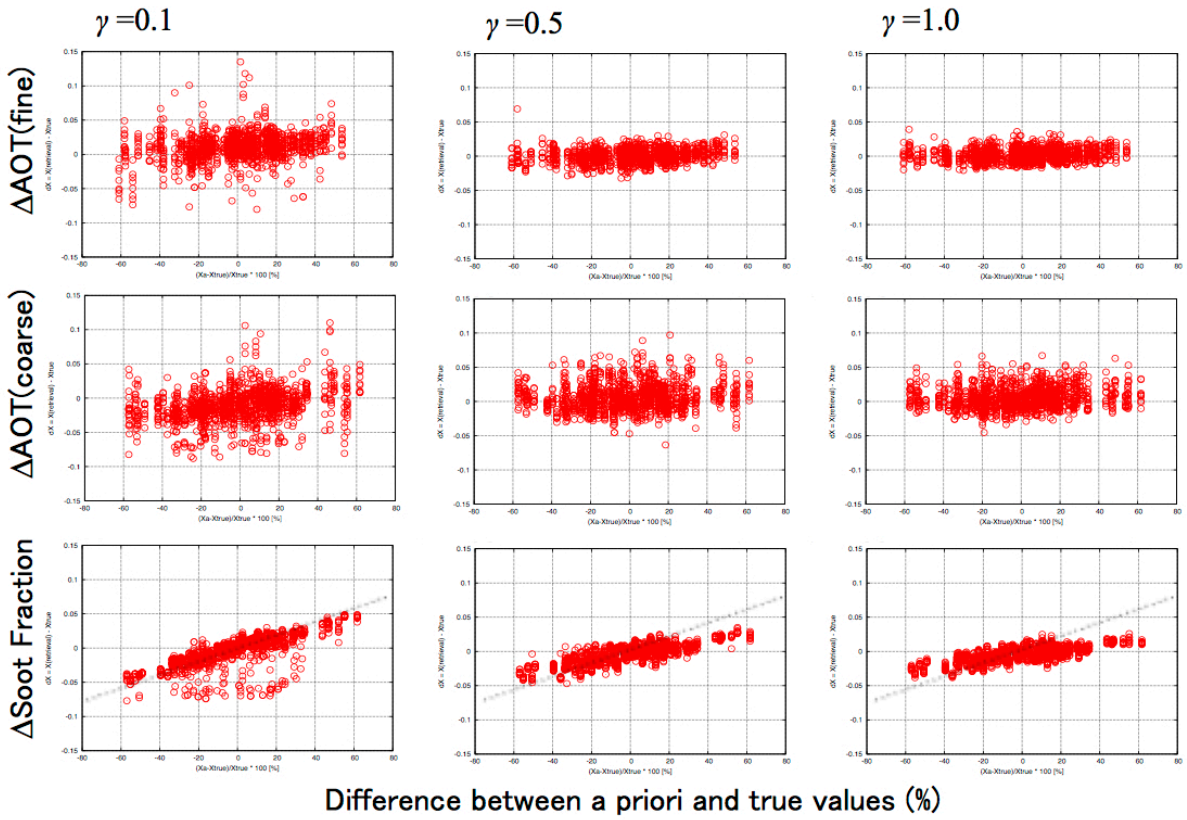

Figure 3.2.7 Retrieval errors of aerosol parameters, AOT(fine), AOT(coars) and FS, for urban-like surface. All plot of results of numerical tests at different smoothness factors, γ = 0.1, 0.5 and 1.0. X-axis is a percentage difference between a priori and true values. Y-axis is a difference between retrieved and true values. Top panels show the result for AOT(fine); middle panels for AOT(coarse); bottom panels for soot Fraction (SF). Linear lines in the SF results denote the expected retrieval error when the retrieval errors are determined only by a priori information. If the result alines with the line, the measurement does not have sensitivity to the retrieval parameter.

Figure 3.2.8 shows similar plots as in Fig. 3.2.7 but for sea water (dark) surface, snow (bright) surface and urban-like (heterogeneous) surface types at γ =1.0. We can see AOTs are accurately retrieved in dark surface case, whereas AOTs are not determined in bright surface case. On the other hand, AOT(fine), AOT(coarse) and SF can be determined in urban-like surface case within about ±0.03, ±0.05 and ±5%, respectively. This result again support my speculation of the synergetic cooperation of bright and dark surface to increase the sensitivities of the inverse problem to all the aerosol parameters I set, i.e., AOT(fine), AOT(coarse), and SF. In the cases of Fig. 3.2.8, I imposed the condition that the aerosols and their properties are smoothly distributed in the horizontal direction or are almost homogeneous between pixels adjacent to each other by giving γ =1.0.

In this regard, I should note that AOT and SSA have their unique spectra different from those of the ground albedo as shown in Fig. 2.3.2, so that simultaneous solution for multi-pixel satellite observation of different surface types significantly helps the aerosol retrievals under the assumption of strong smoothness condition (a large γ-value). In conclusion, simultaneous solution of the inverse problems in the region that includes different reflectances in the spatial and spectral dimensions improve the retrieval accuracy of aerosol parameters such as AOT(fine), AOT(coarse) and SF.

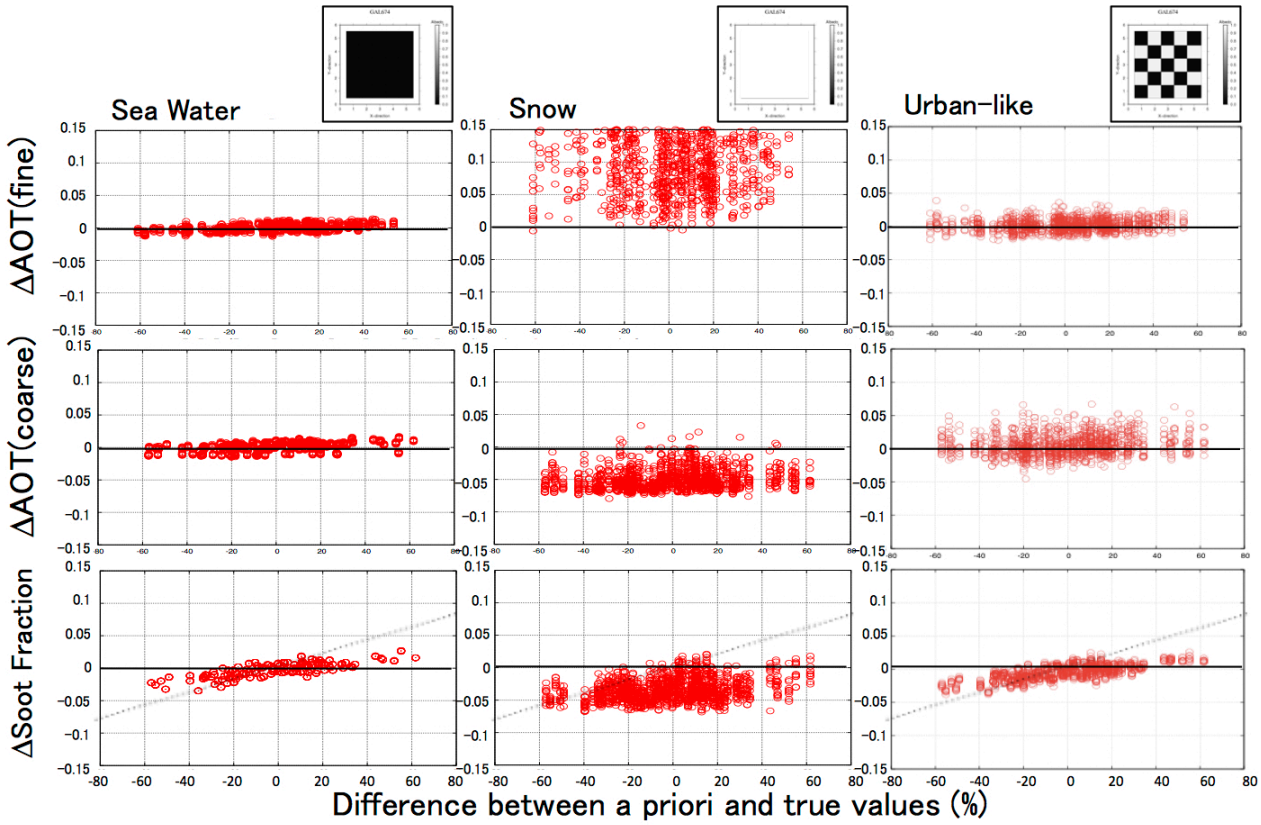

Figure 3.2.8 Same as Fig. 3.2.8 but for sea water, snow, and urban-like surface types at smoothing factor γ = 1.0.

Figure 3.2.9 shows the weighting function for AOT(fine), AOT(coarse) and SF as defined as

$$\mathbf{K}\Big|_{u_i} = \nabla_u \boldsymbol{f}(\boldsymbol{u})\Big|_{u_i} = \frac{\partial f_\lambda(\boldsymbol{u})}{\partial u_i}. \qquad (3.2.2)$$

This figure presents the rate of change in the apparent reflectance with respect to a change in retrieved parameters. From the figure, it is found that the sensitivity is different for different types of surface and wavelength, i.e. different surface reflectance. Sensitivity to AOT(fine) in snow (bright) surface case is negative, while that at sea water (dark) surface case has a positive value. This opposite sensitivities can be explained by the characteristic relationship between surface albedo and observed reflectance as described by Eq. (2.2.11) in chapter 2. It should be noted that the surface albedo is low at 1.6μm as water surface bringing the weighting functions close to those of sea water. As for AOT, sensitivity is different between fine and coarse mode in sea surface case, then it is easy to retrieve AOT(fine) and AOT(coarse) separately if I combine observations at different wavelengths. It is interesting to see that the sensitivity of AOT in vegetation cases change the signs in NUV to blue and red to NIR spectral regions, so that AOT(fine) and AOT(coarse) can be retrieved in the vegetation cases. Similarly we can use AOT sensitivity difference between snow (bright) and sea water (dark) surface. On the other hand, retrieval of SF is difficult for all the surface types. It is found, however, the sensitivity of SF at a wavelength of 380nm in snow surface case is about −5% and it is larger than measurement error 2%, indicating that the SF retrieval is possible but needs 380nm. Therefore, it is likely that AOT(fine), AOT(coarse) and SF could be determined in the checkerboard or urban-like surface case (i.e. spatially heterogeneous surface case).

I represent the sensitivity of measurement for SF in different AOT and surface albedo (Ag) for the case that Ag is uniform in wavelength and spatial direction in Fig. 3.2.10. The figure shows that the sensitivity for SF becomes larger with increase of AOT or surface albedo. Especially the sensitivity is large when surface albedo exceeds 0.4 and AOT larger than 0.4. Therefore, it is likely that AOT(fine), AOT(coarse) and SF are able to retrieve simultaneously even over moderately bright pixel in urban-like surface case in the turbid atmosphere with AOT larger 0.4 by use of multi-wavelength and multi-pixel information.

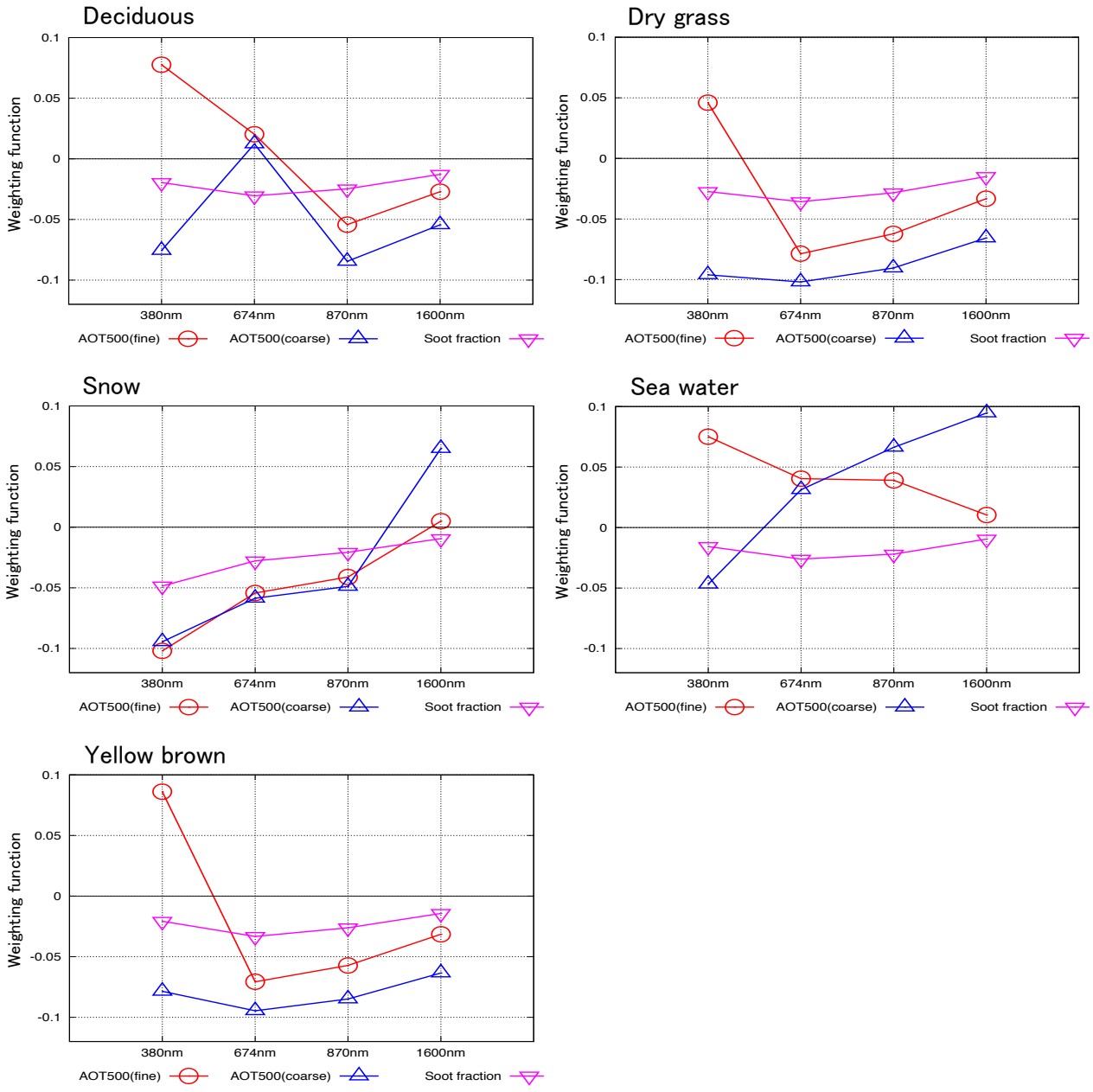

Figure 3.2.9 Weighting functions of the apparent reflectance for retrieved parameters, AOT(fine), AOT(coarse), and SF, at single pixel for several surface types (deciduous, dry grass, snow, sea water and yellow brown), in the case of AOT(fine)= 0.1, AOT(coarse)= 0.1, and SF= 0.1. Red-colored line denotes the sensitivity for AOT(fine), blue for AOT(coarse), and pink for soot fraction at four CAI-sensor wavelengths.

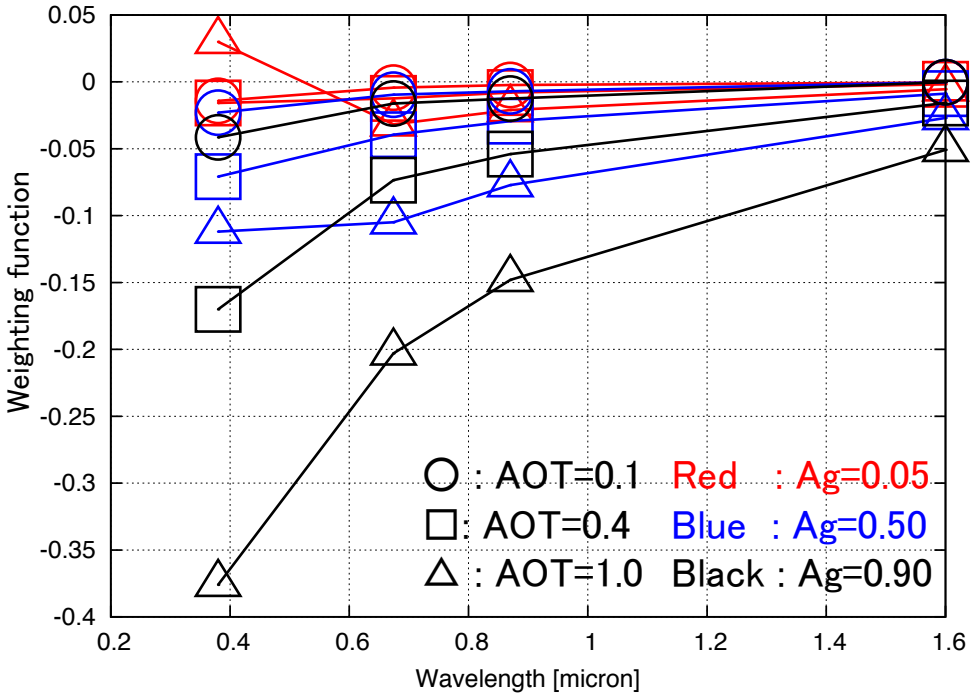

Figure 3.2.10 Weighting function of soot fraction (SF) for Apparent reflectance of different AOT and Ag for four CAI wavelengths for the case that Ag is uniform in wavelength and spatial direction. Results for AOT= 0.1 (○), AOT=0.4 (□), AOT=1.0 (△); red-color for Ag=0.05, blue for Ag=0.50, black for Ag=0.90.

3.2.3 Results of several surface patterns

In the previous section, I studied the effectiveness of this method in the inhomogeneous surface region. In this section, I show retrieval results of several surface patterns. Calculation conditions are same as Tables 3.2.1 and 3.2.2, but smoothness factors of aerosol parameters are fixed at $\gamma = 1.0$. For one set of calculations, I calculated 50 patterns. I show the true values and retrieval values averaged by all calculation of each pixel.

Figures 3.2.11a and 3.2.11b show the horizontal distributions of true and retrieved state vectors in an experiment of a homogeneous aerosol layer on a urban-like surface with the true values of AOT(fine)=0.3, AOT(coarse)=0.3, SF=0.1, and A_g for sea water and snow surfaces of the Aster spectral library (Fig. 2.3.2). The figure indicates that the horizontal distributions of aerosol parameters and surface albedo are successfully retrieved without a large error, other than a large error at the corner pixels of retrieved SF values. Retrieval of the state vectors at border pixels, especially corner pixels, are difficult without a suitable boundary condition to be posed when the sub-domain is isolated without neighbor sub-domains as in the present experiment.

Figures 3.2.12a and 3.2.12b are similar plots as in Figs. 3.2.11a and 3.2.11b but for a step-wise aerosol layers on a homogeneous surface. The two AOT values to define the step-function are assumed as AOT(fine)=0.1 and 0.2 for fine mode aerosols, and AOT(coarse)=0.1 and 0.4 for coarse mode aerosols. Soot fraction is assumed to be SF=0.1; The surface albedo of the homogeneous surface to be those of the sea water type of the Aster spectral library. It is found from the figure that the a blurred AOT distribution with spreaded boundary is obtained with large errors around the edge of the step-wise distribution under the strong smoothing condition of γ=1.0. It is, therefore, the γ-value should be tuned so as to produce optimized horizontal distributions of aerosol layers depending on the applications.

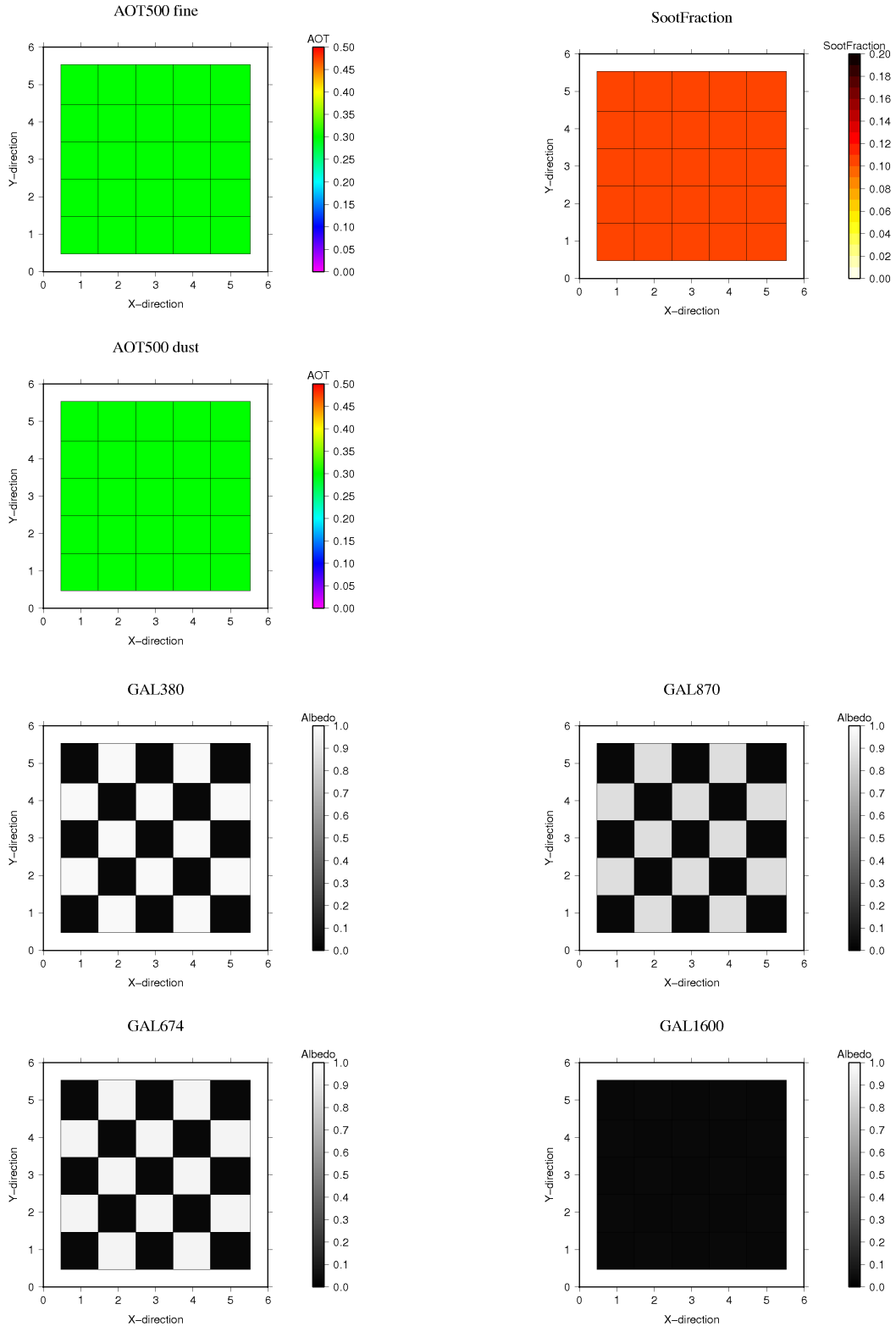

Figure 3.2.11a Grid maps of the true state vector values for the experiments in a sub-domain. True values are AOT(fine)=0.3, AOT(coarse)=0.3, and SF=0.1; Urban-like Ag at all four wavelengths (380, 674, 870, 1600nm).

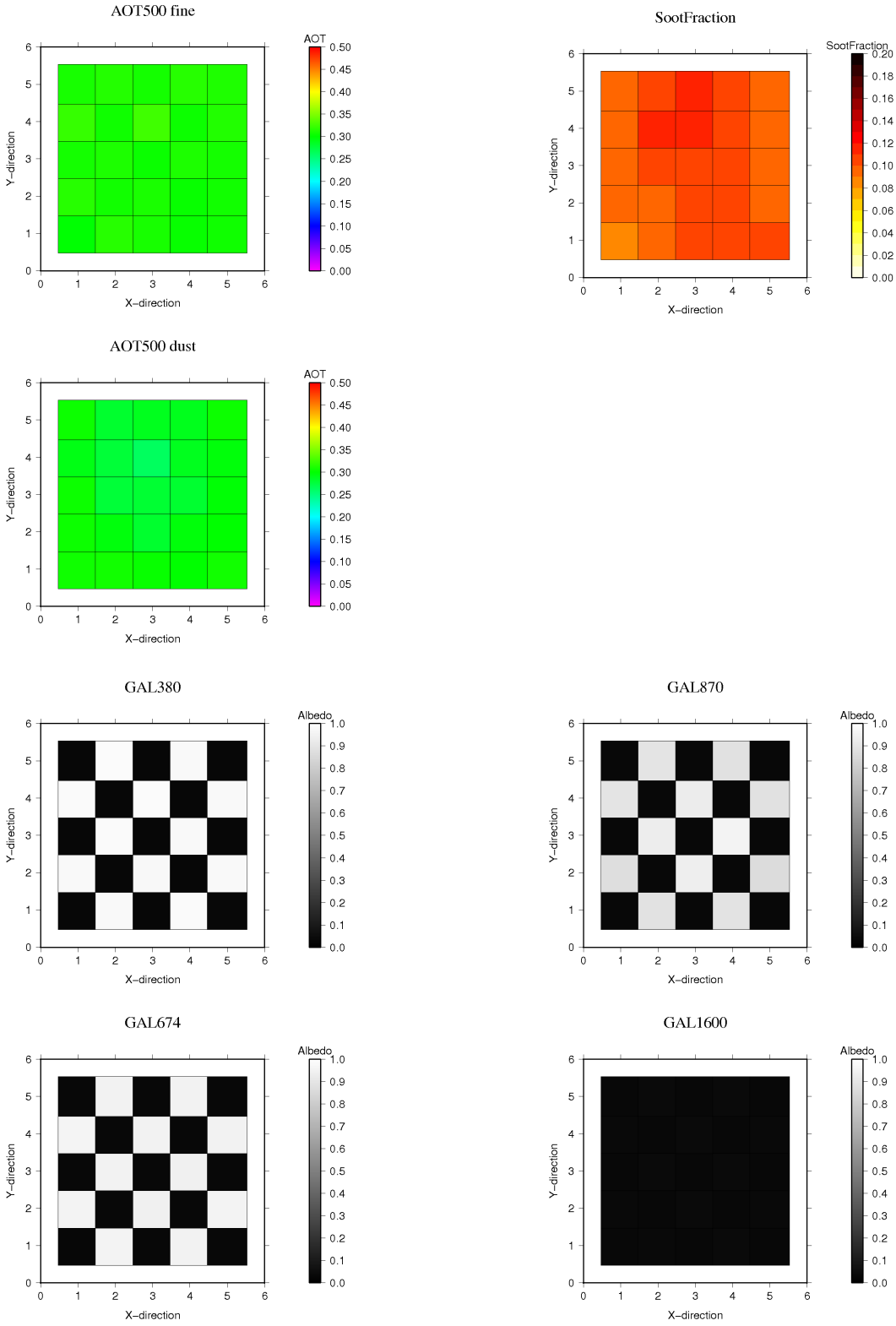

Figure 3.2.11b Same as in Fig. 3.2.11a but for retrieved state vector values.

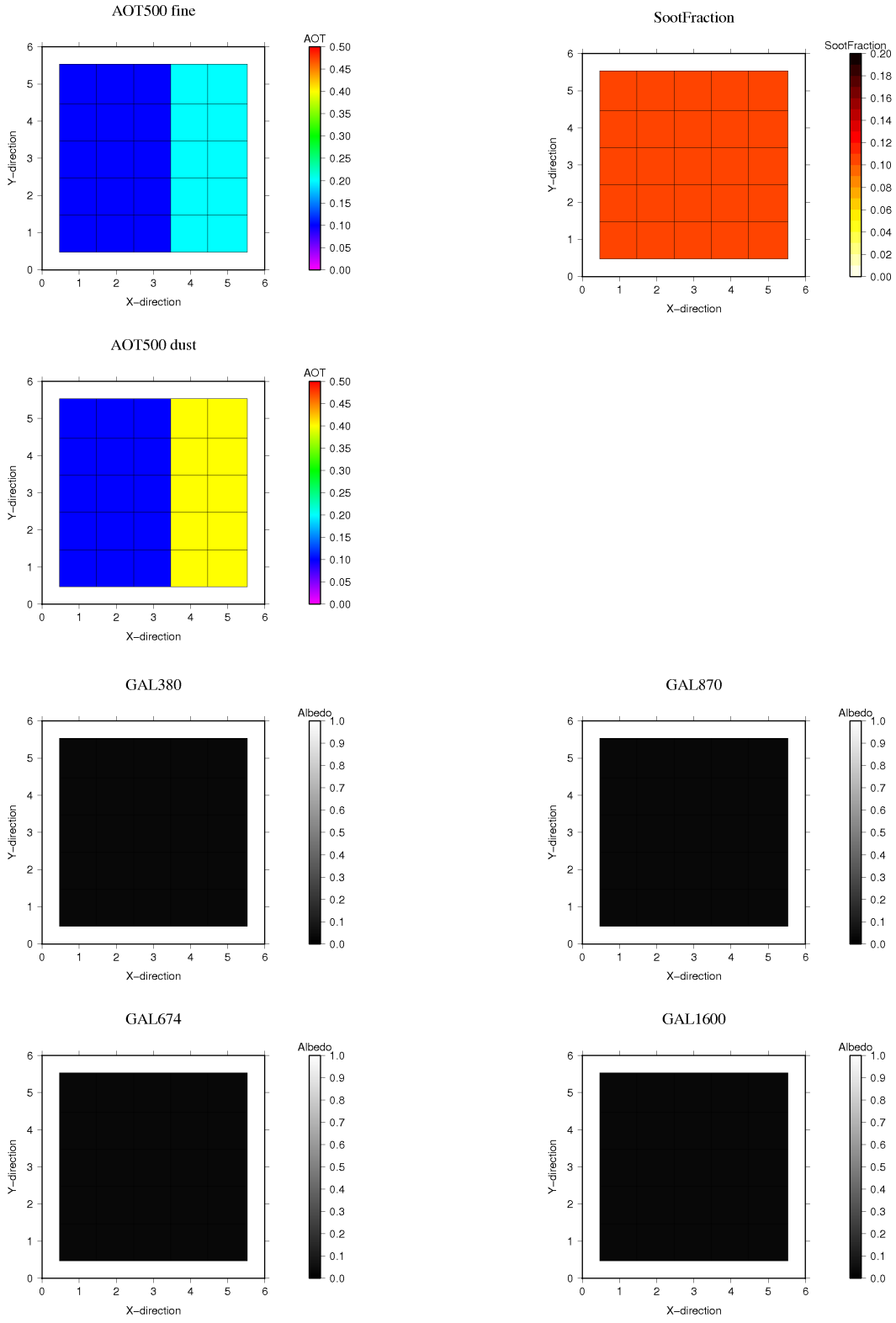

Figure 3.2.12a Same as in Fig. 3.2.12a but for a step-wise aerosol pattern over a homogeneous surface. True values are AOT(fine)=0.1 and 0.2 and AOT(coarse)=0.1 and 0.3, and SF=0.1; Sea water (dark) Ag at all four wavelengths (380, 674, 870, 1600nm).

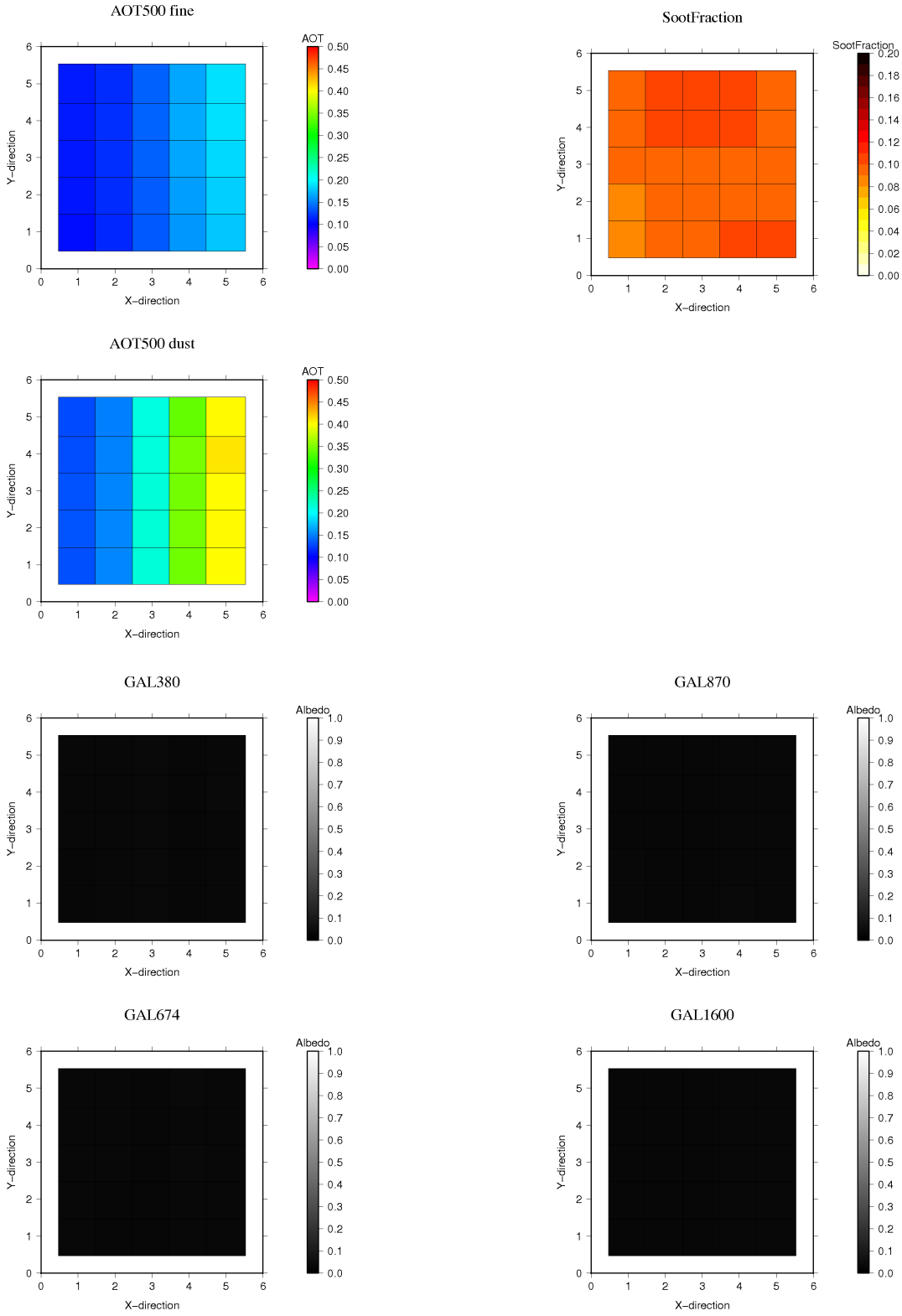

Figure 3.2.12b Same as in Fig. 3.2.12a but for the retrieved state vector values.

To investigate the effect of the boundary condition between sub-domains of the analysis, I conducted some experiments in cases of 10×10 pixels divided by four 5x5 pixel sub-domains. Figures 3.2.13 and 3.2.14 show the results of two surface types, i.e., a case of a lake surrounded by deciduous forest and another case of dry grass area in yellow sand surface. Calculation conditions are same as in Tables 3.2.1 and 3.2.2, but smoothing factors of aerosol parameters are set as $\gamma = 1.0$. In the former case, the true values of AOT(fine)=0.3, AOT(coarse)=0.1, SF=0.1, and deciduous and sea water of Aster spectral library are assumed for Ag of vegetation and lake area. In the latter case, the true values of AOT(fine)=0.1, AOT(coarse)=0.3, SF=0.1, and sand and dry grass of the Aster spectral library are assumed for Ag of yellow sand surface and grass area. For one experiment of the surface type, I calculated 50 patterns. Figures show that in both cases AOT(fine) and AOT(coarse) are retrieved within error of 0.05 at all pixels, and SFs are retrieved within 0.02. At the boundary pixels of each sub-domain, I find retrieved AOTs and SF are smoothly connected. From the results, I conclude that the distribution of state vectors, such as AOT and SF, can be retrieved by the present method being applied to a wide area composed of a number of sub-domains with different surface types.

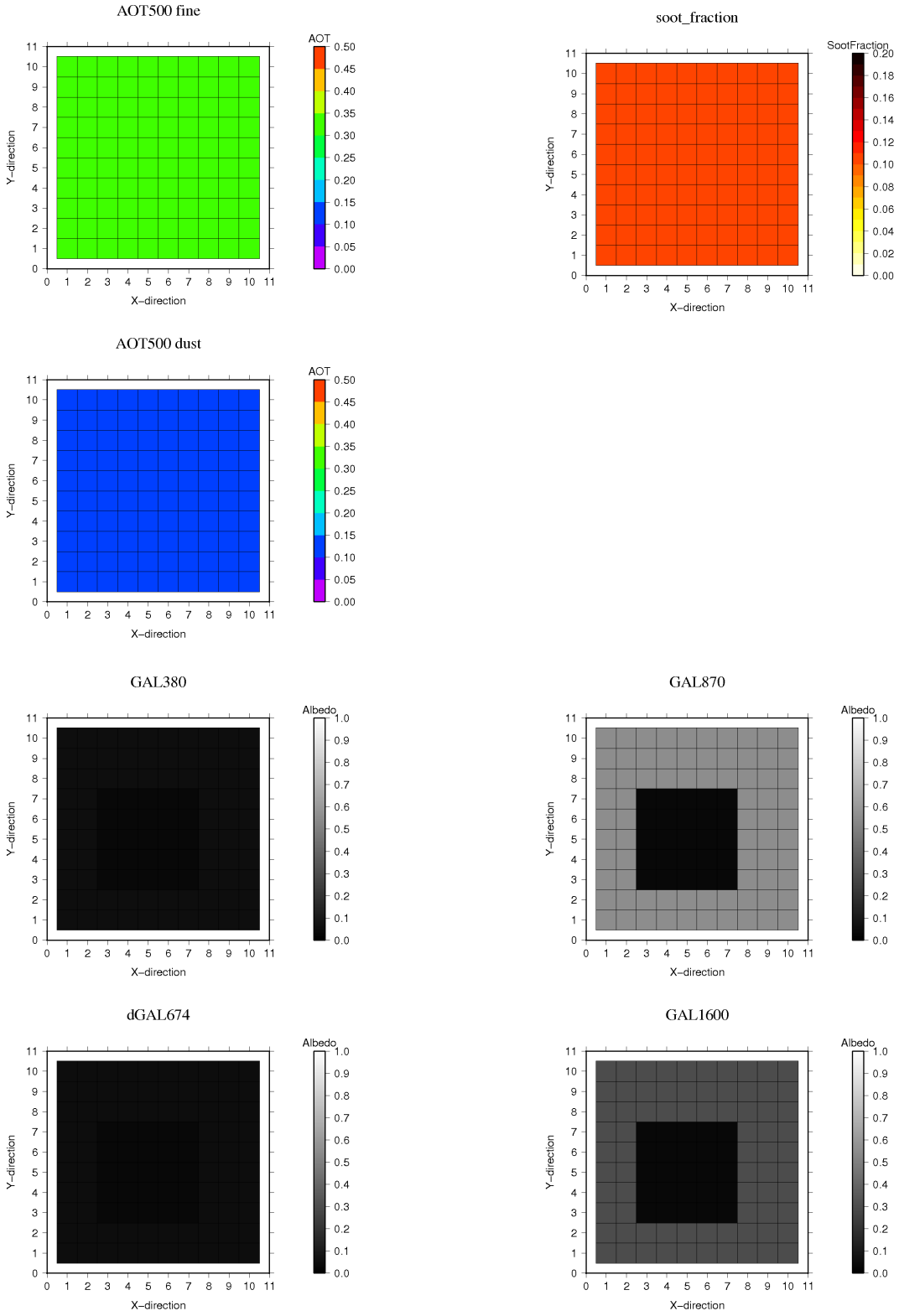

Figure 3.2.13a Same as in Fig. 3.2.11a but the true state vectors for the 10x10 pixels composed of a lake surrounded by deciduous forest. True values are assumed as AOT(fine)=0.3, AOT(coarse)=0.1, SF=0.1.

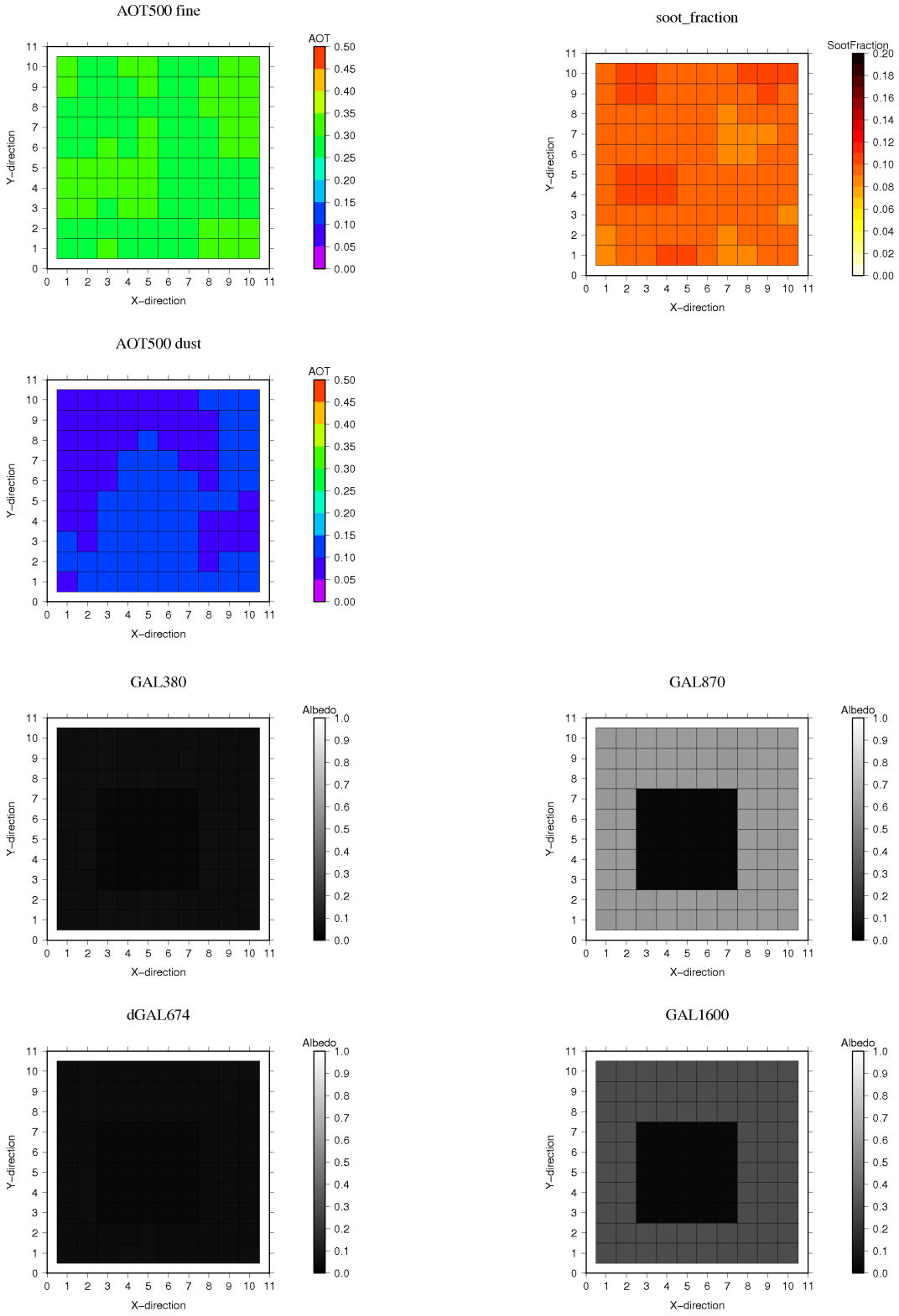

Figure 3.2.13b Same as Fig. 3.2.13a but for the retrieved state vector.

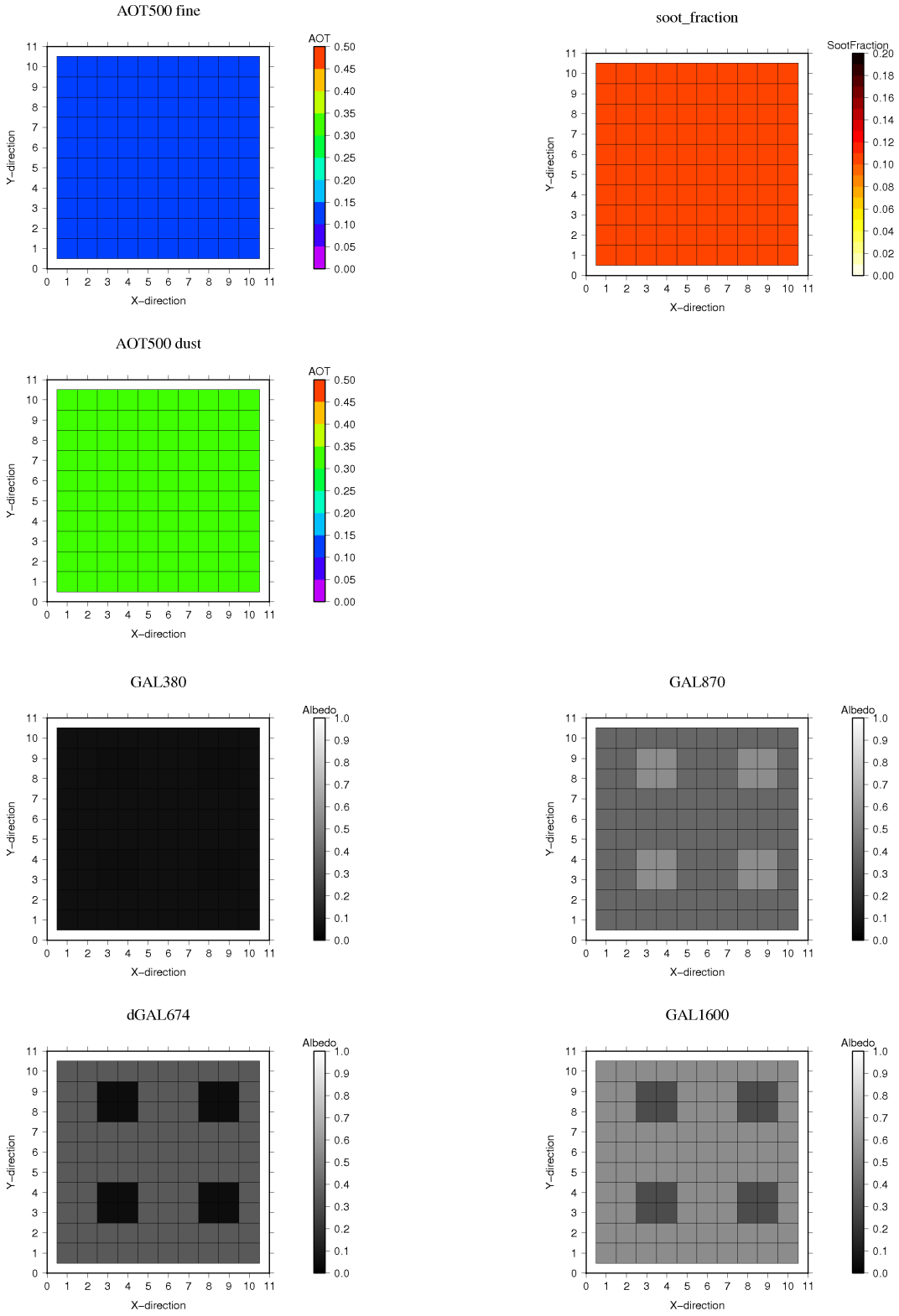

Figure 3.2.14a Same as in Fig.3.2.13a but for a surface composed of yellow brown and dry grass surfaces.

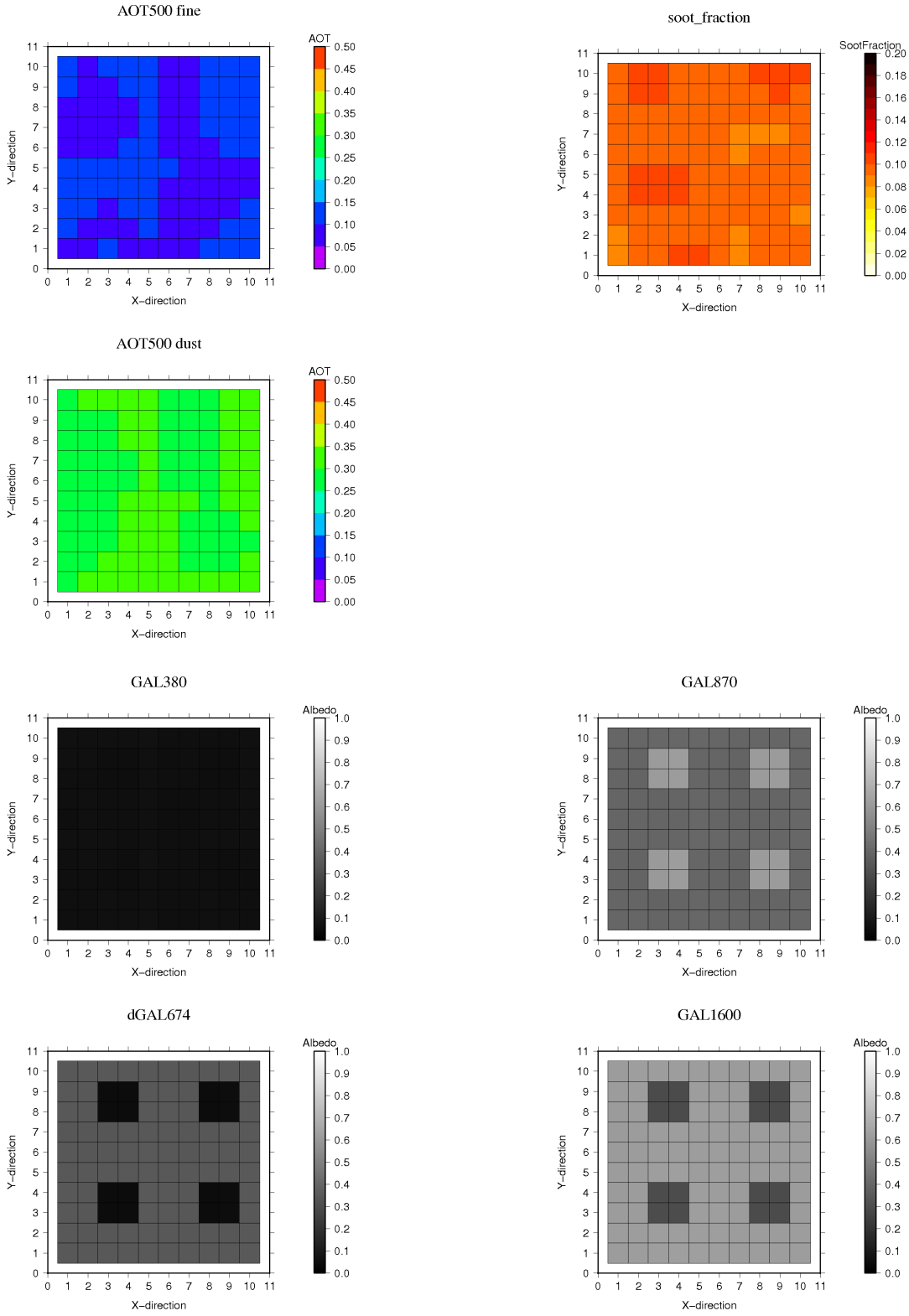

Figure 3.2.14b Same as in Fig. 3.2.14a but for retrieved state vector.

3.3 Summary

I have tested the new remote sensing method, developed in Section 2, by applying it to a set of surface patterns and aerosol distribution patterns and investigated the retrieval accuracy of state vectors and the effect of aerosol smoothing effect to retrieval results. It is found from the results that AOT(fine), AOT(coarse), soot fraction (SF) and surface albedo (Ag) can be retrieved within the error of 0.03, 0.05, 5%, 0.1 at γ =1.0, except for homogeneous snow or bright surfaces. The problem of aerosol remote sensing on the urban-like surface especially contains a large information contents of aerosol and land surface information to be retrieved.

In this algorithm, I assume that the aerosol property is almost spatially homogeneous in a sub-domain of a certain size, and I constrain the surface albedo of each pixel strongly using a priori information. It is found that the aerosol parameters and surface albedo are successfully retrieved when the multi-wavelength and multi-pixel information is used simultaneously in the sub-domain composed of several pixels with different wavelength dependence of aerosol properties and surface reflectance. The distributions of the state vectors are found to be smoothly connected between sub-domains in a wide area when a boundary condition of smooth connection at the boarder pixels is applied. It is important to recognize that the present method can retrieve SF if the sub-domain includes dark and bright surface pixels. Also it is found that a use of 380nm is advantageous for accurate SF retrieval.

Chapter 4 Real data analysis

4.1 Introduction

In this chapter, I apply the present algorithm to real satellite data from the GOSAT/TANSO-CAI imager. The main purpose of this study is to investigate the performance of the algorithm and validate it through comparison with ground-based observations. For this purpose I conduct case studies at several validation sites where ground-based validation instruments are located.

4.2 GOSAT / TANSO-CAI

The GOSAT (Greenhouse gases Observing SATellite) is the world's first satellite to monitor the concentration of greenhouse gases, i.e., carbon dioxide (CO_2) and methane (CH_4), from space. The GOSAT was developed by a collaboration of the Ministry of Environment (MOE), National Institute for Environmental Studies (NIES), and Japan Aerospace Exploration Agency (JAXA) and launched on January 23, 2009, from the Tanegashima Space Center. The GOSAT flies at 666km altitude polar orbit and completes one revolution in about 100 minutes, returning to the same point in space in three days (Table 4.2.1). The satellite has two sensors, TANSO-FTS (Thermal And Near-infrared Sensor for carbon Observation; Fourier Transform Spectrometer) and TANSO-CAI (Cloud and Aerosol Imager). TANSO-FTS is the main sensor of GOSAT and observes sunlight reflected by the ground surface and the (near infrared) spectral light emitted from the surface and the earth atmosphere (thermal infrared), utilized to derive CO_2 and CH_4. TANSO-CAI is a supplement sensor of TANSO-FTS, dedicated to measure cloud and aerosol properties.

Table 4.2.1 Observation orbit of GOSAT (http://www.gosat.nies.go.jp/index.html)

Orbiter	Sun-Synchronous Sub-Recurrent
Altitude	666 km
Inclination	98.05gedree
Mean local solar time on descending	1300±0:15
Launch date	12:54, January 23, 2009

Figure 4.2.1 Greenhouse gases Observing SATellite "IBUKI" (GOSAT) (provided by JAXA: http://global.jaxa.jp/projects/sat/gosat/index.html)

TANSO-CAI is an imaging sensor and observes reflected sunlight from the atmosphere and surface of the ground during the day. The sensor has four bands from near ultraviolet (near-UV) to shortwave infrared. Table 4.2.2 is a specification of TANSO-CAI. The field of view size is 0.5 km for band-1 through band-3, and 1.5km for band-4.

Table 4.2.2 Specifications of GOSAT/TANSO-CAI (http://www.gosat.nies.go.jp/index.html)

	Band-1	**Band-2**	**Band-3**	**Band-4**
Center wavelength [nm]	380	674	870	1600
Band width [nm]	20	20	20	90
Swath [km]	1000	1000	1000	750
Instant field of view [km]	0.5	0.5	0.5	1.5

One of the unique function of the CAI sensor is band-1 (380nm). The near-UV observation offers several advantages for the remote sensing of aerosols over land: (a) Low reflectance of most surfaces; (b) Weak BRDF effects, which simplifies the radiative transfer problem; (c) Sensitivity to absorbing aerosol types, which is enhanced by the large Rayleigh scattering; (d) Absorption of trace gases is weak in this spectral region (Höller, Higurashi and Nakajima, 2004). Figure 4.2.2 is an RGB composite image using GOSAT/TANSO-CAI band-1, band-2 and band-3 provided by JAXA/NIES/MOE. The yellow color plumes represent smoke aerosols emitted from biomass burning, and the white color features correspond to clouds. This figure shows that I can distinguish absorbing aerosol (smoke) from cloud by use of information at the wavelength of 380nm. Thus, it is possible to separately retrieve absorbing aerosol and non-absorbing aerosols using near-UV and other wavelengths.

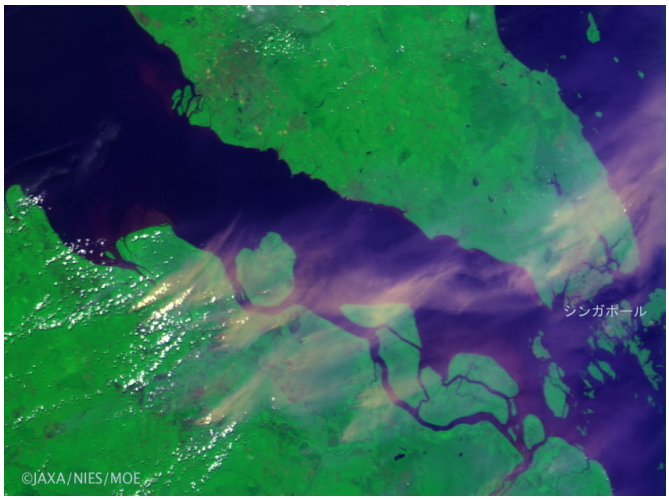

Figure 4.2.2 An RGB composite image. Smoke from forest fires (Smoke is distinguished from clouds by 380nm) (Original data provided by JAXA/NIES/MOE)

4.3 Data set

4.3.1 Vicarious calibration

The raw radiance L_0 in a digital number (DN) unit is converted in JAXA to the level-1 data, L_1, by geometrical calibration and pre-flight radiometric calibration. I applied the vicarious radiometric calibration constants (Shiomi et al., 2010) in Table 4.3.1 to level-1 data, producing level-1b radiance data, L_{1b}, in radiant energy unit (W/m^2/μm/str) by a transformation,

$$L_{1b} = a \cdot L_1 + b, \tag{4.3.1}$$

where a and b are vicarious radiometric calibration constants regularly obtained by vicarious calibrations with ground-based radiometers in the condition that satellite flies over the ground sites (Yoshida et al., 2005).

Table 4.3.1 Vicarious calibration constants of GOSAT/TANSO-CAI radiances. These coefficients are obtained in a period from April to July 2009. (Shiomi et al., 2010). The unit of b is [W/m^2/μm/str]

Band	1	2	3	4
a	1.138	0.946	1.033	1.144
b	0.00	-1.372	-0.189	0.00

4.3.2 Earth-sun distance correction

In the inversion process, I use apparent reflectance, R, calculated from observed radiance, L_{1b}, and the solar irradiance at TOA, F,

$$R = \frac{\pi L_{1b}}{\mu_0 F}, \tag{4.3.2}$$

$$F = \frac{F_0}{d^2}, \tag{4.3.3}$$

where d is the Earth-sun distance in Astronomical Unit (AU). μ_0 is the cosine of solar zenith angle. F_0 is the extraterrestrial solar irradiance when the Earth-sun distance is 1 AU. I use Thuillier (2002) for F_0 (Table 4.3.2).

Table 4.3.2 Extraterrestrial solar irradiance for CAI bands. Thuillier (2002)

Band	1	2	3	4
F_0[W/m^2/μm/str]	1093.76	1497.66	952.575	252.311

4.3.3 A priori data set

4.3.3.1 Ground surface albedo

I use the minimum reflectance as a priori ground surface albedo with the correction by Fukuda et al. (2013). The minimum reflectance ($R_{\min,31}$) is the lowest value of the daily apparent radiance of CAI in a period before and after 31days of target day, assuming $R_{\min,31}$ is under non-aerosol condition. Then, Rayleigh scattering correction is applied to $R_{\min,31}$, and estimate ground surface albedo (A_g) under isotropic scattering approximation. However, the observation times are less than 11 times for 31 days, because GOSAT returns to the same point in space every three days (i.e. the 3rd recurrence), so that the minimum reflectance includes significant aerosol effects. Fukuda et al. (2013) proposed a correction method, called modified Kaufman method (Fukuda et al., 2013), to estimate A_g at wavelength 380nm by a formula,

$$A_g(380\text{nm}) = a_{NDVI} \cdot A'_g(674\text{nm}), \tag{4.3.4}$$

$$a_{NDVI} = -0.192309 \cdot \exp(-9.62693 \cdot NDVI) + 0.3, \tag{4.3.5}$$

$$NDVI = \frac{A'_g(870\text{nm}) - A'_g(674\text{nm})}{A'_g(870\text{nm}) + A'_g(674\text{nm})}, \quad (4.3.6)$$

where A'_g is a ground surface albedo derived from the minimum reflectance and Rayleigh correction. NDVI is Normalized Difference Vegetation Index.

4.3.3.2 A priori information of AOT(fine) and AOT(coarse)

For a priori information of AOT, I used the monthly mean values of fine and coarse mode AOT (AOT(fine) and AOT(coarse)) at wavelength of 500nm derived by ground-based aerosol monitoring networks, AERONET and SKYNET (See Figures 4.3.1 and 4.3.2).

Observation sites of AERONET (Aerosol Robotic Network in NASA: Holben et al., 1998; Dubovik and King, 2000) are widely distributed on the globe, and AOT, Ångstrom exponent, SSA, particle size distribution and complex refractive index are obtained from the observed sky radiance. Its data is used to validate satellite data in many past studies. SKYNET (Sky Radiometer Network: Nakajima et al., 1996) is a similar network to AERONET, and observation site is spread in Asia, India and Europe, where are an important place to monitor anthropogenic aerosols.

AERONET version 2 provides AOT(fine) and AOT(coarse) at wavelength 500nm, so I utilized monthly mean values of AOT(fine) and AOT(coarse) as a priori information. I also used SKYNET Level 2.0 AOT (Nakajima et al., 1996; Khatri and Takamura, 2009; Hashimoto et al., 2012). However, they only provide total AOT, so I divided total AOT at wavelength 500nm to AOT(fine) and AOT(coarse) as using Ångstrom exponent, α, by a simplified relation as follows,

$$AOT_{\text{fine}} = 0.5 \cdot \alpha \cdot AOT_{\text{total}}, \quad (4.3.7)$$

$$AOT_{\text{coarse}} = (1 - 0.5 \cdot \alpha) \cdot AOT_{\text{total}}, \quad (4.3.8)$$

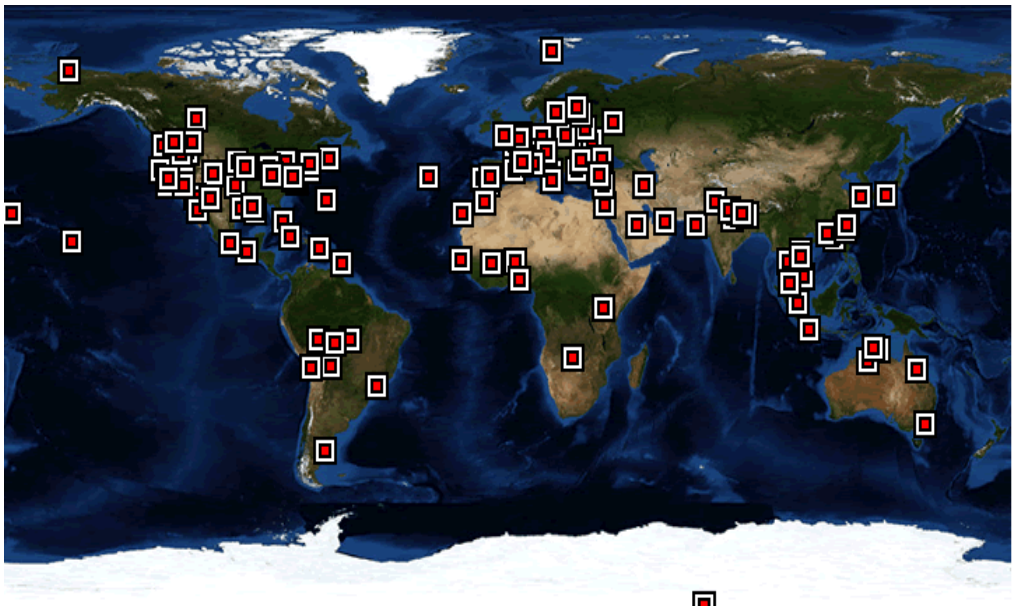

Figure 4.3.1 Observation sites of AERONET (Aerosol Robotic Network in NASA) Level 2.0 (http://aeronet.gsfc.nasa.gov/)

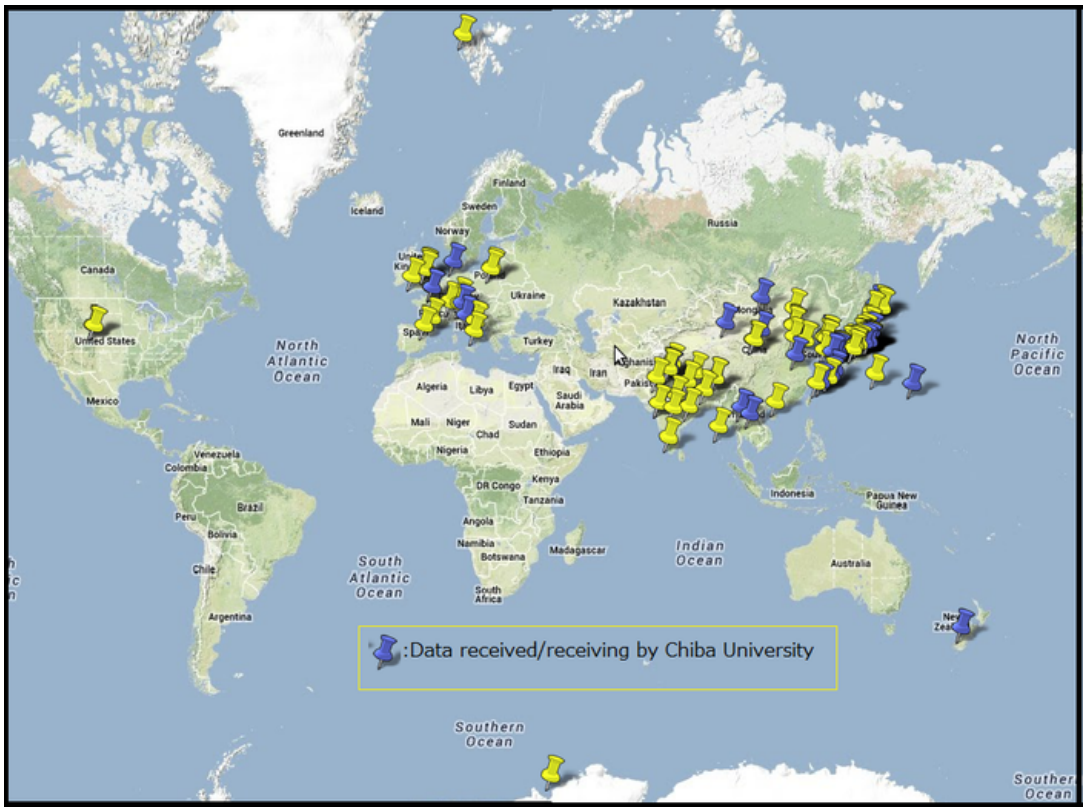

Figure 4.3.2 Observation sites of SKYNET (http://atmos.cr.chiba-u.ac.jp/)

4.4 Experimental setting and procedure of analysis

I defined a 5×5 pixel region as a sub-domain. In this analysis, the resolution is 0.0125×0.0125 degrees, and here, about 2×2 km for a pixel as shown Figure 4.4.1.

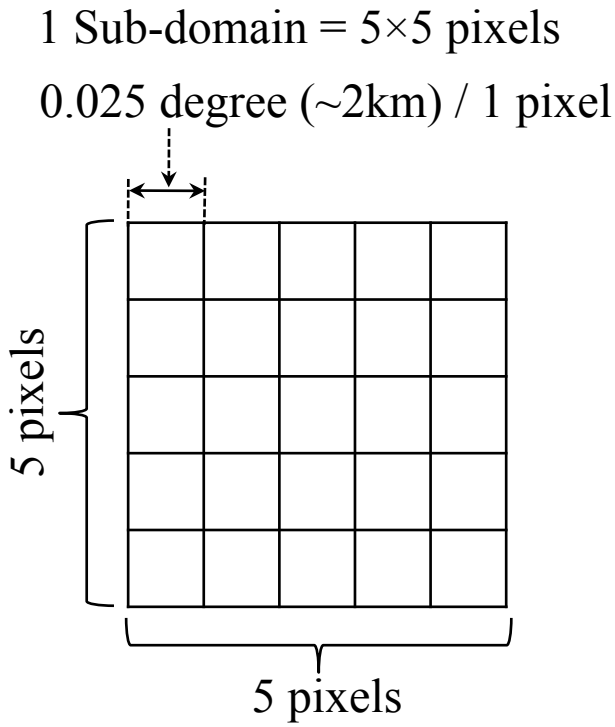

Figure 4.4.1 Definition of a sub-domain for analysis by the present algorithm.

The measurements (**R**) are composed of GOSAT/CAI band-1 through band-4 data and all pixels in the sub-domain. The state vector (**u**) consist of AOT(fine) and AOT(coarse) at wavelength of 500nm, volume soot fraction in fine particles (SF) and ground surface albedo of each wavelength.

The nearest pixel's AOT(fine) and AOT(coarse) of AEONET or SKYNET site are given as a priori information of each pixel, and a priori SF is fixed at a value of 0.03, because I do not have a reliable data set for SF on global scale.

$$\mathbf{R}^{\mathrm{meas}} = \begin{pmatrix} \boldsymbol{R}_{iw=1,\lambda=0.380\,\mu\mathrm{m}} \\ \boldsymbol{R}_{iw=2,\lambda=0.674\,\mu\mathrm{m}} \\ \boldsymbol{R}_{iw=3,\lambda=0.870\,\mu\mathrm{m}} \\ \boldsymbol{R}_{iw=4,\lambda=1.600\,\mu\mathrm{m}} \end{pmatrix} \quad \mathbf{u}_{\mathrm{ret}} = \begin{pmatrix} \boldsymbol{u}_{ip=1,\mathrm{AOTfine}} \\ \boldsymbol{u}_{ip=2,\mathrm{AOTcoarse}} \\ \boldsymbol{u}_{ip=3,\mathrm{SF}} \\ \boldsymbol{u}_{ip=5\sim7,Ag_{iw}} \end{pmatrix} \quad \mathbf{u}_{a} = \begin{pmatrix} \boldsymbol{u}_{a,ip=1,\mathrm{AOTfine}} \\ \boldsymbol{u}_{a,ip=2,\mathrm{AOTcoarse}} \\ \boldsymbol{u}_{a,ip=3,\mathrm{SF}} \\ \boldsymbol{u}_{a,ip=5\sim7,Ag_{iw}} \end{pmatrix}, \tag{4.4.1}$$

I show other input parameters and geometries in Table 4.4.1.

Table 4.4.1 Input parameters of geometries and atmospheric consitions

	Parameters	Unit	Data from
Geometry	Solar zenith angle (θ_0)	Degree	GOSAT/TANSO-CAI
	Satellite zenith angle (θ_1)	Degree	GOSAT/TANSO-CAI
	Relative azimuth angle (φ)	Degree	GOSAT/TANSO-CAI
Atmosphere	Surface pressure	hPa	NCEP reanalysis
	Surface relative humidity	Ratio	NCEP reanalysis
	Ozone	DU	OMI Level 3

Initial values of retrieval parameters are as follows: AOT(fine)=0.01, AOT(coarse)=0.01; SF=0.01; Ag = 0.01 at all four wavelength. Values of measurement error covariance, a priori covariance and smoothing parameters are shown in Table 4.4.2 and 4.4.3. I assume that the radiance measurement error is within 2%. It is expected to retrieve CO_2 from GOSAT within an accuracy of 1%, and it is comparable to about 0.03 in AOT at wavelength 1.6μm (Ota et al., 2006 Tenki) and is also comparable to about 2 to 3% error in radiance estimated by use of a single scattering and two-stream approximations. Aerosols vary temporally and spatially and it is difficult to determine a priori covariance, so that I set fixed values for a priori covariance S_a as given in Table 4.4.3. And also, I fix the smoothness factor to AOTs and SF at γ=1.0 based on the assumption that aerosol is distributed smoothly in horizontal directions.

Table 4.4.2 Measurement error covariance set in analysis for each band

	Band1	Band2	Band3	Band4
Range for Measurement error covariance, S_e	2%	2%	2%	2%

Table 4.4.3 A priori covariance and smoothing factor set in analysis for each parameters

Retrieval parameters	AOT(fine)	AOT(coarse)	SF	Ag
Range for A priori covariance, S_a	$\Delta u = \pm 0.5$	$\Delta u = \pm 0.5$	100%	$\Delta u = \pm 0.1$
Smoothing factor, γ	1.0	1.0	1.0	0.0

In the analysis I utilized aerosol models in Table 4.4.4, which are built in RSTAR. For the each mode, aerosol models are internally mixed by volume ratio, and fine and coarse modes are mixed externally using both AOT values.

Table 4.4.4 Aerosol models of fine and coarse modes set in analysis. r_m is aerosol mode radius; S is dispersion of the aerosol volume size distribution (See Eq. (2.3.2)); k_λ is imaginary part of refractive index at wavelength λ.

	Component	r_m [μm]	S	k_{380}	k_{674}	k_{870}	k_{1600}
Fine mode	Water soluble	0.175	2.24	0.005	0.007	0.013	0.023
	Dust-like			0.008	0.008	0.008	0.008
	Soot			0.463	0.430	0.431	0.468
Coarse mode	Yellow brown	3.00	4.00	0.007	0.004	0.003	0.002
	Soot			0.463	0.430	0.431	0.468

RSTAR is implemented the WCP hygroscopic growth model of aerosol particles (WCP, 1983), and I applied it to fine mode aerosols,

WCP (World Climate Programme) 1983: Report of the experts meeting on aerosols and their climatic effects, Williamsburg, Virginia, 28-30 March 1983 (Edited by Deepak, A. and H. E. Gerber) WMO-ICSU WCP-55

$$r(a_w) = r_0 \left[1 + \rho \frac{m_w(a_w)}{m_0} \right]^{1/3}, \quad a_w = f(RH), \tag{4.4.2}$$

$$n = n_w + (n_0 - n_w) \cdot \left[\frac{r_0}{r(a_w)} \right]^3, \tag{4.4.3}$$

where $r(a_w)$ and r_0 are a particle radius related to relative humidity and dry particle radius; ρ is the particle density relative to that of water. m_w and m_0 are the ass of condensed water and dry particle, respectively; a_w is the water activity which is essentially the relative humidity RH; n is the effective complex refractive index, and n_0 and n_w is the volume weighted average of the refractive index of

the dry aerosol substance and water, respectively.

I show the analysis procedure in Fig. 4.4.2. I input all the parameter required to the inversion analysis by this new algorithm. Then, I obtain aerosol parameters, such as AOT(fine), AOT(coarse), SF, and Ag of each wavelength, in target areas.

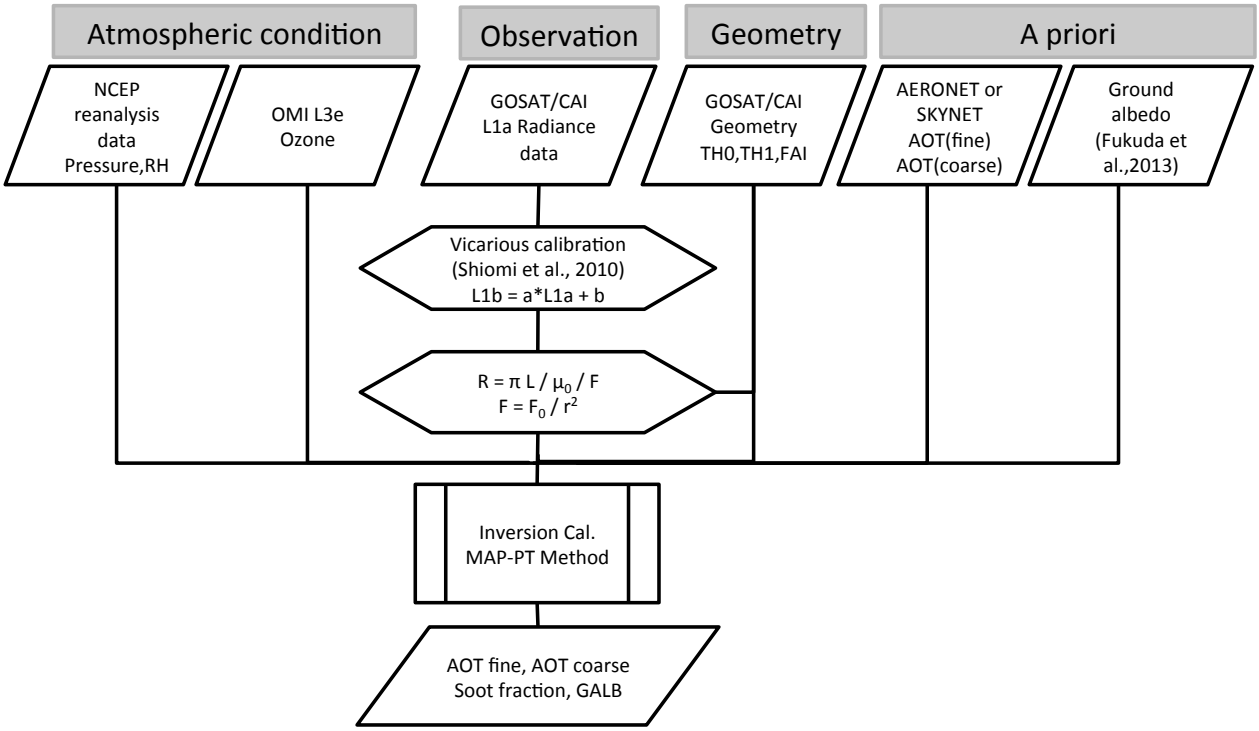

Figure 4.4.2 Flow chart of analysis procedure. MAP-PT method denotes the present method.

4.5 Analysis Results and Discussion

4.5.1 Validation and Comparison the result with ground-based observations

4.5.1.1 Validation area

To validate the result retrieved by this algorithm, I first selected target areas in the condition that three ground-based observation sites exist and the urban area is included in 100×100 km area, because I need to study the retrieval results by the new algorithm in the urban area or spatially heterogeneous surface area. I show the selected area, Area1 and Area2, in Figure 4.5.1. Area1 is the East coast of the United States (76-77°W/38.7-39.4°N) including areas of urban, agricultural fields, vegetation and water surface, composed of 64 sub-domains. Area2 is around Paris in France

(2.15-2.50°E/48.68-48.88°N) including areas of urban, agricultural fields and vegetation, composed of 9 sub-domains. Locations of ground-based observation sites of AERONET are listed in Table 4.5.1. The analysis period is from July 2009 to December 2009.

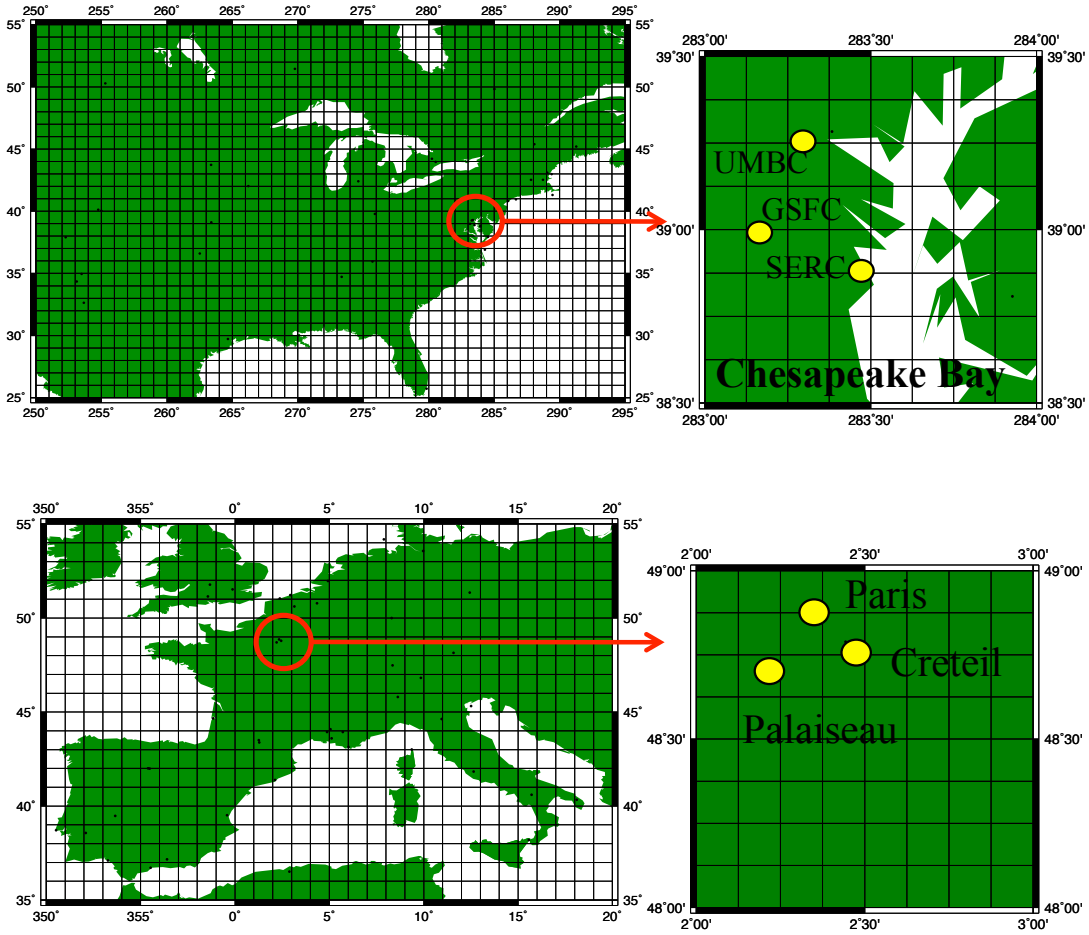

Figure 4.5.1 Analysis area information. Area1 is the East coast of the United States (76-77°W/38.7-39.4°N) and Area2 is around Paris in France (2.15-2.50°E/48.68-48.88°N)

Table 4.5.1 Location of ground-based observation sites (AERONET) for validation

Site name	Longitude	Latitude	Data from
UMBC	76.7094°W	39.2546°N	AERONET
GSFC	76.8398°W	38.9925°N	AERONET
SERC	76.5000°W	38.8833°N	AERONET
Cretail	2.4428°E	48.7885°N	AERONET
Palaiseau	2.2083°E	48.7000°N	AERONET
Paris	2.3333°E	48.8667°N	AERONET

4.5.1.2 Validation Result

I retrieved AOT(fine) and AOT(coarse) at wavelength of 500nm, SF and Ag of each pixel in the target region. I show a calibration result using Shiomi et al. (2010) and albedo correction Fukuda et al. (2013) in Figure 4.5.2. I compared AOT(fine) and AOT(coarse) derived by this method with the values of AERONET at the nearest site. In the case before vicarious calibration and albedo correction, AOTs(fine) are underestimated, and AOTs(coarse) are greatly overestimated. The underestimation of AOT(fine) is improved by introduction of the vicarious calibration constants (Shiomi et al., 2010), and the overestimation of AOT(coarse) is also reduced by the albedo correction. I show a time series of a priori surface reflectance that I used, i.e., the minimum reflectance in 30 days around the target day at the close pixel to SERC site, as in Figure 4.5.3. The upper panel in the figure shows the minimum reflectance before albedo correction, and the lower panel shows the minimum reflectance corrected by Rayleigh correction and Fukuda et al. (2013). The largest difference is the value at wavelength of 380nm (i.e. band 1), and a main cause of the difference is the effect of Rayleigh scattering. In the analysis, a dust particle model (yellow sand) is used for coarse particles, and has an absorption in near UV (380nm) or blue part of visible region. The possible reason why AOTs(coarse) are overestimated is that the greatly overestimated reflectance at the wavelength of 380nm is offset by increasing AOT(coarse). I need to set accurate a priori of surface reflectance for accurate aerosol retrieval.

From the result of the vicarious calibration, AOT(fine) and AOT(coarse) at wavelength of 500nm became close to the AERONET values.

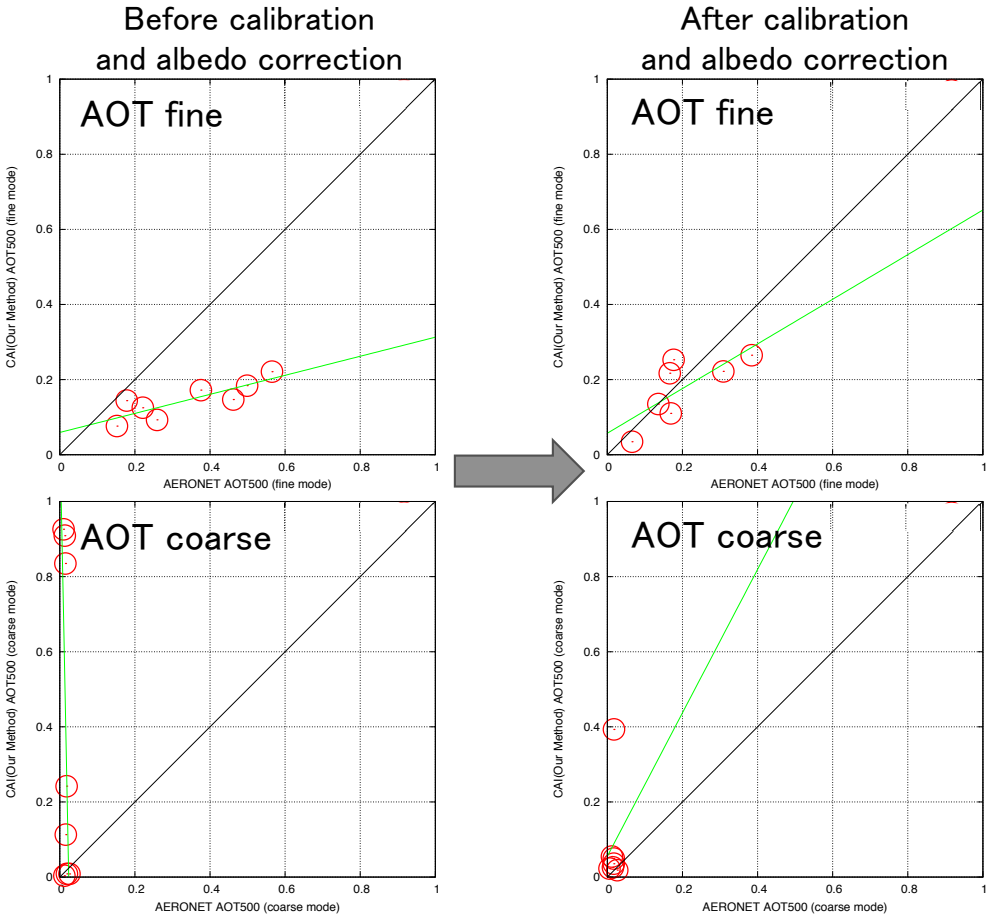

Figure 4.5.2 Comparison of AOT(fine) and AOT(coarse) at wavelength of 500nm between AETONET and the closest pixel of CAI with this method at SERC site. Left and right panels are the result before and after calibration and albedo correction. Top and bottom panels show AOT(fine) and AOT(coarse), respectively. Analysis periods are from June 2009 to September 2009 (left panel), and July 2009 to December 2009 (right panel)

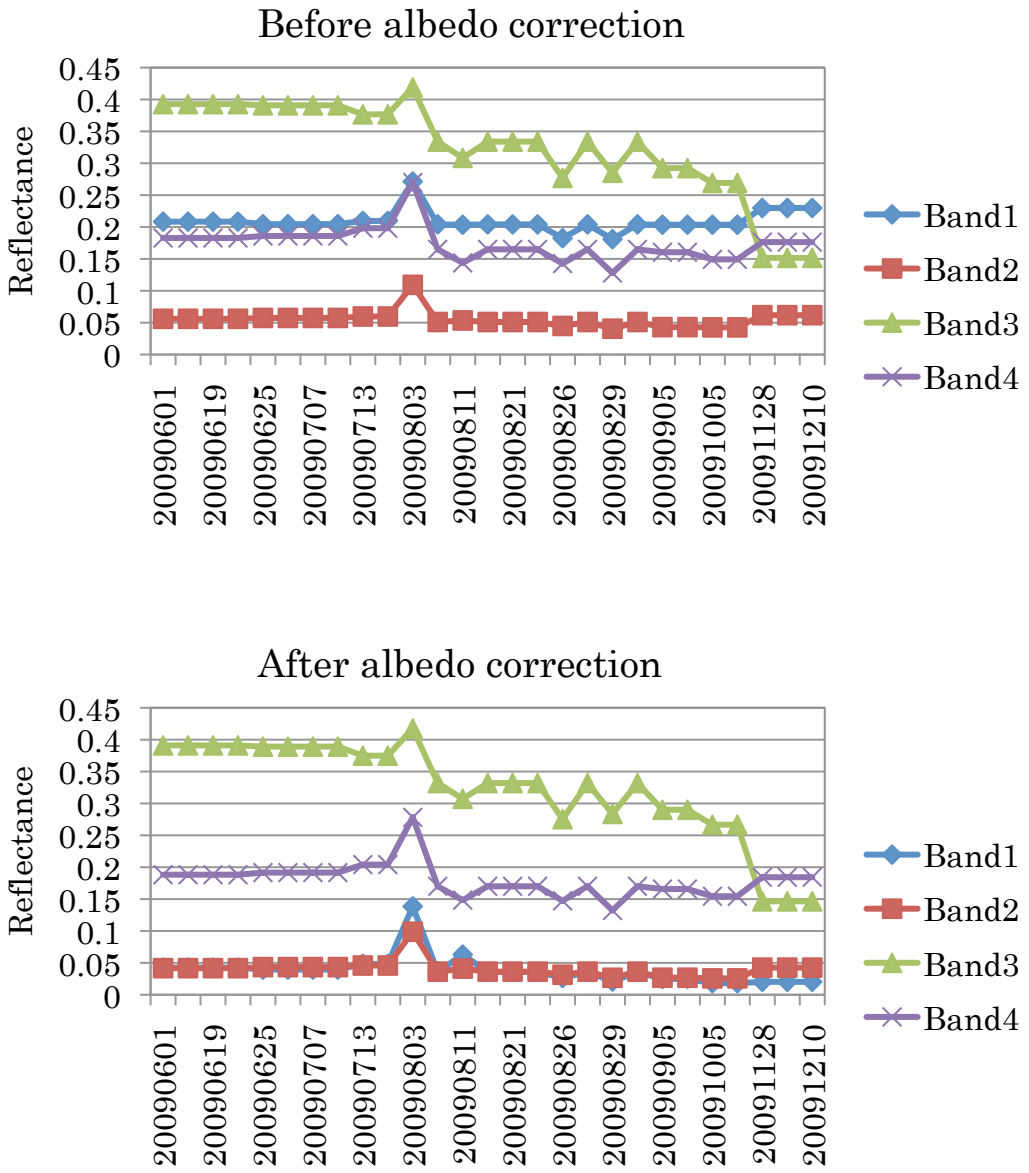

Figure 4.5.3 Time series of the minimum reflectance of each band used in the analysis. Top panel shows the value not corrected by Rayleigh correction and by the aerosol correction of Fukuda et al., (2013); Bottom panel shows the corrected values.

To validate the result of AOT derived by this method, I first select data to compare my results with AERONET retrieval values by following condition:

1. Root mean square error (ε) < 0.1; to remove low accuracy data;
2. The difference of Julian time between TANSO-CAT and AERONET < 0.05 (=1.2 hours); to take into account aerosol temporal variability, and to judge clear sky if AERONET retrieval data exist;
3. Remove cloud and low accuracy data judged by CLOUDIA (Ishida et al., 2009) and the cloud screening method of Fukuda (2010, PhD thesis at the University of Tokyo).

Figures 4.5.4 and 4.5.5 compare the results of AOT(fine), AOT(coarse) and AOT(total), which is sum of AOT(fine) and AOT(coarse), between TANSO-CAI with this method at the closest pixel of AETONET site and AERONET. Cross marks in the figures denote a priori values I used in the analysis. We can see that the results of AOT(fine) and AOT(coarse) do not completely depend on a priori values from the results.

From the result, AOT(fine) and AOT(coarse) close to the AERONET values are obtained. Those two regions include urban area, and comparison sites are in urban area. Furthermore, in both cases, the results have captured the features of the aerosols in urban area where fine particles (anthropogenic) are large and coarse particles are small (Kaufman et al., 2002; Dubovik et al., 2002). In the result of Area 1, one AOT(coarse) at GSFC and SERC on October 5, 2009 is greately overestimated, while the same day's data at UMBC was screened by screening condition 3. Therefore, there is a possibility of cloud contamination. I checked the result and observation image of band-2 (674nm), at which reflectance from cloud is strong, of Area 1 on October 5, 2009, and found whitish part that was distributed in a patchy feature at both sides of Chesapeake Bay and on the observation sites, as shown in Figure 4.5.6. Therefore, the overestimation of AOTs(coarse) at GSFC and SERC are probably caused by cloud contamination.

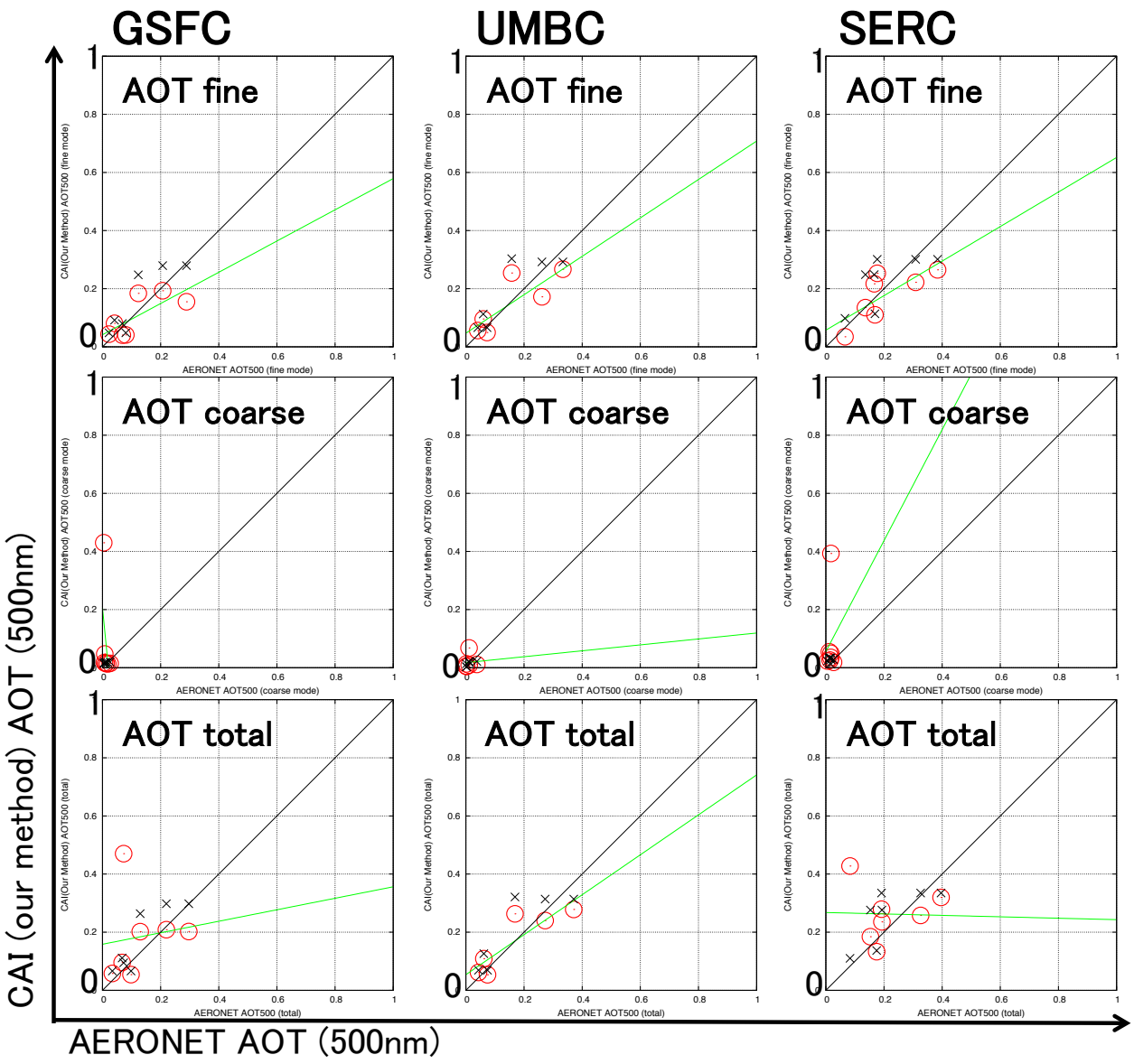

Figure 4.5.4 Comparison of AOT(fine), AOT(coarse) and AOT(total) at wavelength of 500nm between AETONET and the closest pixel of CAI with this method in Area 1. Red circle is a comparison of AOT, cross denotes a priori of AOT. Left, center and right column panels are the results at GSFC, UMBC and SERC, respectively. Top, middle, and bottom panels show AOT(fine), AOT(coarse), and AOT(total), respectively. Analysis period is July 2009 to December 2009.

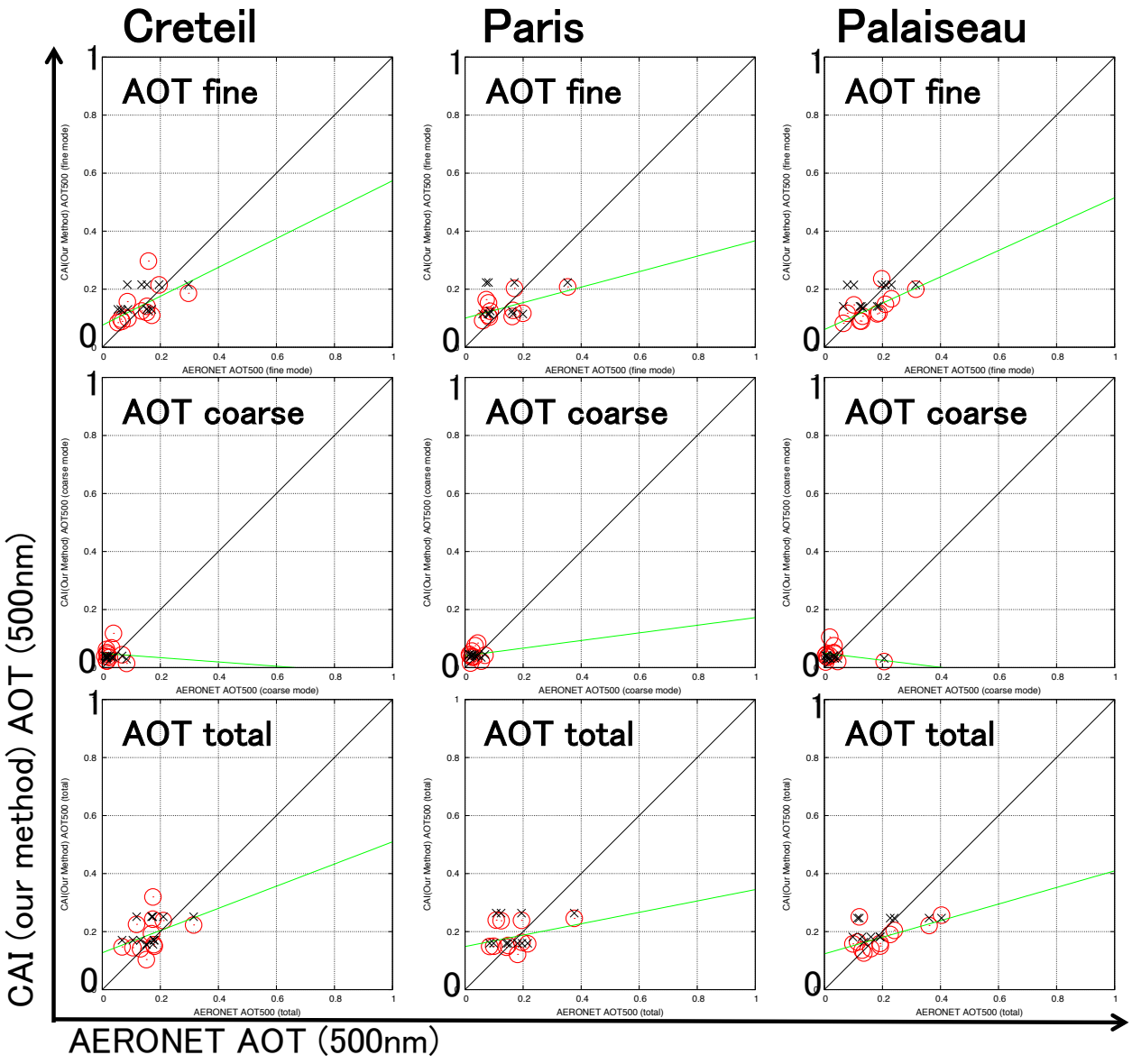

Figure 4.5.5 Same as in Fig. 4.5.4 but for Area 2. Red circle is a comparison of AOT, cross mark denotes a priori of AOT. Left, center and right column panels are the result at Cretail, Paris and Palaiseau, respectively.

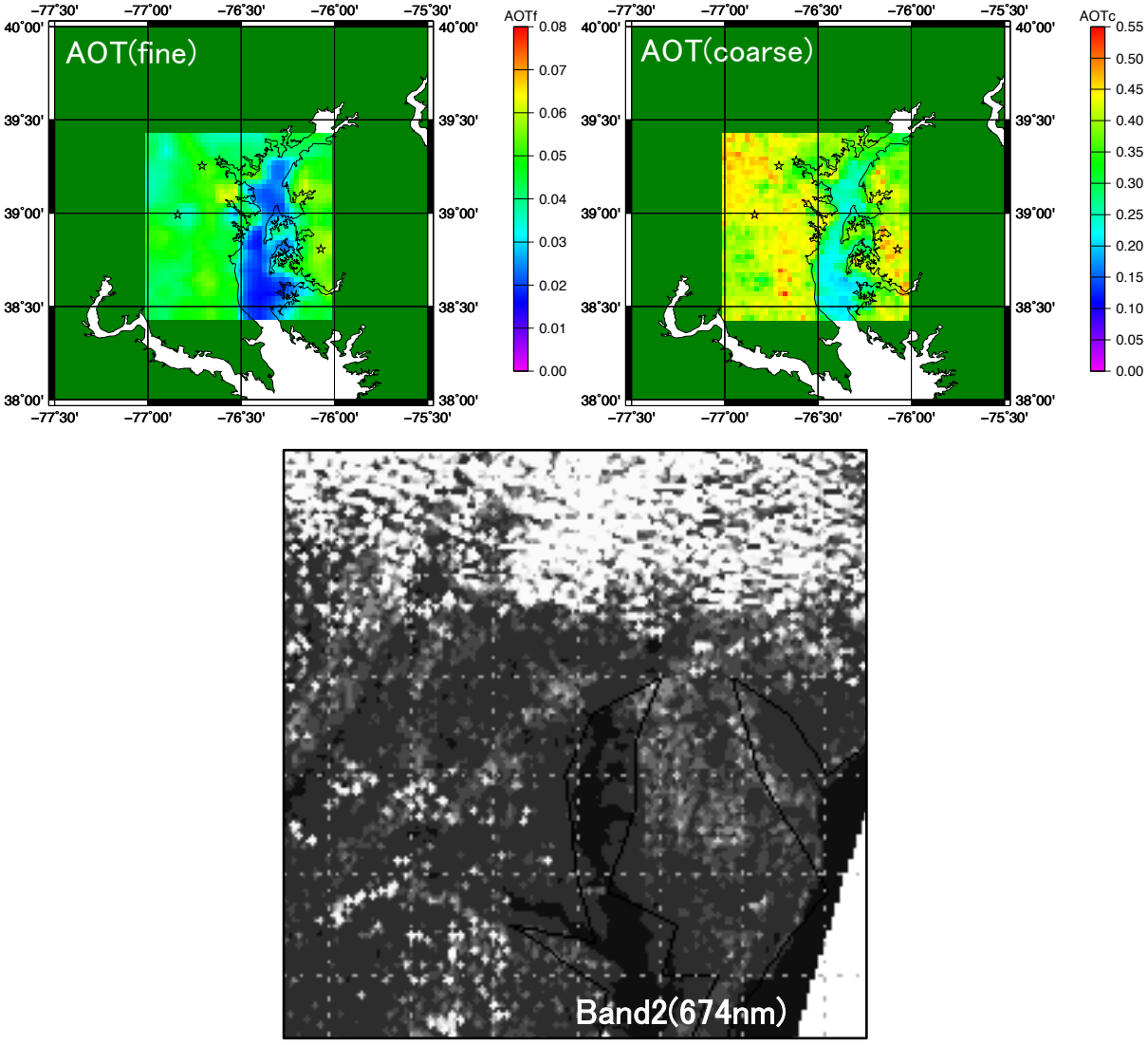

Figure 4.5.6　Retrieval result of AOT(fine) and AOT(coarse) in Area 1 on October 5, 2009 (Top panel), and TANSO-CAI imager data at wavelength of 674nm (band-2).

I calculate AOT difference between AERONET and the closest TANSO-CAI pixel with this method, and this value denotes one of index of retrieval accuracy in satellite remote sensing. The AOT difference, $\Delta\tau$, was calculated by

$$\Delta\tau = \sqrt{\frac{1}{N}\sum_{N}(\tau_{\text{retrieval},\,i} - \tau_{\text{ground-based},\,i})^2}\,, \tag{4.5.1}$$

where N is the number of data; $\tau_{\text{retrieval}}$ and $\tau_{\text{gound-based}}$ are retrieval value by the method and AERONET AOT, respectively. The results at sites of Table 4.5.1 are shown in Table 4.5.2. Note that I eliminated cloud like case on October 5, 2009 when I calculated the difference.

Table 4.5.2 AOT difference from AOT of AETONET or SKYNET of each site (ΔAOT or $\Delta\tau$). See Equation (4.5.1). ΔTime is observation time difference between TANSO-CAI and AERONET.

	ΔAOT(total)	ΔAOT(fine)	ΔAOT(coarse)	ΔTime
GSFC	±0.054	±0.065	±0.018	< 1.2h
SERC	±0.062	±0.075	±0.025	< 1.2h
UMBC	±0.060	±0.063	±0.026	< 1.2h
Cretail	±0.070	±0.061	±0.040	< 1.2h
Paris	±0.076	±0.068	±0.027	< 1.2h
Palaiseau	±0.076	±0.057	±0.064	< 1.2h

Mean values of AOT(total), AOT(fine) and AOT(coarse) at the six sites are ±0.066, ±0.065 and ±0.033, respectively. Those values are likely good results compared with present AOT retrieval accuracy in land area by satellite remote sensing, ±0.05±0.2AOT or 5~30% (Kaufman et al., 2002; Chu et al., 2003; Lee et al., 2009). For urban area, this reported AOT error, ±0.05±0.2AOT, is the result of error over vegetated and semi-vegetated region in of near urban area (Chu et al., 2003). However, I compared AOT between AERONET and the closest TANSO-CAI pixel. Therefore, it is likely that AOT(fine) and AOT(coarse) can be retrieved over complex surface reflectance region like the urban area by this method.

4.5.2 Result of Clear days

In this section, I show results of analysis in Area 1 and Area 2 on clear days. I defined as a "clear day", when there are no deep white parts in the analysis area in RGB image. RGB image is made from band 1, band2 and band 3 of GOSAT/TANSO-CAI. I show RGB image and results of AOT of fine mode, coarse mode and total at wavelength of 500nm, RMSD, surface albedo (Ag) of all observed wavelength on some clear days in Figs. 4.5.7 to 4.5.9. White or black square in RGB composite image represents analysis area. Figures 4.5.7 and 4.5.8 are results of Area 1, and Figure 4.5.9 is result of Area 2. In almost of all pixels, RMSD values have been within 0.02, and solutions have converged. As shown in the figure, the distribution of AOT(fine) and AOT(coarse) were spatially smooth over the heterogeneous surface region.

In Area 1, the aerosol properties can simultaneously retrieved over several type surface, such as land and water surface, where there are no similar past studies to retrieve aerosol parameters. On both days of November 28 and December 1 in 2009 in Area 1, AOTs(coarse) in right side area of Chesapeake Bay show the same tendency and was lager than that in right side area. From the results, AOT(fine) in right area of the bay is larger than another area on November 28, 2009, but the value is smaller on December 1, 2009. On the other hand, the result of AOT(total) and AOT(coarse) suggests that AOT(fine) of top left corner area in Area 1 looks larger than that in the central region on both days.

In Area 2, AOT(fine) is large in south of Paris, and AOT(total) is large near the observation sites, urban area. I show the other clear day results in Area 2 in Figs. 4.5.10 and 4.5.11. Figure 4.5.10 is an RGB image of Area 2, and Fig. 4.5.11 denotes retrieval results of AOT(fine), AOT(coarse) and AOT(total). As shown in the figure, in all case, AOT(fine) in south of Paris is large, and AOT(coarse) is large around Palaiseau compared to other area. As seen above, I could obtain spatial characteristic distribution in urban areas by this algorithm.

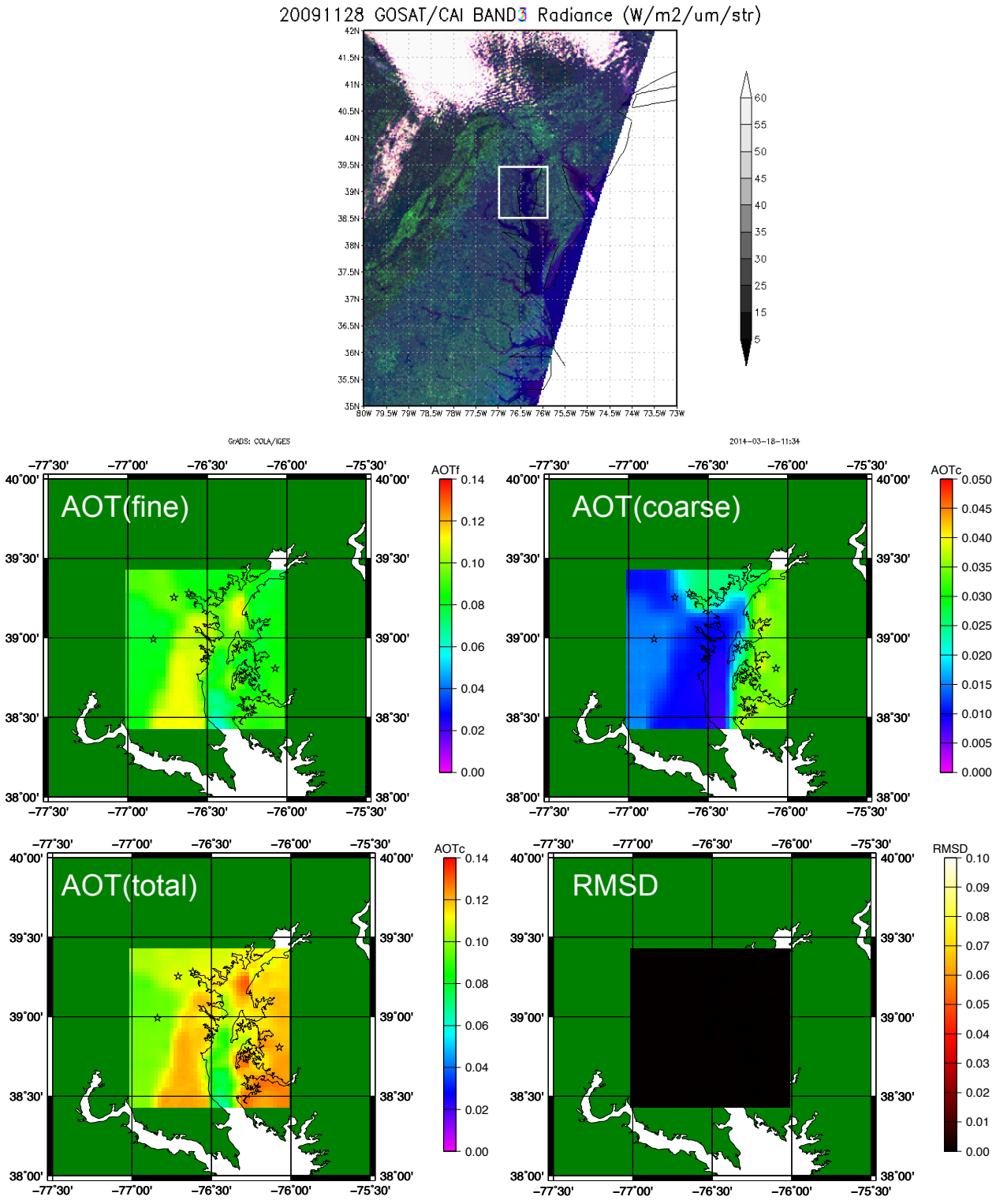

Figure 4.5.7a Retrieval result of AOT(fine), AOT(coarse), AOT(total) at wavelength of 500nm, and RMSD in Area 1 (76-77°W/38.7-39.4°N) on November 28, 2009. Top panel is RGB composite image made of band-1, band-2 and band-3.

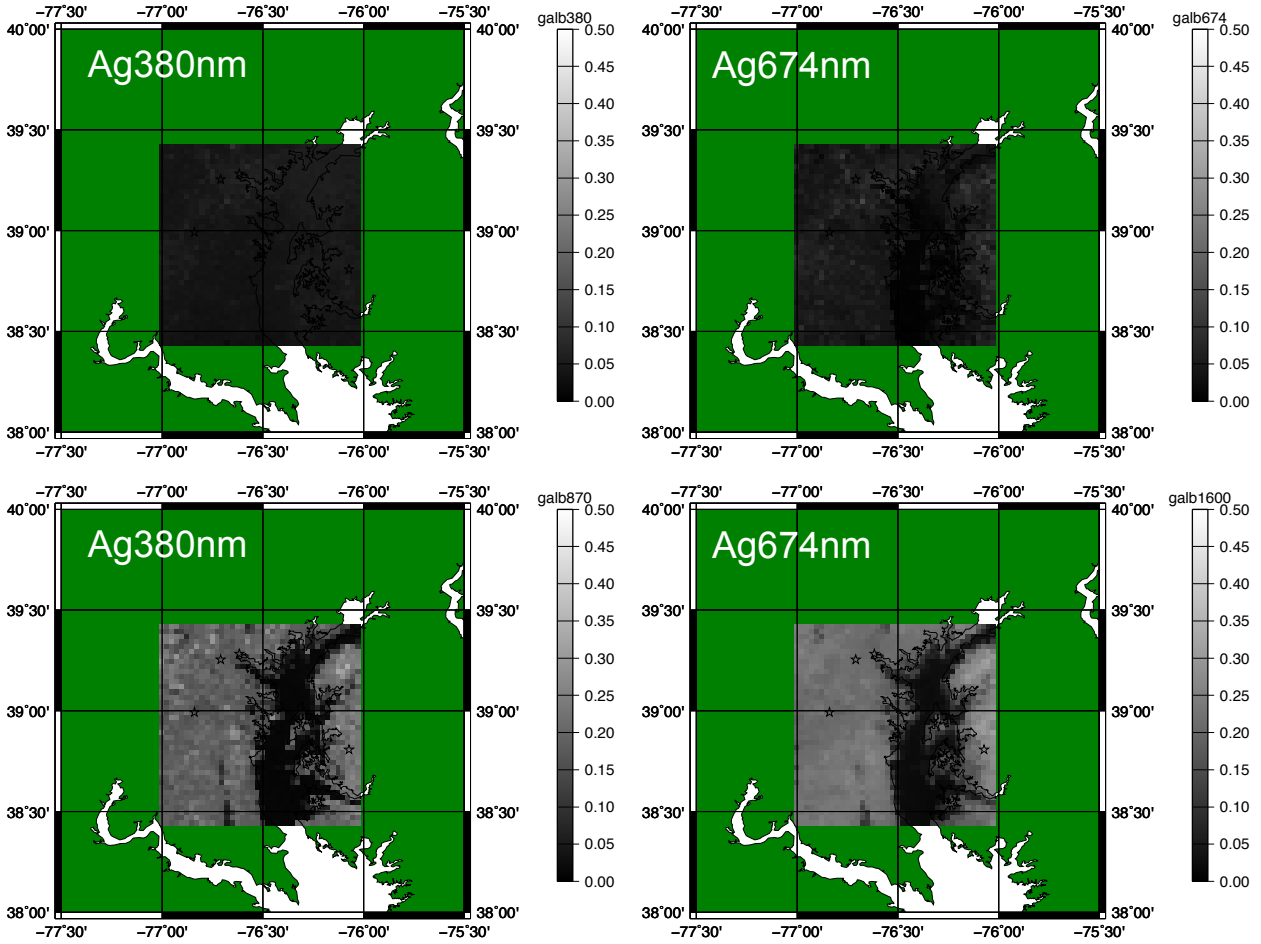

Figure 4.5.7b Retrieval result of surface albedo (Ag) at wavelengths of 380, 674, 870 and 1600nm in Area 1 on November 28, 2009.

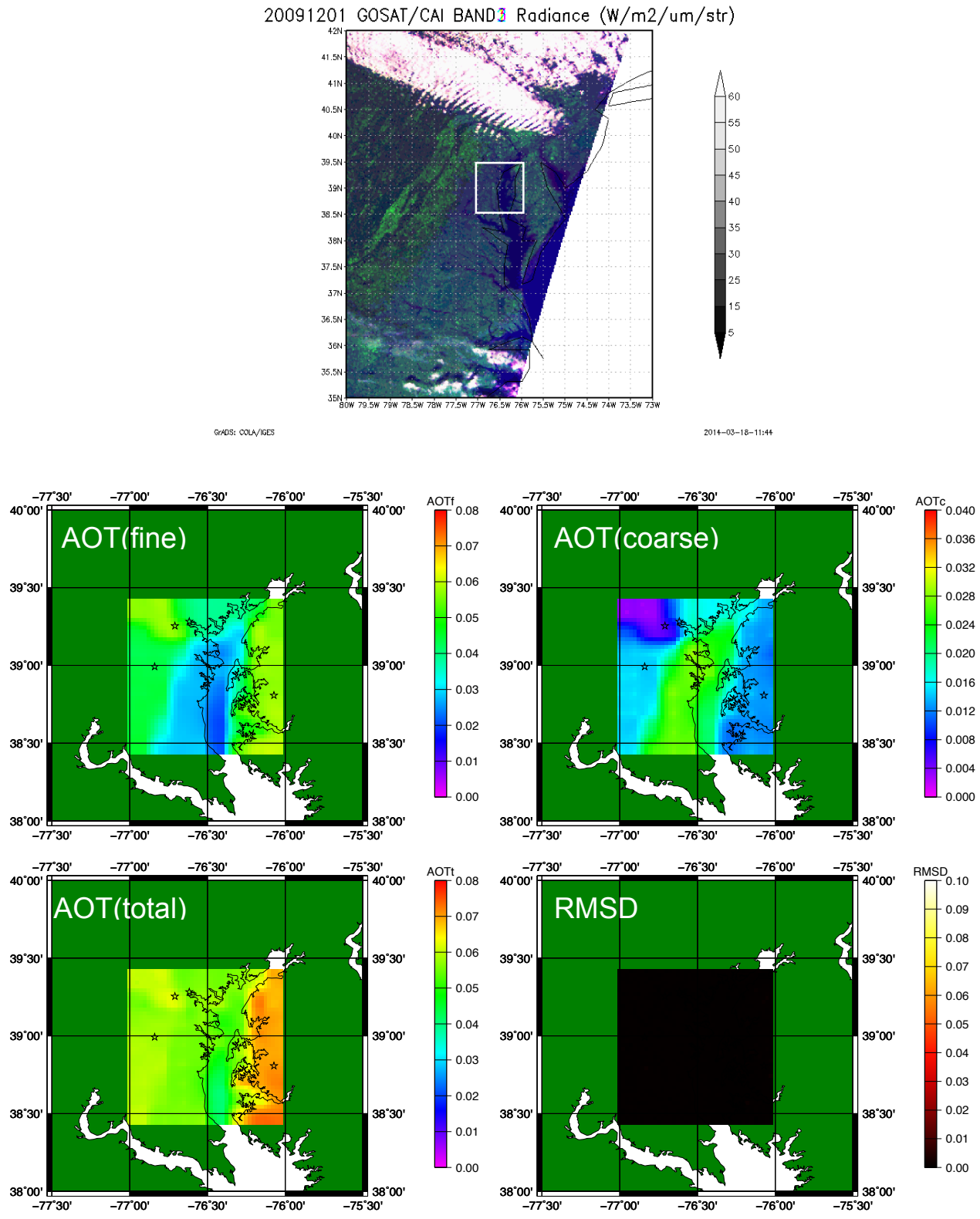

Figure 4.5.8a Same as in Fig. 4.5.7a, but on December 1, 2009.

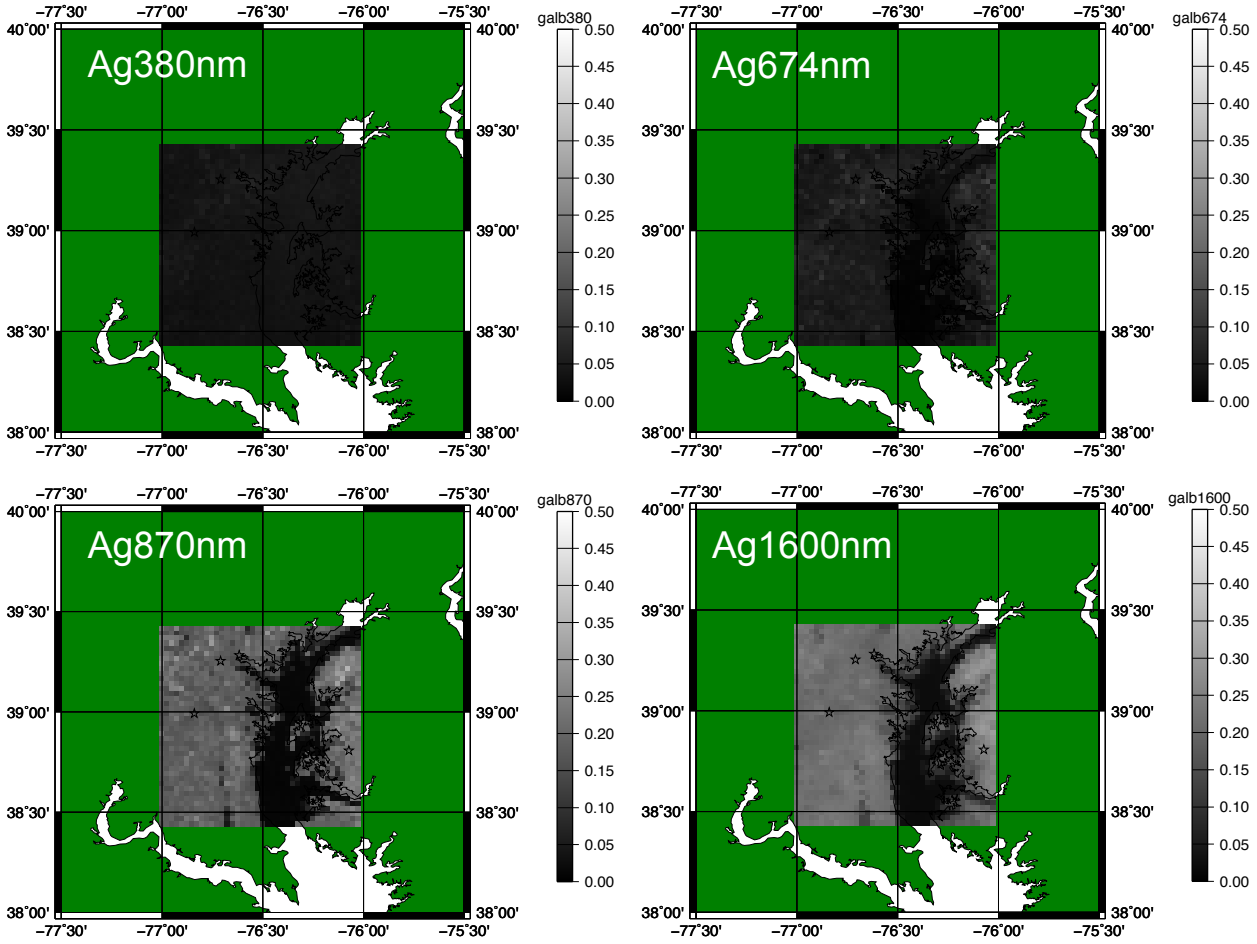

Figure 4.5.8b Same as in Fig. 4.5.7b, but on December 1, 2009.

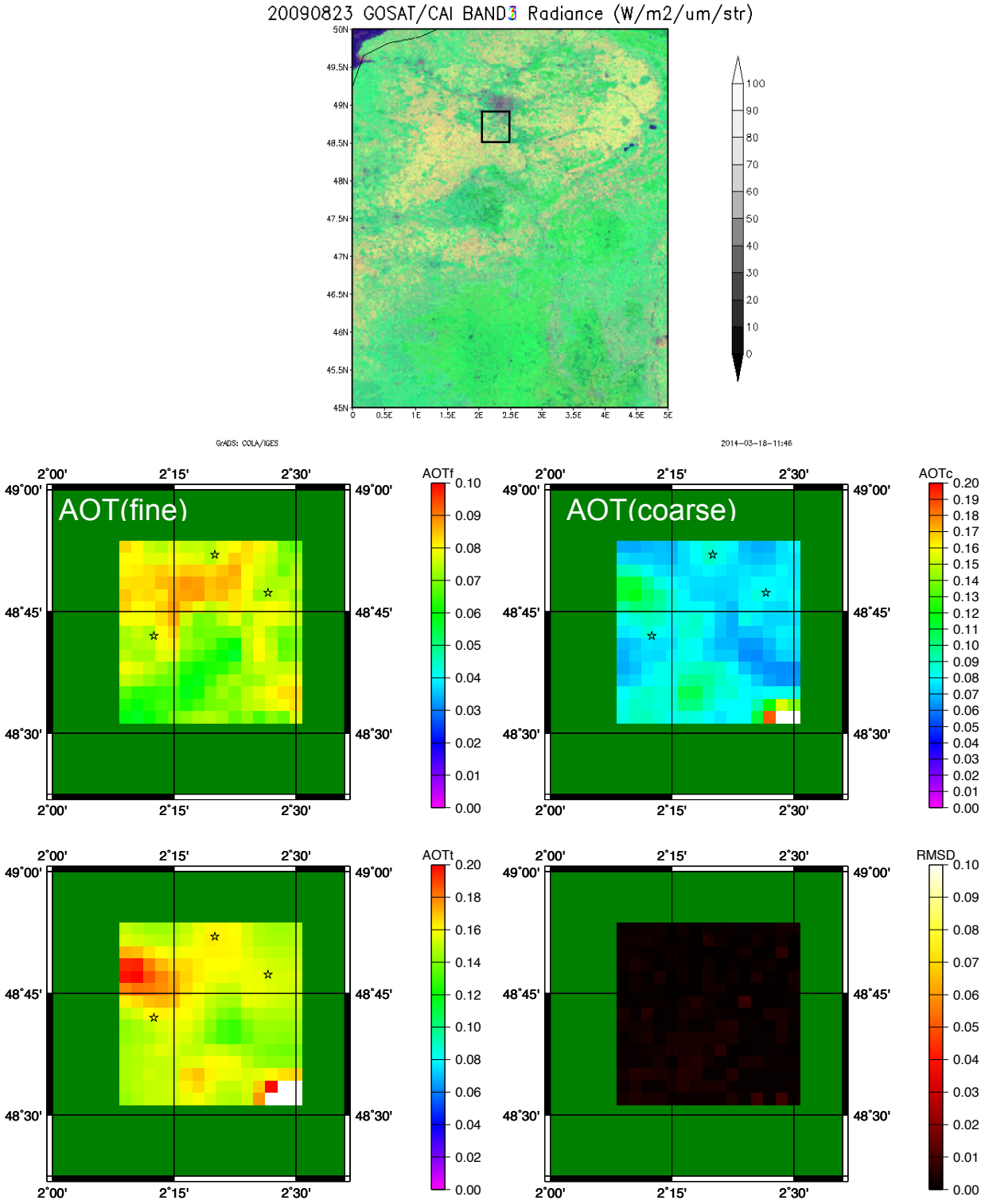

Figure 4.5.9a Same as in Fig. 4.5.7a, but in Area 2 (2.15-2.50°E/ 48.68-48.88°N) on August 23, 2009.

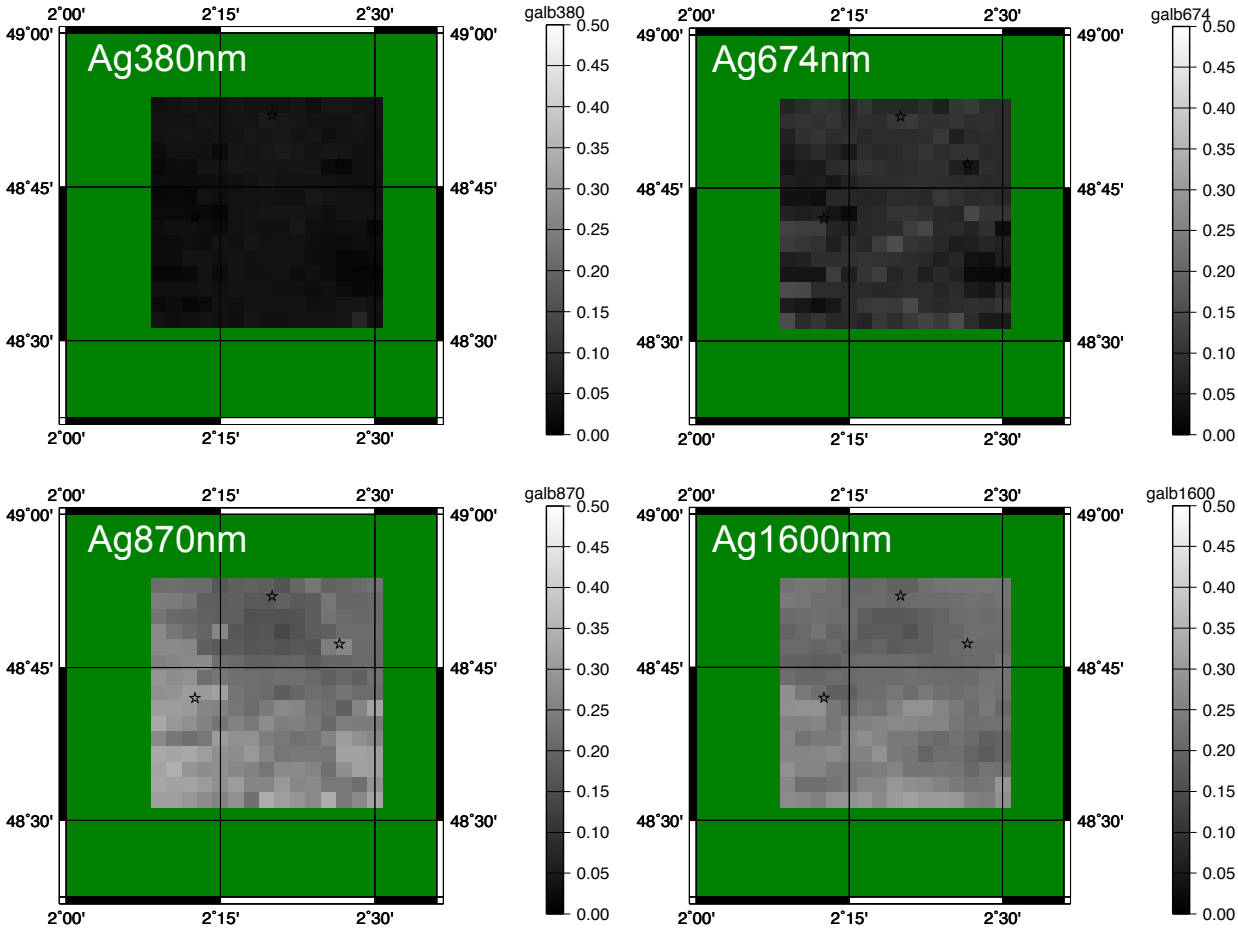

Figure 4.5.9b Same as in Fig. 4.5.7b, but in Area 2 on August 23, 2009.

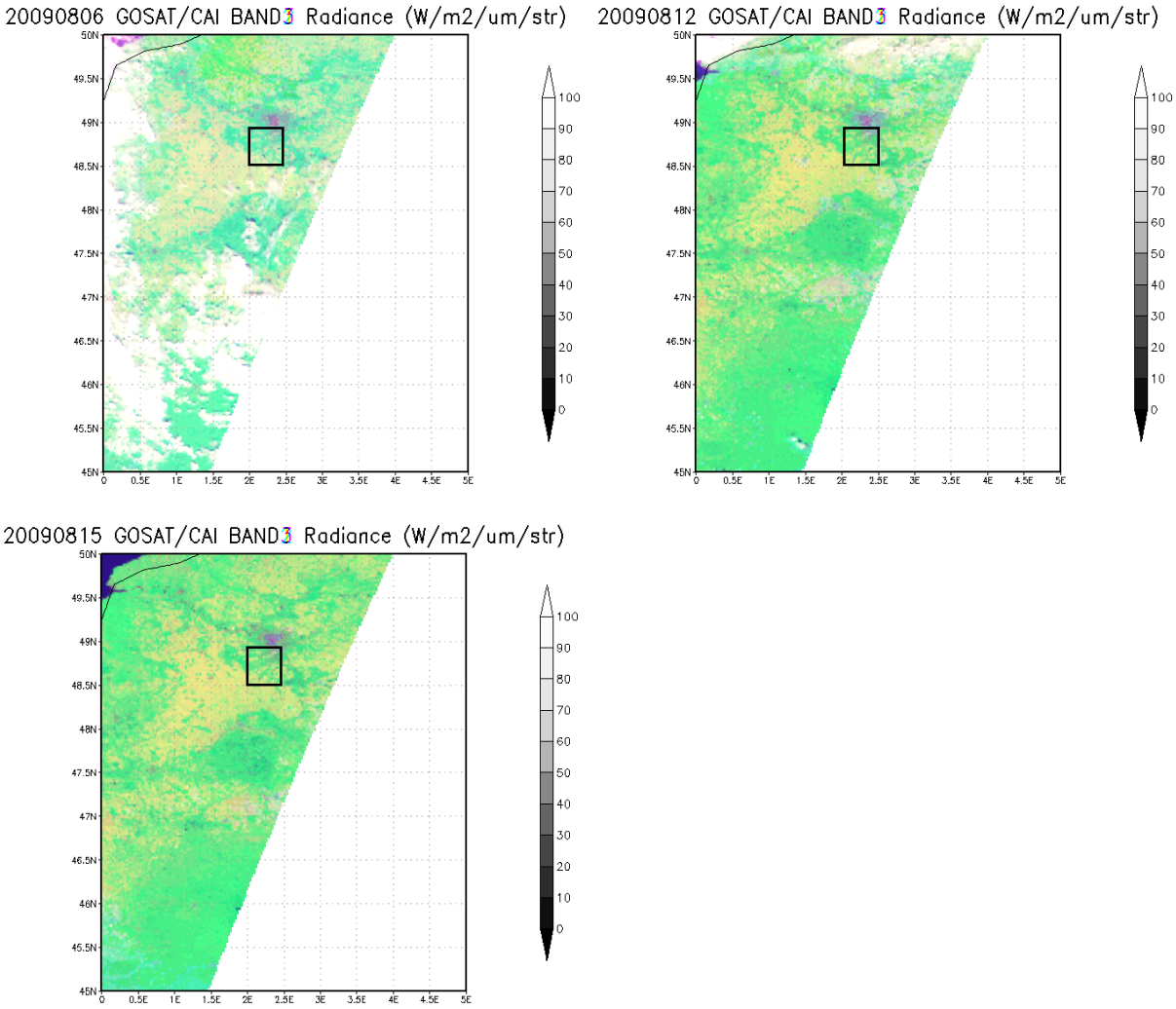

Figure 4.5.10a RGB composite images made from band 1, band2 and band 3 on August 6, August 12 and August 15 in 2009. Square in figures shows analysis area (Area 2) (2.15-2.50°E/ 48.68-48.88°N). There are no clouds (white parts) in the square in those cases, and it means the day is clear day.

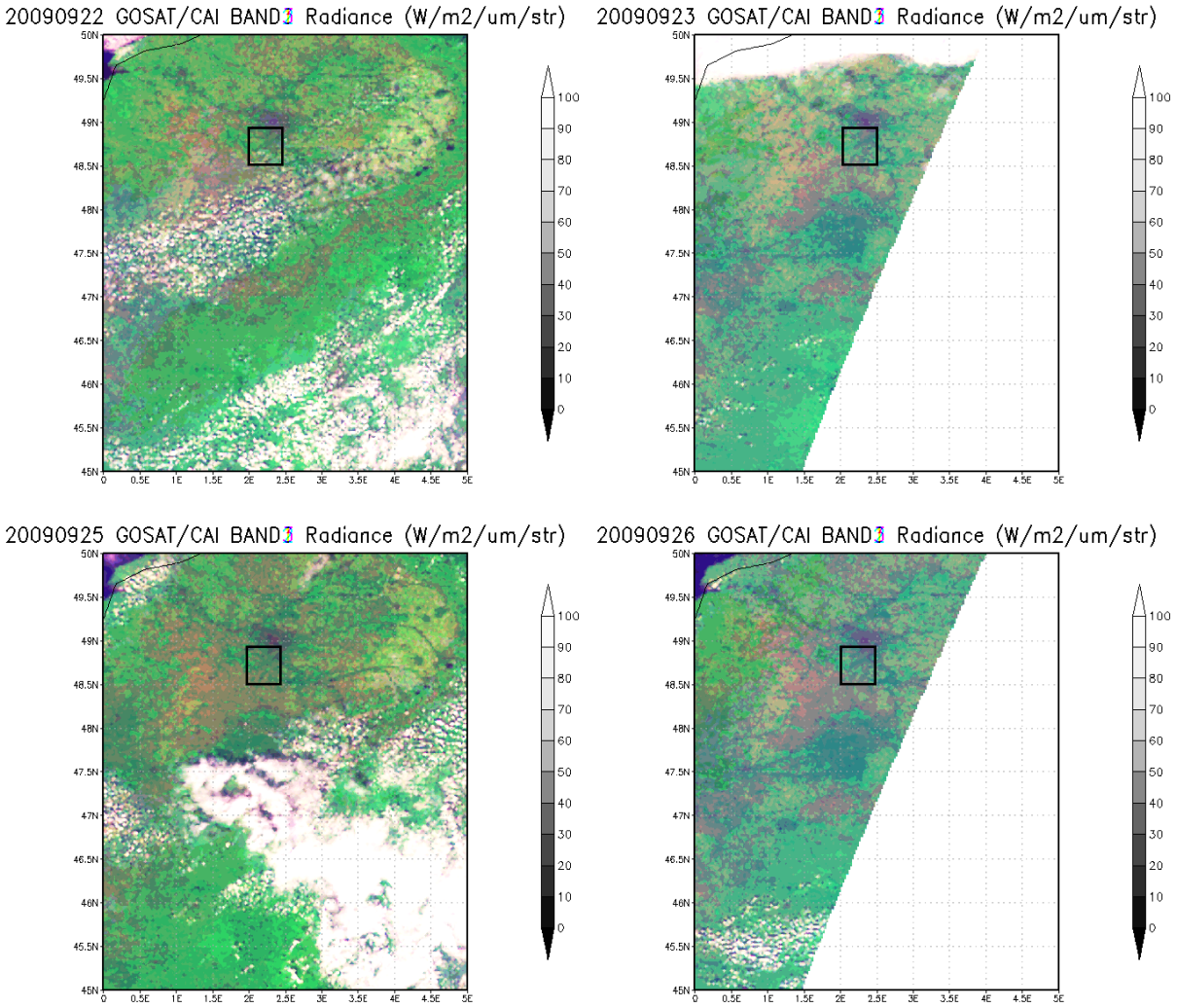

Figure 4.5.10b Same as in Fig. 4.5.10a, but for September 22, September 23, September 25 and September 26 in 2009.

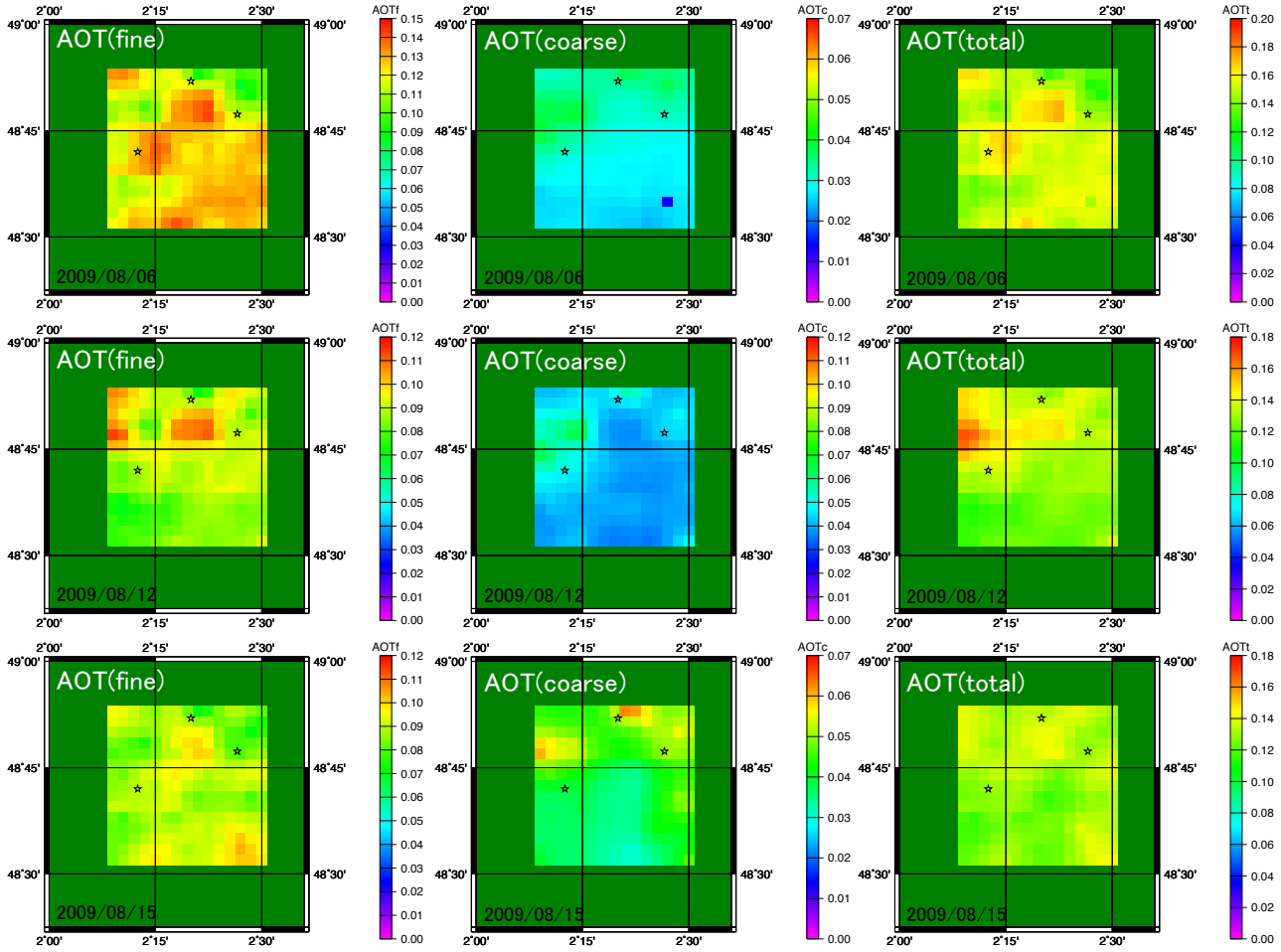

Figure 4.5.11a Retrieval result of AOT(fine), AOT(coarse) and AOT(total) at wavelength of 500nm on clear days over analysis region, on August 6, August 12 and August 15 in 2009 in Area 2 (2.15-2.50°E/ 48.68-48.88°N). Note that color bar takes differnent scales dipending on figures.

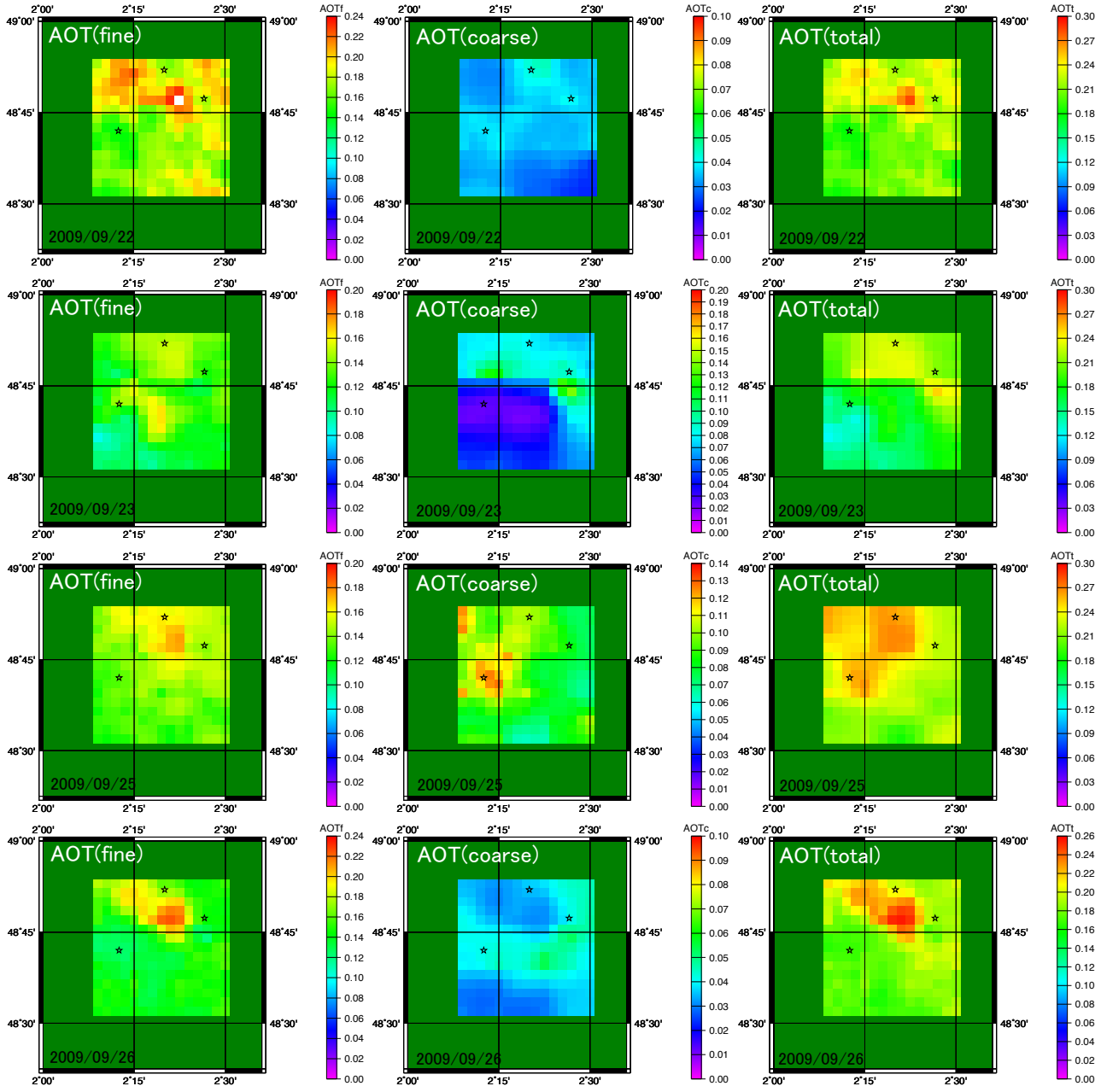

Figure 4.5.11b Same as in Fig. 4.5.11a, but for September 22, September 23, September 25 and September 26 in 2009.

In Figure 4.5.12, I compared the AOT total values at wavelength 500nm of clear day with AOT at wavelength 550nm derived by method of Fukuda et al. (2013), which retrieves AOT from GOSAT/TANSO-CAI imager data. Fukuda et al. (2013) has advantage of aerosol retrieval in desert region using near UV wavelength region where dust particles have absorbing feature.

As shown in the figure, previous method could not obtain reasonable spatial distribution of AOT. On the other hand, this new method could derive spatial distribution. Furthermore, AOT were simultaneously obtained in both land and water surface by the method.

Method of Fukuda et al. (2013) retrieves one pixel AOT at one time by fitting way and LUT method, so it is probably difficult to obtain AOTs when surface reflectance is spatially inhomogeneous including bright and dark surfaces like urban case, so smoothly distributed AOT was not obtained in this urban case. Moreover, this method retrieves AOT in sea water region and land surface region separately. On the other hand, this new algorithm retrieves aerosol parameters by the use of information of reflectance difference between pixels and at several wavelengths using wavelength-dependence of AOT by analyzing multi-pixel region at once, and it is an advantage of this algorithm and is different point from Fukuda et al., (2013). Furthermore, the method solves the problem by optimal method including measurement error information and constraint of retrieval parameters, such as a priori and smoothing constraint to spatial direction. Therefore, it is likely that aerosol parameters, such as AOT values, are retrieved stably.

Hence, AOT has become retrieved in urban area by this new algorithm, and the accuracy of urban AOT could be improved.

2009/11/28

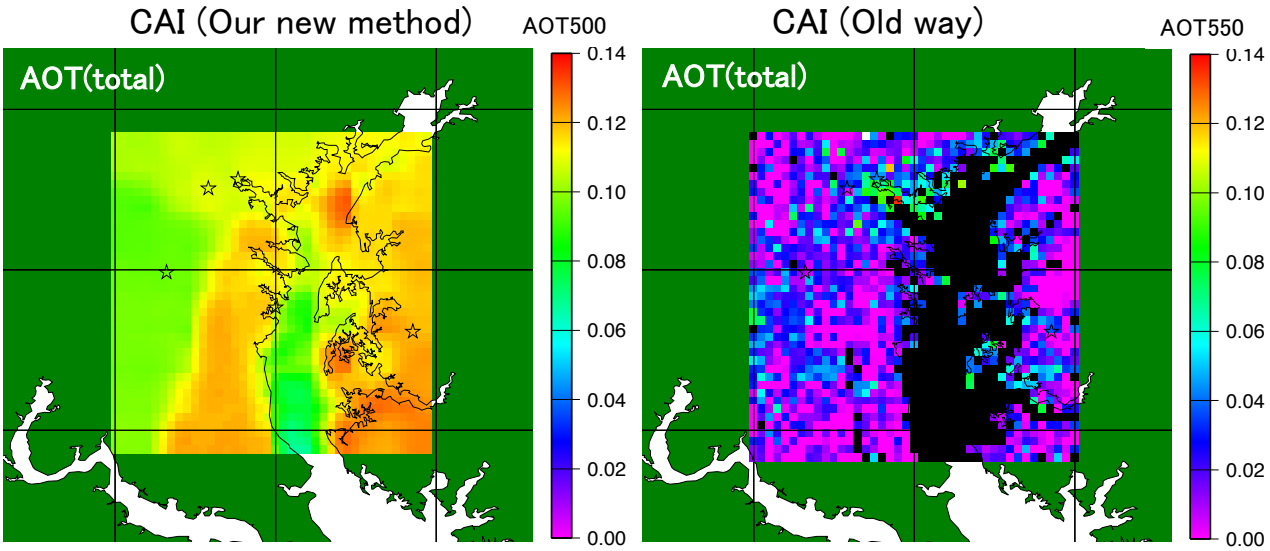

2009/12/01

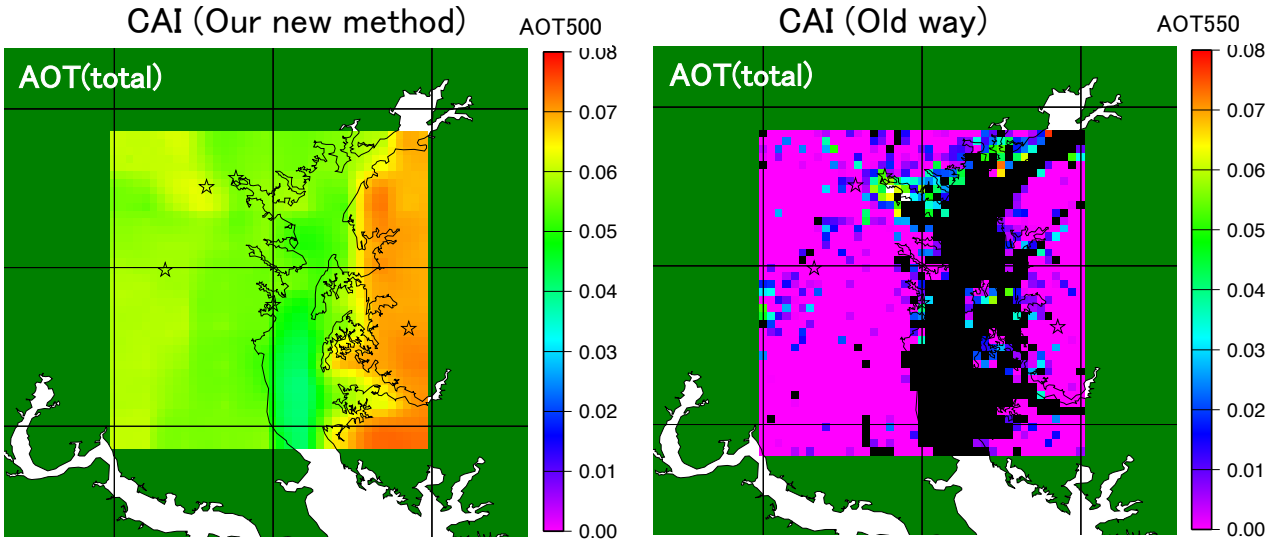

Figure 4.5.12 Comparison of retrieved AOT(total) at wavelength 500nm of clear day with AOT(total) at wavelength 550nm derived by a method of Fukuda et al. (2013). Top panel is the result on November 28, 2009; and bottom, on December 1, 2009

4.5.3 Comparison with MODIS AOT

There is tno AOT obtained by a pixel by pixel satellite product in urban area to be compared with my results. Therefore, I compare the result with results of other satellite or other algorithm; AOT of TANSO-CAI (this new method) vs AERONET with AOT of MODIS VS AERONET. Figure 4.5.13 is a figure from Hernandez et al. (2007), and shows the comparison of AOT from MODIS with that from AERONET in NYC that is an urban site. The red circles in the figure show the matchup between AERONET and the closest MODIS pixel, while the blue circles denote the minimum AOT within a 40 km box. They state that this matchup was based on the reasonable assumption that the minimum AOT will occur for pixels, which are over dark surfaces such as dense vegetation. They pointed out that there are inherent weaknesses which make the approach less useful for aerosol monitoring in urban area, and that the northeast coast resulted in remarkably high MODIS overestimation. The same problem is also pointed out in Chu et al. (2002). The result shows, retrieved AOT over urban area is not in agreement with ground-based observation, if they do not select matchup data attentively. One possible problem is the estimation of surface albedo, because they use mean surface albedo in 400 pixels or 10 km box area. In the area composed of heterogeneous surface albedo like urban area that dark and bright surfaces are complexly mixed, the albedo assumption is not effective. On the other hand, the new algorithm works well in heterogeneous surface or urban area as well as over dark surface area from numerical experiment in Chapter 3 and validation results. Figure 4.5.14 is the result of total AOT at wavelength of 500nm at GSFC, UMBC and SERC in the northeast coast of the United States. The red circles in the figure represent the matchup between AERONET and the closest TANSO-CAI pixel. Although the comparison data is few, AOT values retrieved by this method are in agreement with AOT derived from ground-based AERONET observation. Hence, it is concluded that AOT values in urban area can be retrieved by the multi-wavelength and multi-pixel method.

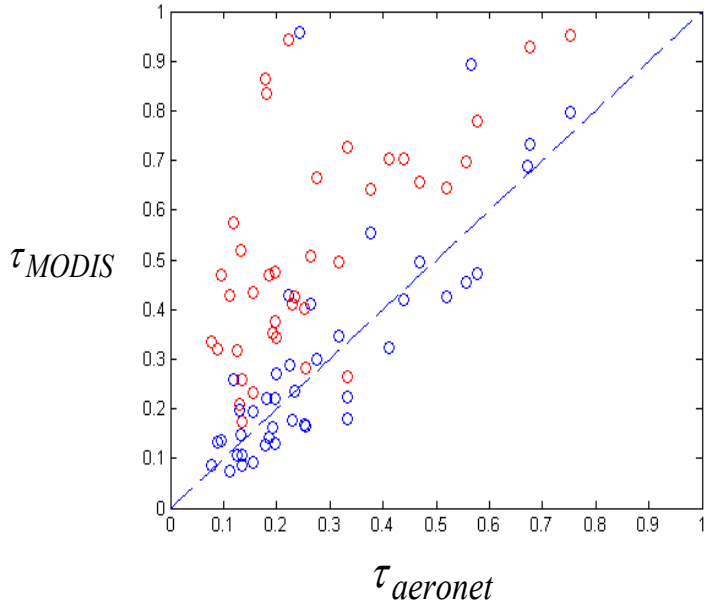

Figure 4.5.13 Intercomparison between AERONET and MODIS AOT at Northeast urban area (NYC) in United States (Hernandez et al., 2007). The red circles are matchup between AERONET and the closest MODIS pixel, while the blue circles is the minimum AOT within a 40 km box.

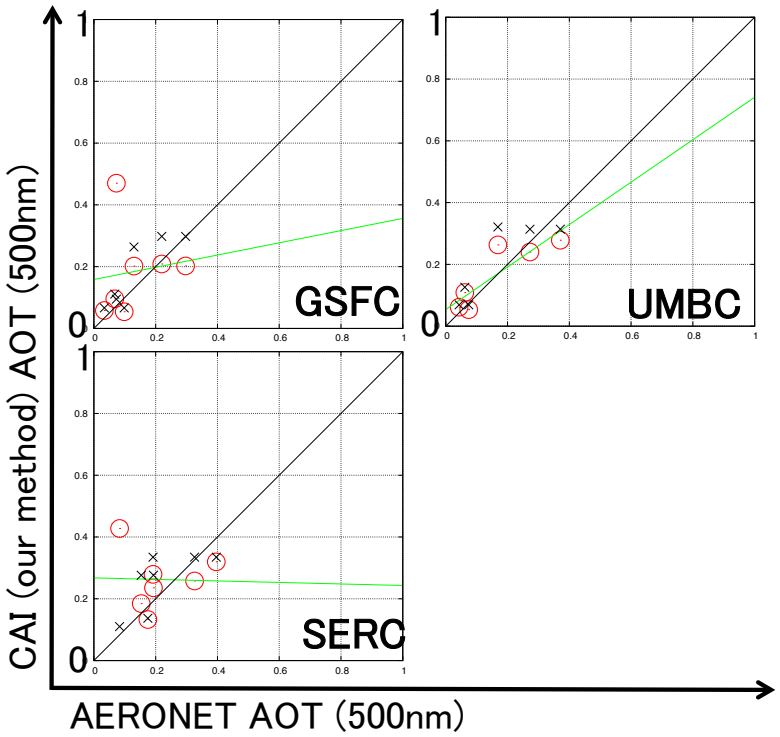

Figure 4.5.14 Comparison between AERONET and TANSO-CAI AOT retrieved by this algorithm at Northeast urban area (GSFC, UMBC and SERC) in United States. The red circles are matchup between AERONET and the closest TANSO-CAI pixel

4.5.4 Soot fraction

Aerosol optical property of absorption such as single scattering albedo (SSA) is difficult to retrieve either from ground or from space. Nowadays, it is considered that the retrieval accuracy or error of SSA from ground-based remote sensing is ±0.05. However, SSA is an important parameter to assess aerosol radiative forcing, and it is pointed out that SSA difference of 0.1 (0.85 to 0.95) makes direct radiative forcing change from positive to negative (Ramanathan et al., 2001). AERONET derives SSA when AOT at wavelength 440nm is lager than 0.4, and there are no retrieved soot fractions (SF) to be able to be compared. Therefore, I compared an absorption parameter, SSA instead of SF at Beijing site (116.3813°E/116.3813°E) where AOT is often high and larger than 0.4 at wavelength 440nm. And also, Beijing includes urban areas.

I first compare retrieved AOT values by this method from TANSO-CAI imager data with that of AERONET in Figure 4.5.15. The period is from July 2009 to December 2009. Cross marks denote a priori value I gave (i.e. a priori AOT versus AETONET AOT). AOT retrieved by the method is in almost agreement with that of AERONET.

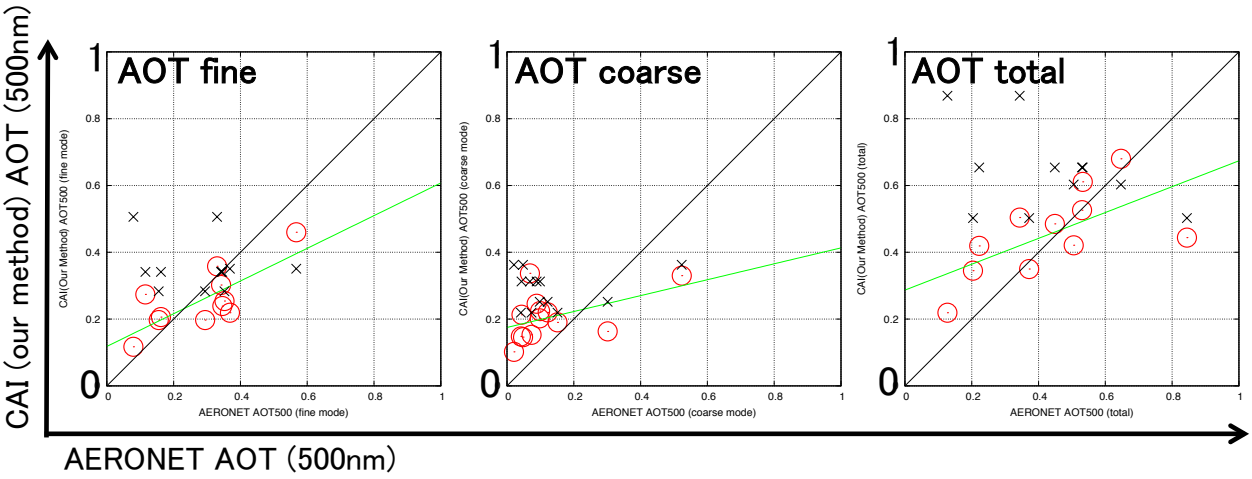

Figure 4.5.15 Same as in Fig. 4.5.4, but at Beijing site.

I show the time series of AOT(total), AOT(fine) and AOT(coarse) retrieved by this method in Figure 4.5.16. And also, I represent time series of SSA retrieved by the method (red) and AERONET SSA (blue) in Figure 4.5.15, and plot monthly value of retrieved SSA in the figure. In both figures, the x-axis denotes day number from 1 January 2009. We can see that the AOT(fine) and AOT(coarse) have varied day by day.

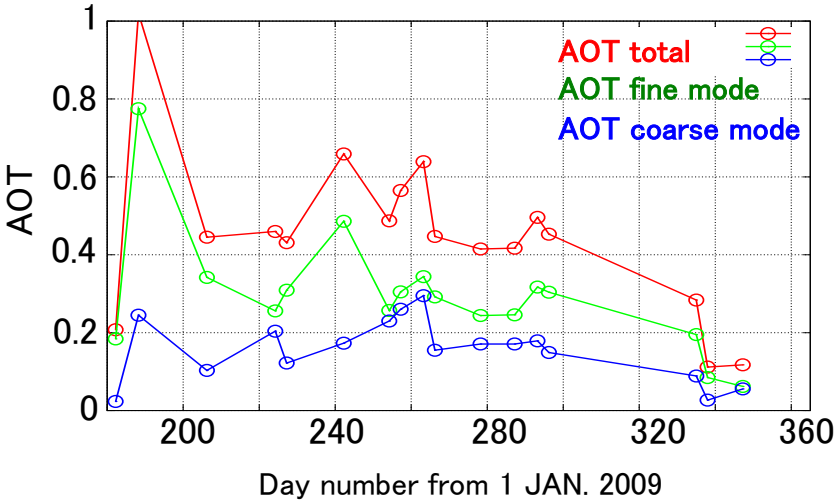

Figure 4.5.16　Time series plot of AOT(total) (red), AOT(fine) (green) and AOT(coarse) (blue) at wavelength of 500nm retrieved by this method at Beijing. X-axis is a day number from January 1, 2009.

For SSA in Figure 4.5.17, although SSA retrieved by this method is not in good agreement with AERONET SSA, the trend that SSA in winter (or December) is relatively high compared with SSA in summer looks similar.

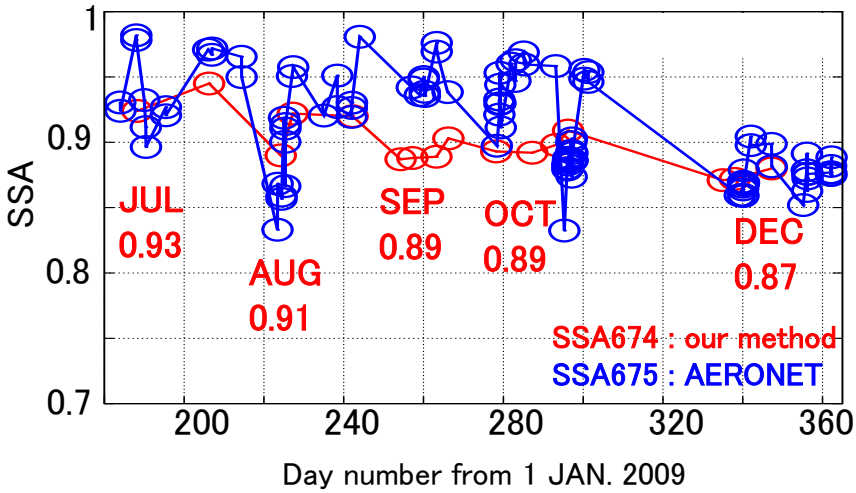

Figure 4.5.17　Time series plot of SSA at wavelength of 674nm retrieved by this method at the closest CAI pixel to AERONET site (red), and AERONET SSA at 675nm (blue) at Beijing. I show monthly mean value of CAI SSA in the figure. X-axis is a day number from January 1, 2009.

Additionally, according to in situ measurement of BC in Beijing in 2009 (Song et al., 2013), BC concentration in winter is larger than that in summer, because a large amount of coal (~5Tg) was still used for residential heating in the winter of 2009 (Beijing Municipal Bureau of Statistics, 2010). In urban area of Beijing, average values of BC concentrations are 8.1μg m^{-3} in summer and 16.1μg m^{-3} in winter. Figure 4.5.18 (Song et al., 2013) shows daily cycles of BC concentrations at three sites (Roadside, Urban and Rural) in Beijing, and error bars are standard deviations. From the figure, BC concentration in winter is larger than that in summer. The trend of this result is in agreement with trend of my result.

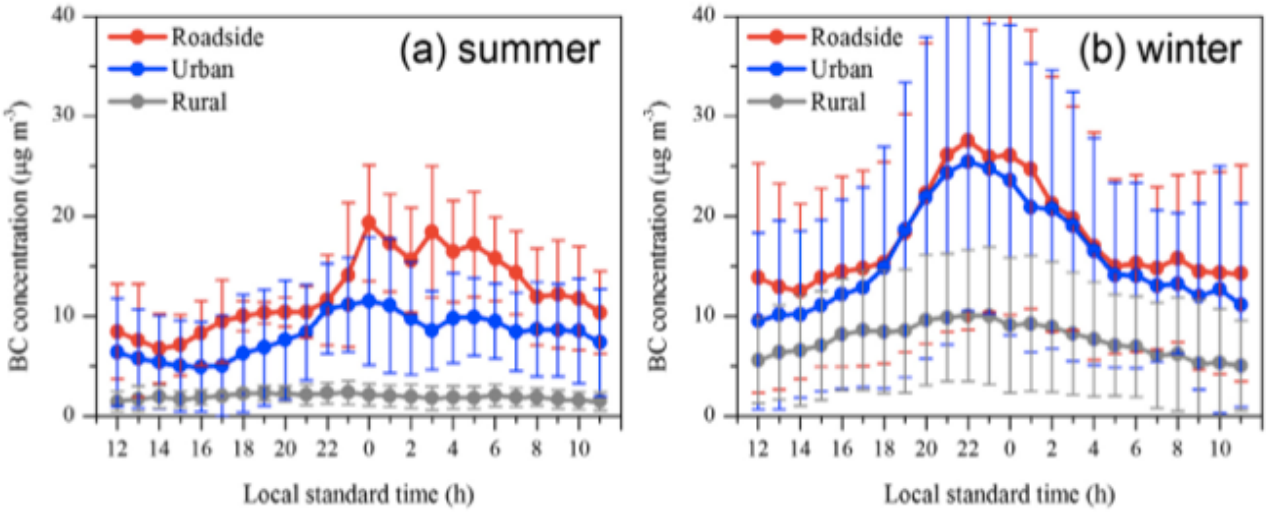

Figure 4.5.18 Daily cycles of BC concentrations in summer and winter at three sites (Roadside, Urban and Rural) in Beijing. Error bars are standard deviations (Song et al., 2013)

Furthermore, it is known that in Beijing the relative humidity (RH) in winter is smaller than that in summer (e.g. RH is 60~70% in summer and 40~55% in winter, at Beijing in 2007 (Wen et al., 2010)). RH is one of possible causes of SSA difference between summer and winter. SSA values are increased by hydroscopic growth of aerosol particles, and this algorithm includes the hydroscopic growth of aerosol particles. I show the numerical calculation results of different RH using RSTAR in Figure 4.5.19. In this calculation, I set AOT500(fine)=0.2, SF=0.03, and RH=0.5(50%), 0.8(80%), 0.99(99%), and a default condition values of US standard atmosphere in RATAR. I used aerosol models in Table 4.4.4. As shown in the figure, SSA value in a high RH case is larger than that in a low RH case. The reason why wavelength dependence of AOT in a case of RH=0.99 is different from others is a strong hydroscopic grows of aerosol particle by high RH.

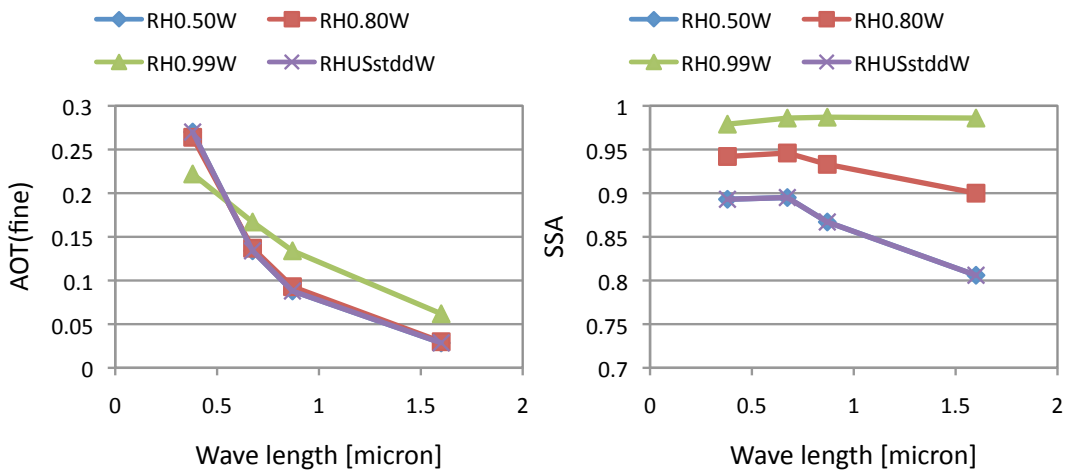

Figure 4.5.19 Numerical calculation result of different relative humidity (RH) using RSTAR. Left and right panels are AOT(fine) and SSA of different RH, respectively. Blue denote the case that RH=50%; red, RH=80%; green, RH=99%; purple, US standard which is an default atmospheric condition in RSTAR.

Therefore, possible causes of the trend that SSA in winter is lower than SSA in summer at Beijing in 2009 are high BC concentration by heating and low RH compared with that in summer. However, most of data, specifically in November and December are screened out because of cloud and low retrieval accuracy, so it is difficult to claim robustness of the SSA values from these results. I need more analysis and validations.

4.5.5 Comparison other region with ground-based observations

In this section, I show the results in several other regions. Each analysis region is composed of 16 sub-domains or 400 pixels, and includes an AERONET or SKYNET site in Figure 4.5.20 and Table 4.5.3.

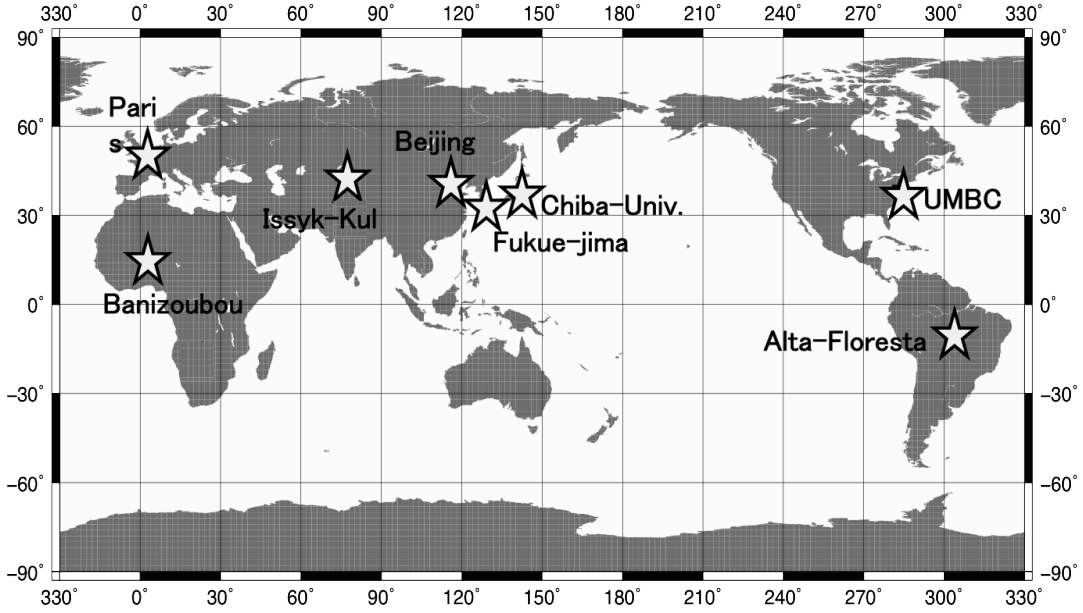

Figure 4.5.20 Location of ground-based observation sites (AERONET and SKYNET) for comparison.

Table 4.5.3 Location of ground-based observation sites (AERONET and SKYNET) for comparison

Site name	Longitude	Latitude	Ground-based network	
Alta-Floresta	56.1044°W	9.8713°S	AERONET	Vegetation(South America)
Issyk-Kul	76.9830°E	42.6227°N	AERONET	Lake side (Asia)
Banizoumbou	2.6648°E	13.5412°N	AERONET	Desert (Sahara)
Chiba Univ.	140.1240°E	35.6220°N	SKYNET	City area (Japan)
Fukue-jima	128.6820°E	32.7520°N	SKYNET	Island (japan)

I show result of comparisons between AERONET or SKYNET and the closest TANSO-CAI pixel at sates of Table 4.3.5 in Figure 4.5.21. Red circles in the figure represent the comparison result, and cross marks denote a priori values.

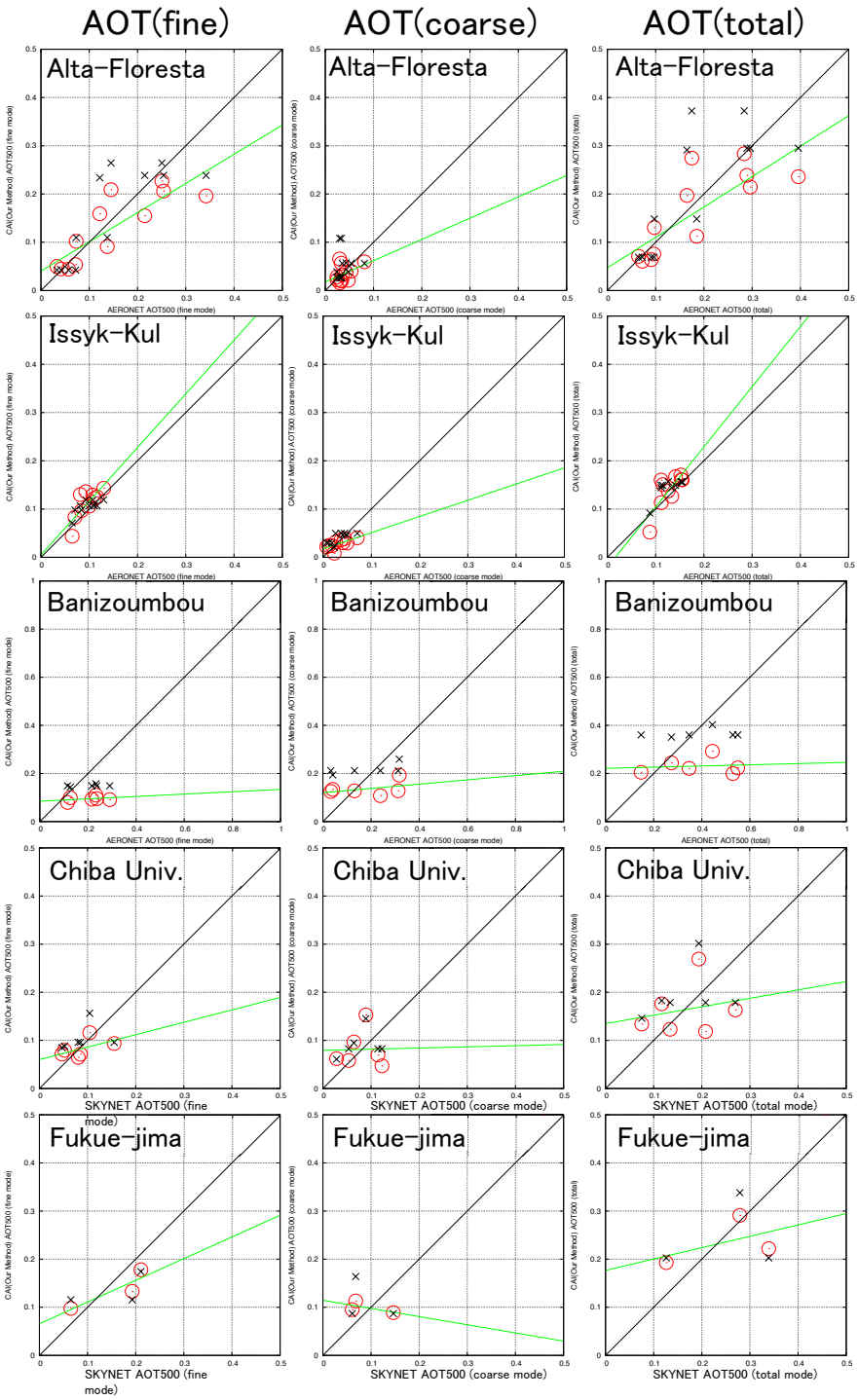

Figure 4.5.21　Comparison of AOT(fine) (left panel), AOT(coarse) (center) and AOT(total) (right) at wavelength of 500nm between AETONET or SKYNET and the closest pixel of CAI with this method at sites of Table 4.5.3. Red circle is a comparison of AOT, cross mark denotes a priori of AOT. Analysis period is July 2009 to December 2009.

At sites of Alta-Floresta and Issyk-Kul, AOTs derived by this method are in good agreement with AERONET AOT. Alta-Floresta is a site in vegetation area, and Issyk-Kul is a lakeside site of Lake Issyk Kul that is an endorheic lake in the northern Tian Snan mountains. In Banizoumbou, Chiba Univ. and Fukue-jima, almost of all data are screened by data selection condition, so I ease the selection condition of an observation time difference between GOSAT/TANSO-CAI and AERONET from 0.05 (1.2 hour) to 0.10 (2.4 hour). At Banizoumbou site in Saharan desert, AOT retrieved by the method is not agreement with AERONET AOT. In this case, analysis area in a sub-domain is almost homogeneous and bright surface, and it is a possible cause of the disagreement. Other possible cause is the aerosol model used by the analysis, because it is likely that an imaginary part of refractive index of aerosol models of fine and coarse mode is a little bit larger for Saharan dust. I have used urban type aerosol model for fine mode and yellow sand with soot model for coarse mode in this analysis, so I should investigate appropriate aerosol model for each region and change aerosol models for each region in the future. In Chiba Univ. and Fukue-jima sites, AOT variability of comparison result looks a little bit large and the number of comparison data is few because of cloud and time difference between GOSAT/TANSO-CAI and AERONET, but the almost of all AOT at both sites can be retrieved within 0.1 from AERONET. However, I need more analysis to validate and compare retrieval values with other observations.

Table 4.5.4 shows AOT difference between AERONET and the closest TANSO-CAI pixel calculated by Equation 4.5.1. AOT difference was ±0.025 at Issyk-Kul, and it was in good agreement with ground-surface observation. On the other hand, AOT difference at Banizoubou was large and was ±0.268. The other sites, AOT difference was about ±0.06 to ±0.08. This value is likely good results compared with present AOT retrieval accuracy over land by satellite remote sensing, or ±0.05±0.2AOT or5~30% (Kaufman et al., 2002; Chu et al., 2003; Lee et al., 2009). However, I need more data to estimate this value.

Table 4.5.4 Retrieval accuracy: AOT difference from AOT of AETONET or SKYNET of each site (ΔAOT or $\Delta\tau$). See Equation 4.5.1 for calculation. ΔTime is observation time difference between TANSO-CAI and AERONET.

	ΔAOT(total)	ΔAOT(fine)	ΔAOT(coarse)	ΔTime
Alta-Floresta	±0.067	±0.056	±0.018	< 1.2h
Issyk-Kul	±0.025	±0.024	±0.015	< 1.2h
Banizoubou	±0.268	±0.158	±0.141	< 1.2h
Chiba Univ.	±0.066	±0.042	±0.062	< 1.2h
Fukue-jima	±0.078	±0.044	±0.046	< 1.2h

I also show time series of AOT retrieved by the method and AERONET or SKYNET AOT at UMBC, Paris, Alta-Floresta, Issyk-Kul, Banizoumbou, Chiba-Univ., and Fukue-jima in Fig. 4.5.22. Error bar in the figure represent retrieval error $\hat{\sigma}$ calculated as follows,

$$\hat{\mathbf{S}} = (\mathbf{K}^{\mathrm{T}}\mathbf{S}_e^{-1}\mathbf{K} + \mathbf{S}_a'^{-1})^{-1} \quad (4.5.2a)$$

$$\mathbf{S}_a' = <(\boldsymbol{u} - \boldsymbol{u}_a)(\boldsymbol{u} - \boldsymbol{u}_a)^{\mathrm{T}}> \quad (4.5.2b)$$

$$\hat{\sigma} = \sqrt{\hat{S}} \quad (4.5.2c)$$

where, $\hat{\mathbf{S}}$ is called the covariance of the solution or total error covariance (Rodgers, 2000), $\mathbf{S}_e$ is the measurement error covariance, $\boldsymbol{u}_a$ is the a priori values of retrieved parameter, $\boldsymbol{u}$, and $\mathbf{S}_a'$ is the associated covariance matrix. $\mathbf{K}$ is Jacobian matrix of radiance for each parameter. Time series of retrieval error is also shown in Fig. 4.5.23. We can see that retrieved AOT is probably not depend on a priori value when $\hat{\sigma}$ is small.

From the result, retrieved AOT at Banizoumbou is not agreement with AERONET AOT and retrieval error is large (~0.1). Almost of all retrieval errors of AOT(fine) and AOT(coarse) in each site, other than Banizoumbu, are smaller than 0.06. We can see seasonal variation of AOT at UMBC, Alta-Floresta and Issyk-Kul. In North and South American region, AOT in July and August at UMBC is higher than September and December, and AOT in July at Alta-Floresta is small and in September to November is large. Those tendencies are reported by Zhang et al. (2012). The former have shown daytime variation of aerosol with seasonal distinction by using multiyear measurements from 1997 of AERONET sites over North America, South America. For the result at Issyk-Kul where located 1650m above sea level, AOT is large in July (~0.2) and decrease with month, and this trend is consistent with measurement result using handheld sun photometer Microtops II by Semenov et al. (2005) and result by WMO Global Ozone Research and Monitoring Project Report (No. 53), Kyrgyzstan (by NDSC network).

As for other site, AOT vary from 0.1 to 0.3, but characteristic variation or peak of AOT could not be seen. To discuss the characteristic of regional or seasonal aerosol properties, I need to analyze more data as future task.

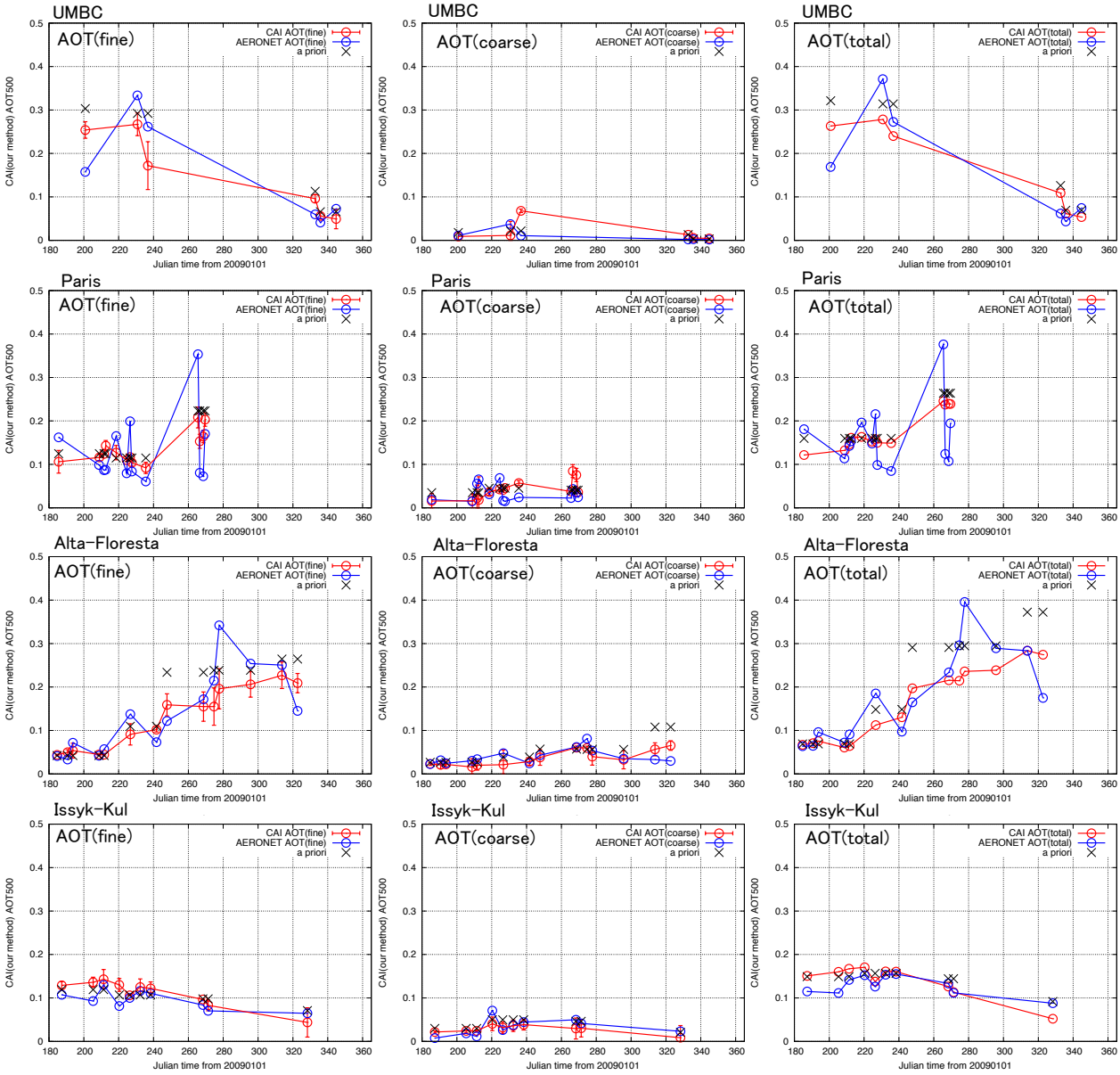

Figure 4.5.22a Time series plot of AOT(fine) (left), AOT(coarse) (center) and AOT(total) (right) at wavelength of 500nm retrieved by my method (red) and derived by AERONET or SKYNET (blue) at UMBC, Paris, Alta-Floresta and Issyk-Kul (Table 4.5.2). X-axis is a day number from January 1, 2009. Error bar in the figure denotes retrieval error calculated by Eq. (4.5.2c).

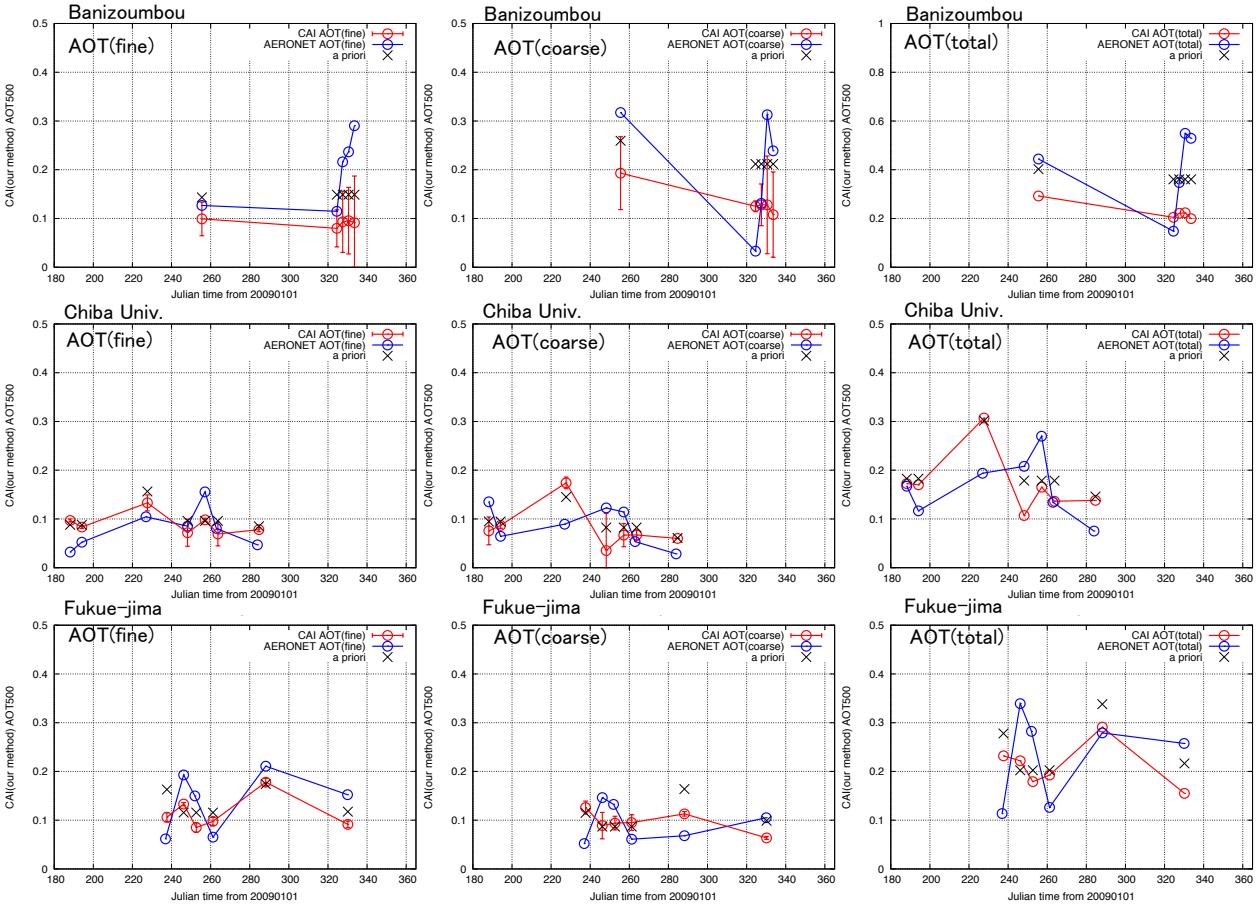

Figure 4.5.22b Same as Fig. 4.5.22a, but at Banizoumbou, Chiba-univ. and Fukue-jima.

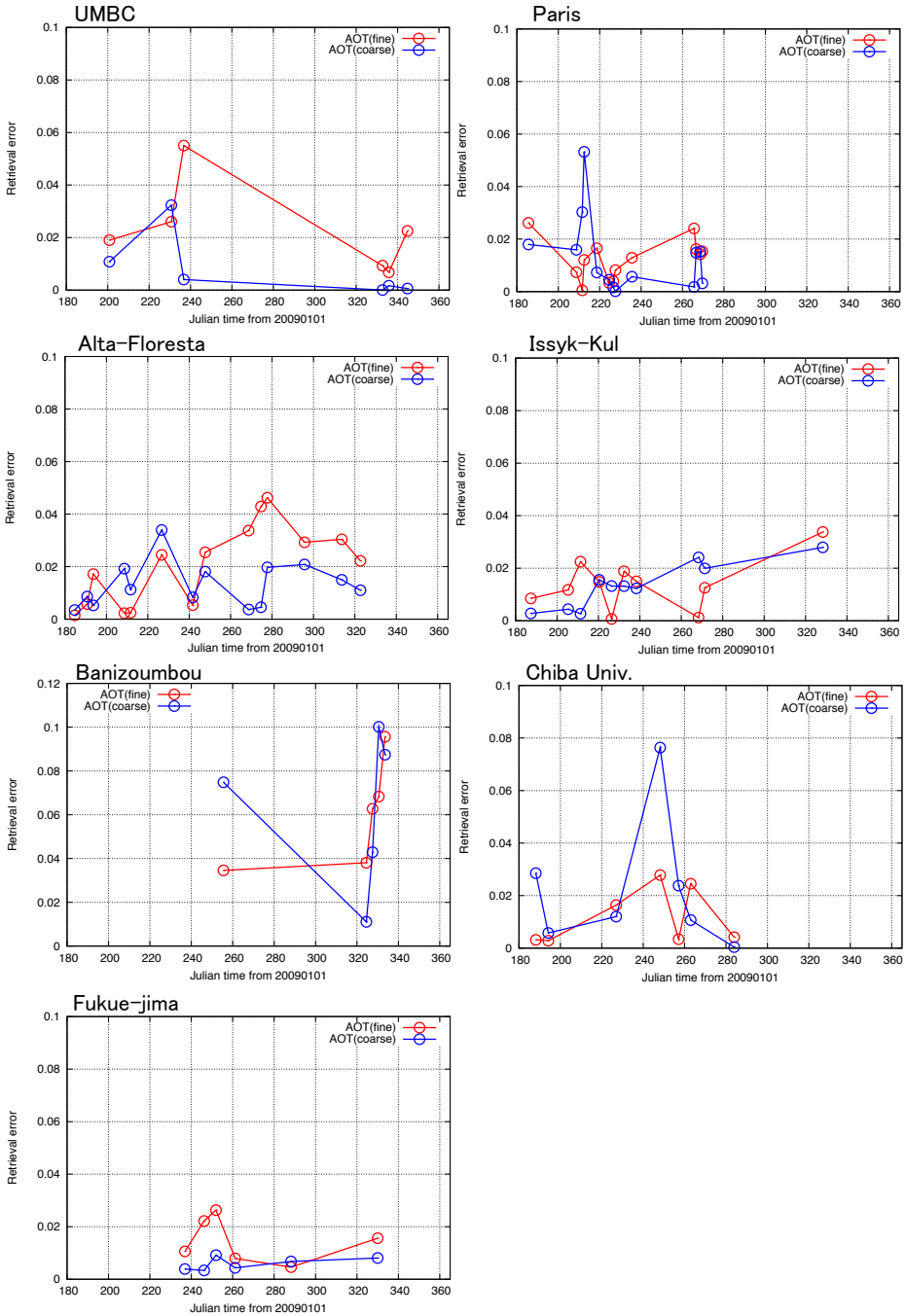

Figure 4.5.23 Time seriese of retrieval error $\hat{\sigma}$ of AOT(fine) (red) and AOT(coarse) (blue) at UMBC, Paris, Alta-Floresta, Issyk-Kul, Banizoumbou, Chiba-univ. and Fukue-jima. X-axis is a day number from January 1, 2009. Note that range of Y-axis of Banizoumbou is different from the other sites.

Figures 4.5.24 shows time series of error reduction ratio (*ERR*),

$$ERR = 1 - \frac{\hat{S}}{\hat{S}_a} \tag{4.5.3a}$$

$$\hat{\mathbf{S}}_a = (\mathbf{K}^{\mathrm{T}}\mathbf{S}_e^{-1}\mathbf{K} + \mathbf{S}_a^{-1})^{-1} \tag{4.5.3b}$$

where $\mathbf{S}_a$ is a priori covariance matrix, and definitions of other parameters are same as Eqs. (4.5.2a) to (4.5.2c). *ERR* is one of parameter to show retrieval accuracy, and retrieval accuracy is likely good when the value is large. I also show time series of minimum reflectance corrected by Fukuda et al. (2013) as surface albedo in Fig. 4.5.25. The circle point in the figure denotes the mean surface albedo of 10×10pixel around each observation site, and error bar represents the standard deviation of surface albedo. If the standard deviation is large, retrieval area or sub-domains including plotted sites have several types of surface albedo, that is, heterogeneous surface.

As shown in Figs. 4.5.23 and 4.5.24, for the result at Issyk-Kul, retrieval error is small (< 0.04) and error reduction ratio is large (> 45%) at all day. Further more, AOT difference compared with AERONET AOT is about ±0.025. Issyk-Kul site is positioned at side of Issyk-Kul Lake, which is surrounded by mountains. Therefore, heterogeneity of surface albedo in sub-domains around the lake is high, and standard deviation is also large (~0.1 to 0.2) as shown in Fig. 4.5.25. Furthermore, there is snow on the mountain in the winter, so surface albedo at wavelength 380 and 674nm and its standard deviation are high and large in November. From this case, it is likely that my algorithm works well over inhomogeneous surface albedo region.

On the other hand, as for Banizoumbou site, which is located in Sahara desert, surface albedo shows characteristic surface reflectance of desert, and standard deviation of surface albedo is small (~0.02) compared with other sites as seen in Fig. 4.5.25. This fact shows that surface albedo in sub-domain is nearly homogeneous. At this site, AOT retrieval error is large (~0.1 in November), and error reduction ratio is low (< 20 % in November). From this result, it is likely difficult to retrieve AOT in bright and homogeneous surface area. As another reason, the possibility exists that used aerosol models are not appropriate, because I set urban type aerosol for fine particle and yellow sand for coarse mode aerosol at this analysis. It is pointed out that aerosol model is possible error causes of retrieval error in AOT value (Hernandez et al., 2007).

For the other sites, error reduction ratio varies widely from day to day, but retrieval error is about under 0.06. Surface albedo at sites including urban area looks similar, these areas include vegetation area and standard deviations of surface albedo are about 0.02 to 0.1. Retrieval areas around UMBC and Chiba-Univ. sites include water surface, so variability of surface albedo is larger than other urban area. As for Alta-Floresta site, this site is surrounded by Amazon jangle, and surface albedo illustrates feature of vegetation surface and this area's surface albedo is likely

homogeneous because the variation of surface albedo is small (~0.02). However, in vegetation area, variability of surface albedo between wavelengths is large, and surface albedo of 380 and 674nm in vegetation area is very small (< 0.05 and < 0.1). Therefore, fine and coarse mode of AOT are separately retrieved, and retrieval error is less than 0.05 over Alta-Floresta site. In this site, retrieved AOT is also in agreement with AERONET AOT at difference of ±0.067.

From the result, AOT could be retrieved in an accuracy of less than ±0.06 and showed good agreement with AERONET AOT in vegetation area and heterogeneous surface area including urban, vegetation and water surface, especially in an area where surface albedo covariance is large such as Issyk-Kul site. Ground surface of analysis area including Issyk-Kul site is composed of water surface, vegetation, sand and bare-ground, and also includes ice and snow in winter season.

Therefore, this algorithm is effective in retrieval of aerosol properties such as AOT not only over vegetation area but alto over inhomogeneous surface area, especially the area where surface heterogeneity is large. I will analyze more data and validate retrieved aerosol properties together with surface albedo in the future.

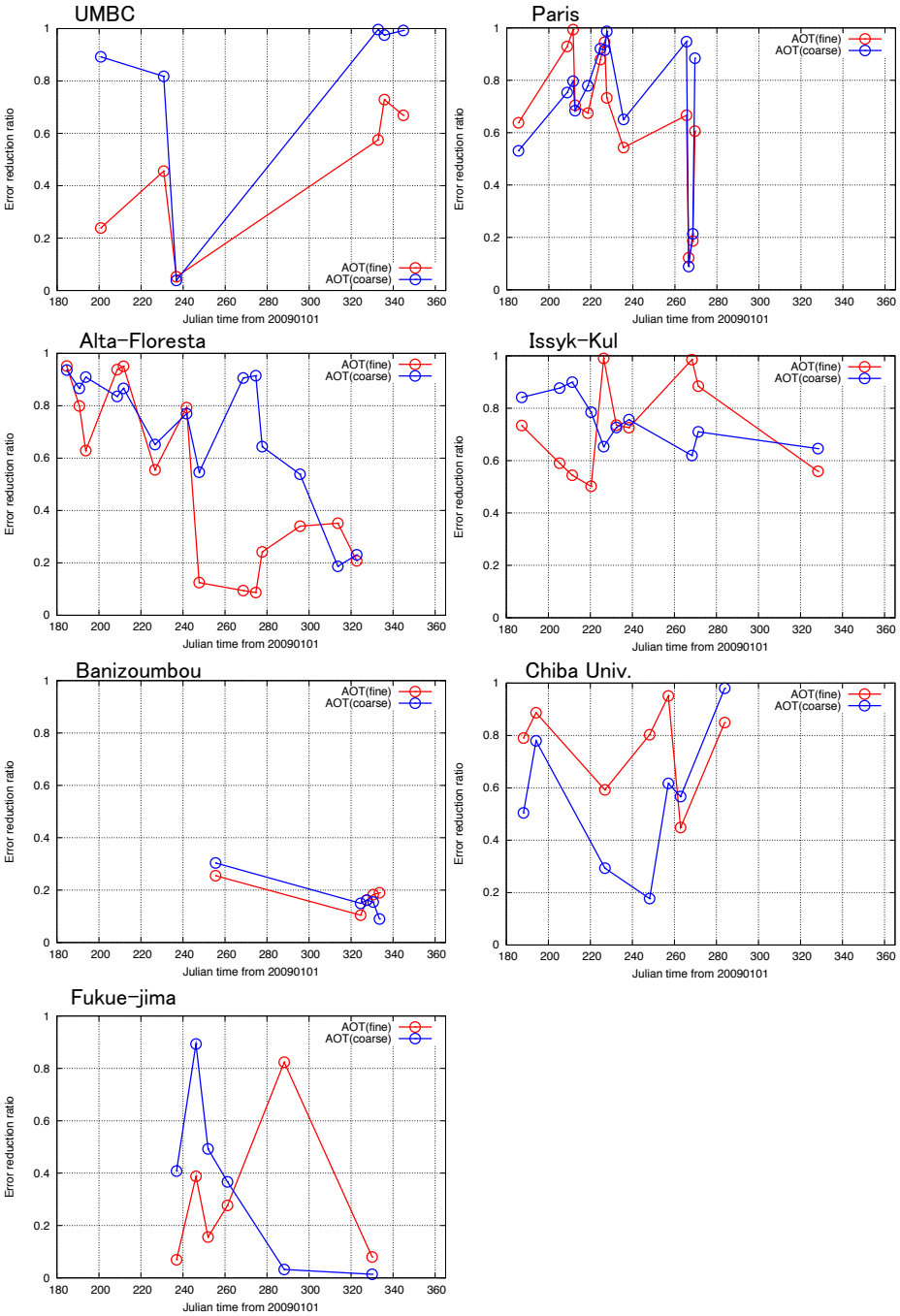

Figure 4.5.24 Time series of error reduction ratio of AOT(fine) (red) and AOT(coarse) (blue) at UMBC, Paris, Alta-Floresta, Issyk-Kul, Banizoumbou, Chiba-univ. and Fukue-jima. X-axis is a day number from January 1, 2009. Error bar in the figure denotes retrieval error calculated by Eq. (4.5.3a).

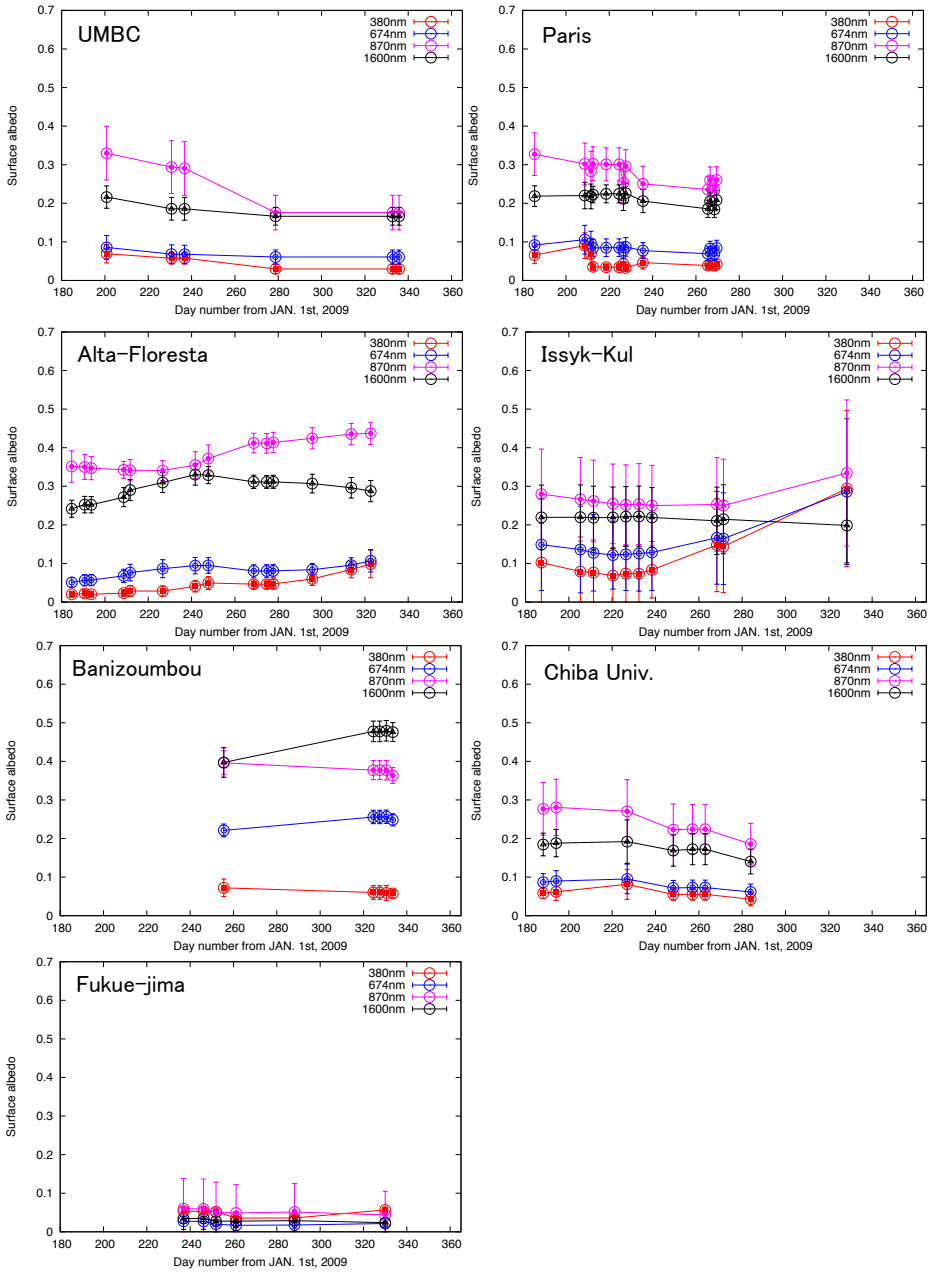

Figure 4.5.25　Time series of surface albedo (corrected minimum reflectance) at wavelengths of 380, 674, 870 and 1600 nm near 10×10 pixels around each site: UMBC, Paris, Alta-Floresta, Issyk-Kul, Banizoumbou, Chiba-Univ. and Fukue-jima. Bar represents the standard deviation of surface albedo. Red is albedo at wavelength of 380nm; blue, 674nm; pink, 870nm; and black, 1600nm.

4.5.6 Discussion

Although AOTs retrieved by this method show an good agreement with ground-based observation such as AERONET and SKYNET except for Saharan desert site, in almost of all cases, there seems to be a same trend that AOT retrieved by the method from GOSAT/TANSO-CAI is underestimated compared with AERONET AOT, especially in large AOT cases. One possible case is vicarious calibration of CAI sensor, because the all cases have a same trend. To investigate the effect of calibration differences in apparent reflectance on AOT values, I have conducted an analysis using the apparent reflectance with some additional values. I tried two experiments: one is to add ±0.02 or ±0.05 to the apparent reflectance, and other is to add ±5% or ±10% of the values of apparent reflectance at all wavelengths. I show the test results in Figure 4.5.26. The figure compares between AERONET AOT and GOSAT/TANSO-CAI AOT by the method at Palaiseou site. Red points denote the result of analysis of default apparent reflectance that already calibrated by Shiomi et al (2010). When apparent reflectance is increased, the retrieved value of AOT(fine) and its slope are increased. On the other hand, AOT(coarse) is decreased when apparent reflectance is increased. SSA is increased when apparent reflectance is decreased, and SSA difference is about 0.01 when the apparent reflectance reduction is 0.05 or 10% of the value. This SSA difference is small compared with AOT difference. From this result, accurate calibration is important to retrieve accurate aerosol parameters.

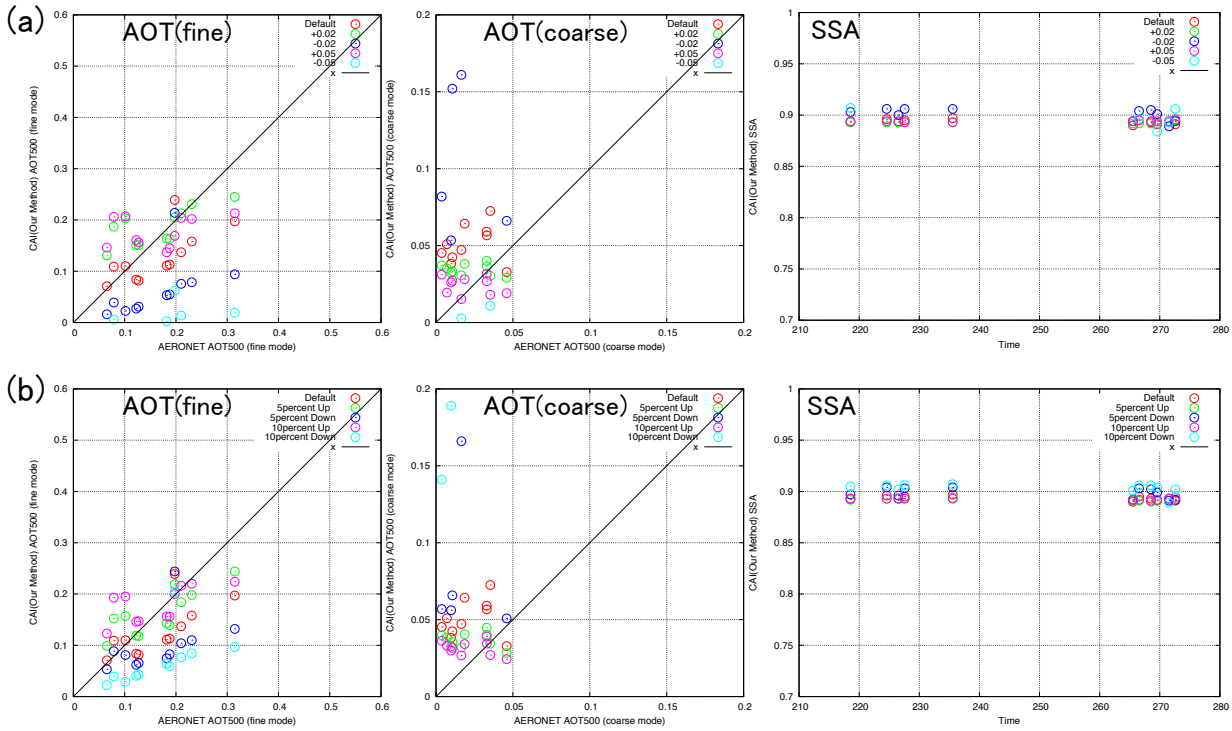

Figure 4.5.26 Test retrieval result of additional correction to observed reflectance and comparison between AERONET AOT and GOSAT/TANSO-CAI AOT by this method at Palaiseou site. (a) I have added ±0(red), +0.02(green), -0.02(blue), +0.05(pink) or -0.05(water blue) to the apparent reflectance at all wavelengths; (b) added ±0(red), +5%(green), -5%(blue), +10%(pink) or -10%(water blue).

In this study, I have focused on the retrieval of aerosol optical properties, such as AOT and SF, over the heterogeneous surface region, especially like urban area. Therefore, I have assumed urban type aerosol model in this analysis. However, I should investigate appropriate aerosol model for each region and change aerosol models for each region. Hernandez et al. (2007 AMS) pointed out that the assumption of aerosol properties, such as the size distribution, single scattering albedo or refractive index, generates substantial errors in AOT (~30%), and that it is required to use an appropriate model of aerosol properties based on measurements to reduce the error in AOT.

In the sections, I compared AOT and SSA derived by this method with that of ground-based observation, AERONET and SKYNET. However, there are few comparison data because of cloud and a large time difference in both observations. I need more analysis to compare with other observation results.

4.6 Analysis with Cloud

One of the features of this algorithm is the direct use of radiation transfer program in the analysis without the use of look up table method (LUT). Therefore, it is easy and possible to retrieve several particle type aerosols simultaneously using a wavelength dependence of aerosol properties. In satellite remote sensing for aerosol, aerosol properties cannot be derived at a place where clouds exist, and the pixels with cloud have been removed by cloud screening process. Simultaneous retrieval of clouds and aerosols has not been challenged. However, in the algorithm clouds can be regarded as white and large size aerosols, and can be incorporated as one of the aerosols into the present algorithm.

I have added a "cloud" aerosol model (Table 4.6.1) and aerosol optical thickness of cloud particle, AOT(cloud) at wavelength 500nm, as a retrieval parameter into analysis. The other aerosol models are same as the models represented in Table 4.4.4. I gave a half of monthly mean values of AOT coarse mode at wavelength of 500nm of AERONET as a priori of AOT(coarse) and AOT(cloud). For AOT(fine), SF and Ag, I gave monthly mean values of AOT fine mode at wavelength of 500nm of AERONET, 0.03, minimum reflectance corrected by Fukuda et al. (2013), respevctively.

Table 4.6.1 Cloud particle model used in analysis. r_m is aerosol mode radius; S is covariance of aerosol volume size distribution (See Eq. (2.3.2)); k_λ is imaginary part of refractive index of each wavelength λ.

	Component	r_m [μm]	S	k_{380}	k_{674}	k_{870}	k_{1600}
Cloud mode	Sea spray	2.04	2.51	5.13E-8	9.86E-8	5.15E-6	6.98E-4

I performed the analysis including a cloud particle property, AOT(cloud), as a retrieval parameter in area of the East coast of the United States (76-77°W/38.7-39.4°N) composed of 64 sub-domains on 4 July, 24 August and 30 August in 2009. As shown in Fig. 4.6.1, which is RGB composite image made from GOSAT/TANCO-CAI band-1, band-2 and band-3, we can see the cloud area (i.e. white area) over the analysis area. I show the analysis result of AOT(fine), AOT(cloud), AOT(coarse), AOT(total), SF, SSA and RMSD of three days in Figs. 4.6.2 to 4.6.4. As shown in the figures, AOT(cloud) can be produced in the same area as Fig. 4.6.1. In other parameters, the spatial distribution can be obtained. SSA values at wavelength 674nm in the cloud-detected area are close to 1.0, and it is a reasonable result because cloud does not absorb the sunlight or light at wavelength of 674nm as much. RMSD values at almost of all pixels are within

0.1 (10%), and it means the calculations are converged. In those days, there are no retrieval data from AERONET, because AERONET cloud screening routine detected clouds in this case and does not retrieve aerosol parameter in cloudy condition.

Although I need to validate the result, it is possible to detect clouds and aerosols simultaneously by this algorithm from the results. To my knowledge, there are no past studies of simultaneous retrieval of clouds and aerosols by one algorithm. If clouds and aerosols are retrieved simultaneously, we are able to use retrieved cloud information to cloud screening at the same time as aerosol retrievals.

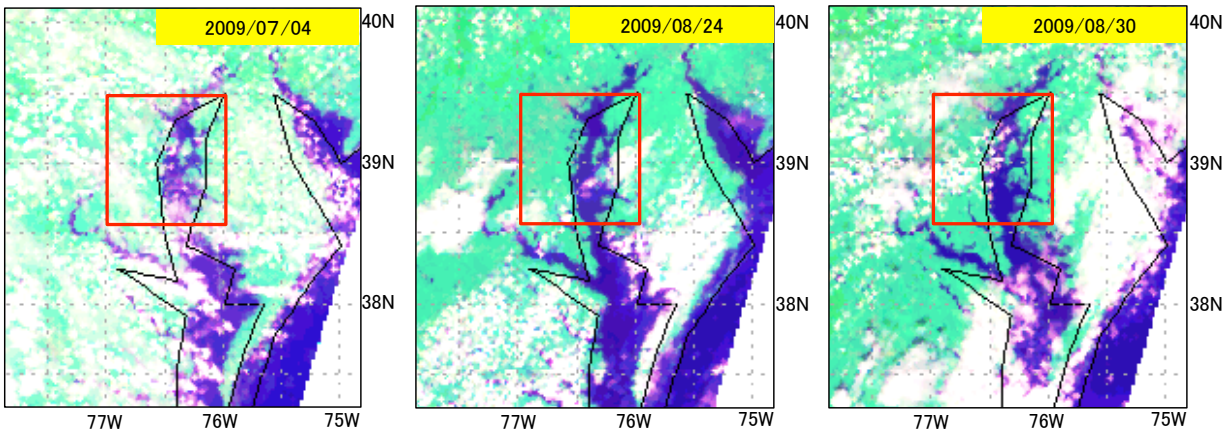

Figure 4.6.1 RGB composite image made from GOSAT/TANCO-CAI band1, band2 and band3, we can see the cloud area (i.e. white area) over the analysis region (Red squire : 76-77°W/38.7-39.4°N) on July 4, August 24, August 30 in 2009.

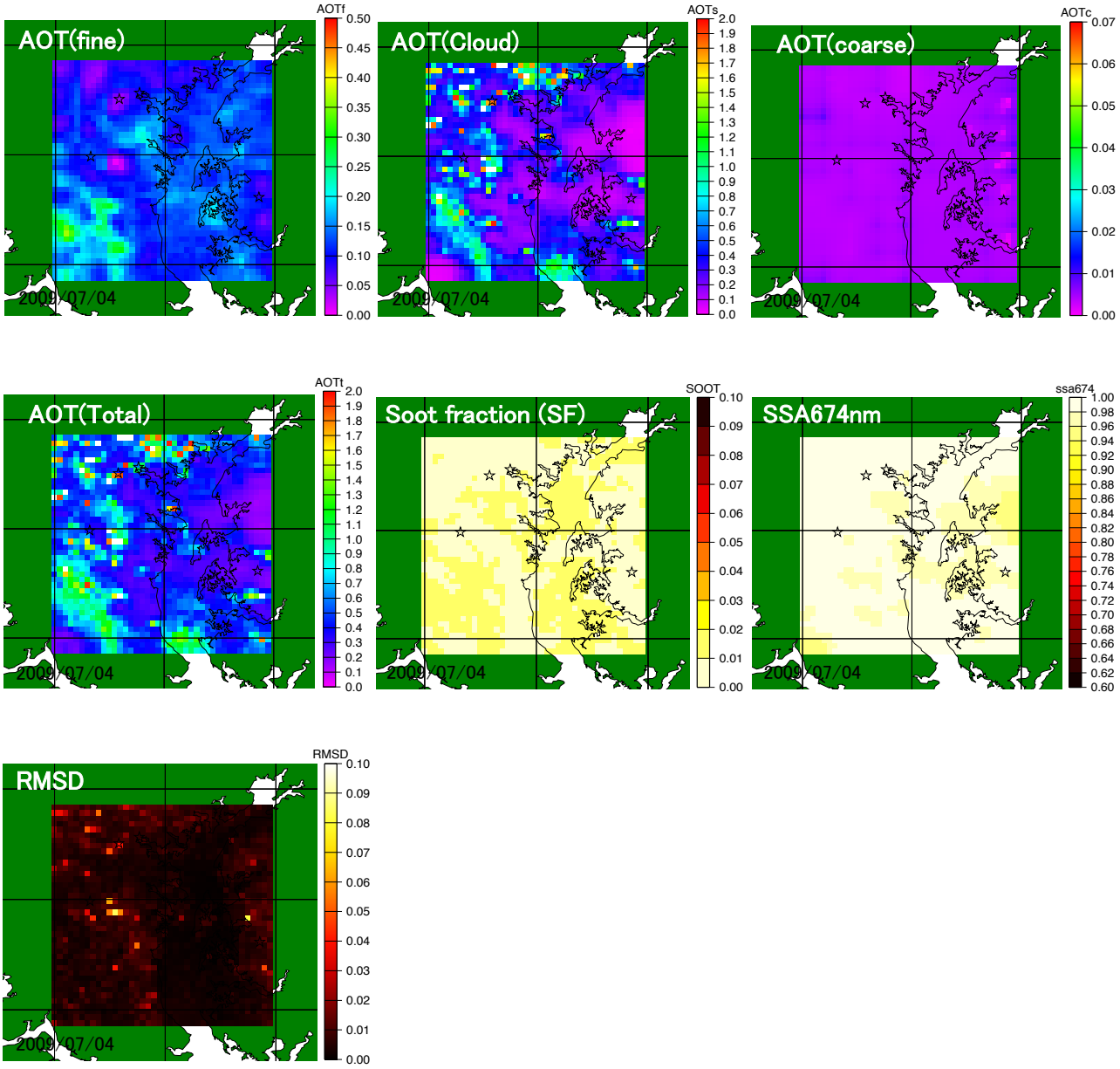

Figure 4.6.2 Retrieval result including cloud particle model: AOT(fine), AOT(cloud), AOT(coarse), AOT(total) at wavelength of 500nm, SF, SSA at wavelength of 674nm, RMSD on July 4, 2009. The analysis region is 76-77°W/38.7-39.4°N.

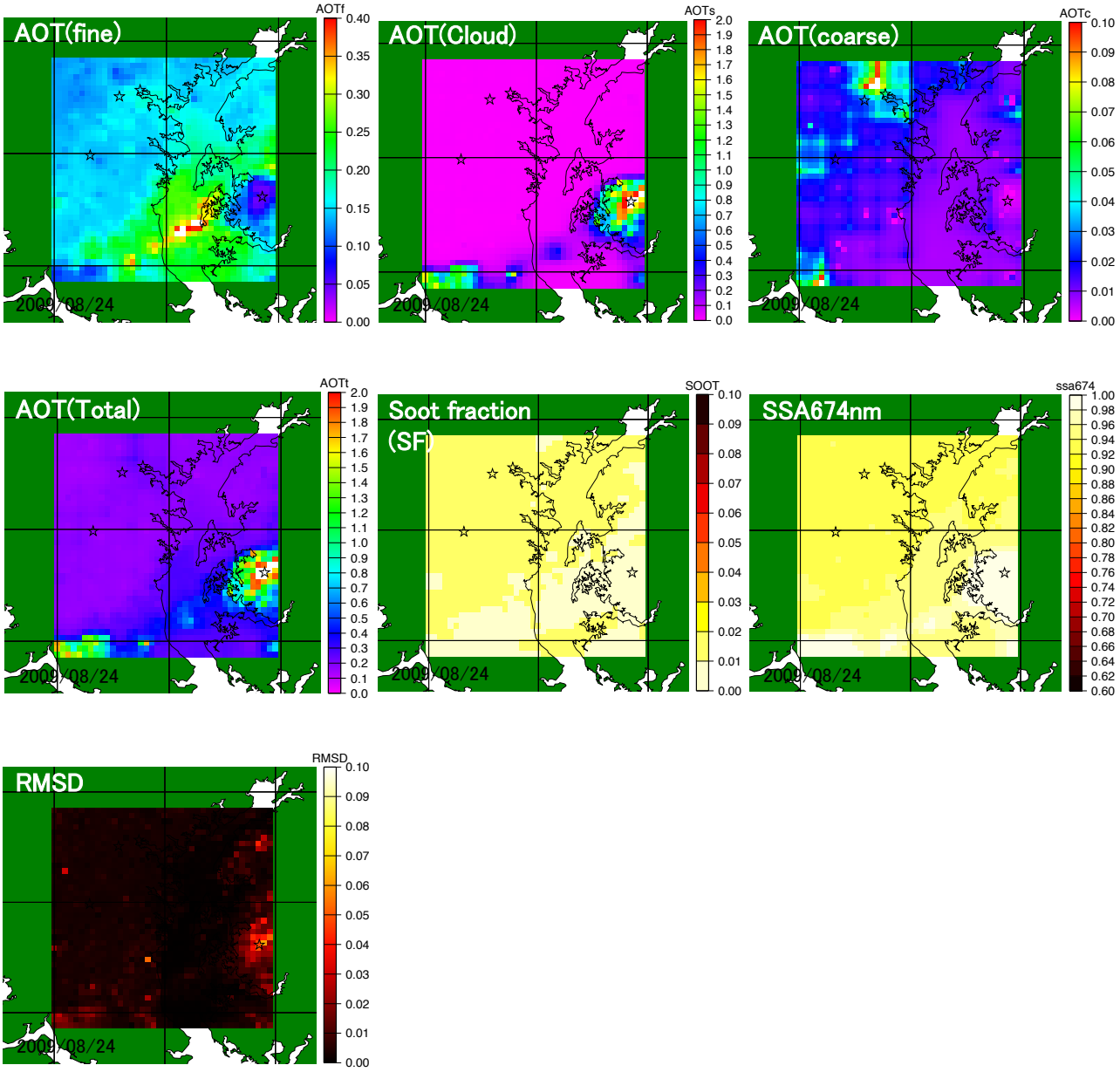

Figure 4.6.3 Same as in Fig. 4.6.2, but on August 24, 2009.

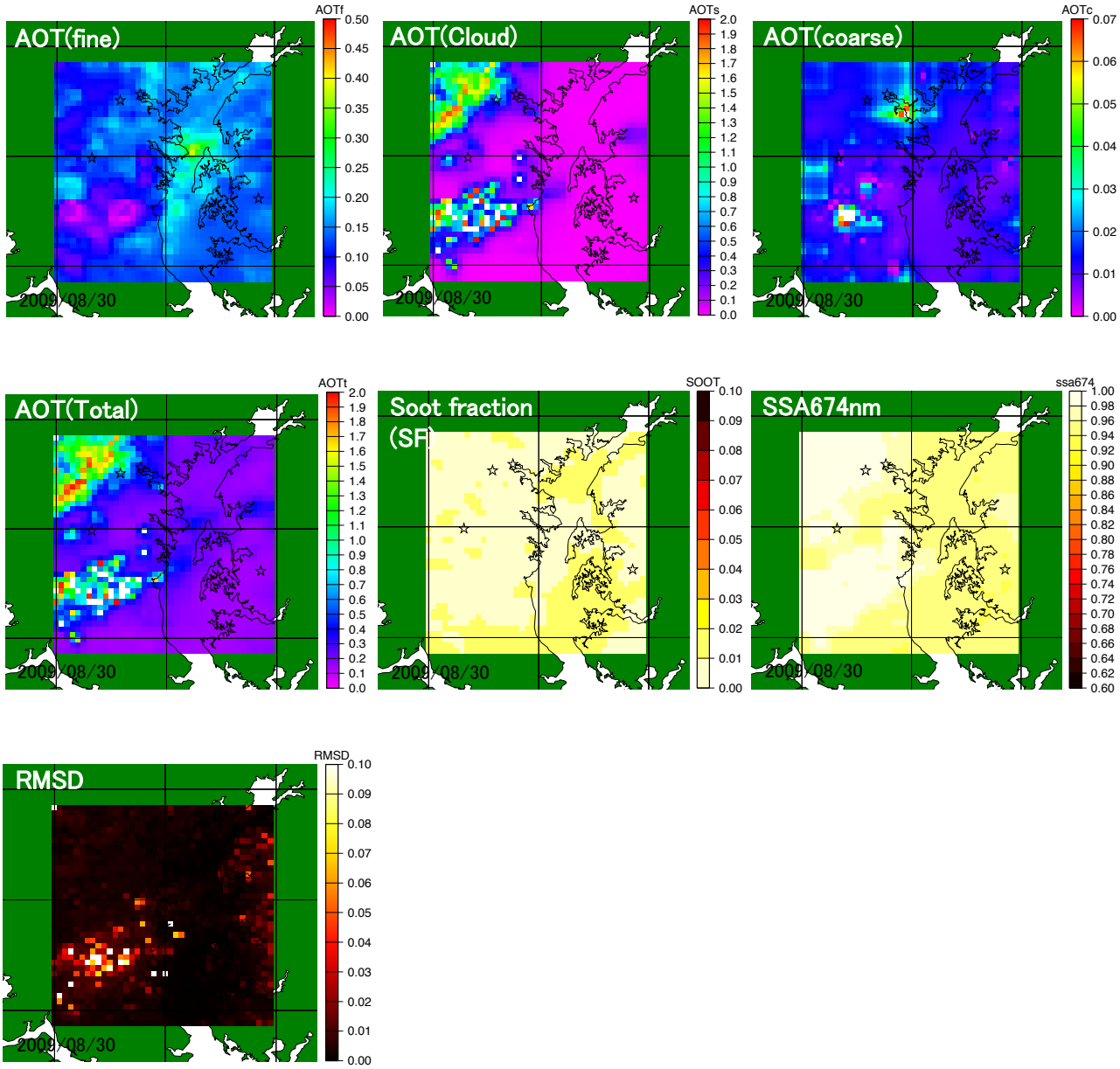

Figure 4.6.4 Same as in Fig. 4.6.2, but on August 30, 2009.

4.7 Summary

In this chapter, I have shown the analysis results using GOSAT/TANSO-CAI imager data by my developed algorithm. An important point of this study is to develop an algorithm to retrieve aerosol properties, such as AOT and SF, in the heterogeneous surface area with bright and dark reflectance like urban area.

I have compared AOT retrieved by this method with AOT obtained by ground-based observation at the closest pixel. In a comparison at several sites in urban area, AOT retrieved by the method are in good agreement with AERONET AOT. As for absorption parameter of aerosol, SSA values are calculated by retrieved AOT and soot fraction (SF) and show a similar tendency of AERONET SSA and BC concentration of in situ measurement (Song et al., 2013) in summer and winter at Beijing. However, validation data is few because ground-based network AERONET have derived SSA when AOT440 > 0.4, and more analyses are necessary to validate column SSA or SF.

In past studies, it has been difficult to retrieve AOT and obtain spatial distribution of AOT over inhomogeneous surface area including bright and dark surfaces (Hernandez et al., 2007; Fukuda, 2010). On the other hand, in the comparison between AERONET and the closest GOSAT-CAI pixel, retrieved AOT in this study is in agreement with AERONET AOT, and AOT error is about 0.066. Moreover, this method was able to obtain the smooth horizontal distribution of AOT. From the results, it has become possible to retrieve aerosol properties AOT in urban area by my developed algorithm.

With respect to AOT in area other than urban area, retrieved AOT in vegetation, lakeside and seaside show an agreement with AOT derived by ground-based observation, AERONET or SKYNET, while AOT at a site in Saharan desert region is not in good agreement with AETONET AOT. Yoshida et al. (2013), which is an expansion of Kaufman neutral method (Kaufman et al., 1987, 2001), has retrieved AOT and SSA in desert region, using temporal information of surface albedo and absorption. I will try to include such information of time dimension to this algorithm in future.

In this study I have focused on urban aerosol retrieval, assuming urban type aerosol model. However, an aerosol model assumption affects accuracy of retrieval AOT and SSA (Hernandez et al., 2007). I need to investigate retrieval differences in retrieval aerosol parameters, such as AOT and SF, arising from aerosol model assumption, applying more suitable aerosol model to each region. Furthermore, calibration of observation data, surface albedo given as a priori and relative humidity are also possible cases for the accuracy of aerosol parameter retrievals. I should apply an accurate value of calibration constant, a priori of surface albedo and relative humidity.

One of features of this algorithm is direct use of radiation transfer code without using LUT.

Therefore, I can easily add or change aerosol model. In this chapter, I have tried simultaneous retrieval of clouds and aerosols, which has not been done in the past. AOT of cloud particles was detected from GOSAT/TANSO-CAI imager data in the same area of RGB composite images. I will investigate more cases and validate the result using lidar or other data.

Chapter 5 General conclusion

5.1 Conclusion

In the present study, I have developed an aerosol remote sensing algorithm using multi-wavelength and multi-pixel information. Using the algorithm, fine and coarse mode aerosol optical thicknesses, volume soot fraction in fine mode particles (SF) and ground surface albedo of each observed wavelength can be retrieved simultaneously over a heterogeneous surface area as well as homogeneous area. Furthermore, I incorporated directly a radiation transfer calculation (RSTAT) into this inversion algorithm without using LUT, which is used by almost of all aerosol satellite remote sensing of imager data. Although a large computational time is required to calculation, the direct use of radiation transfer calculation has following merits: I can retrieve several types of aerosol particles at once; more accurate radiation transfer calculation becomes possible by calculation with realistic atmospheric conditions and multiple scattering process. It is possible to retrieve AOT(fine), AOT(coarse) and SF at the same time by the multi-wavelength and multi-pixel method using the information of different reflectances of surfaces and wavelength dependences of each parameter.

By this developed algorithm, it has become possible to retrieve AOT and an absorption parameter SF in urban area, where the estimation had been difficult in the past. Furthermore, the horizontal distribution of aerosol properties can become obtained over heterogeneous surface region including dark and bright surface like urban area.

The retrieval error of AOT is about ±0.066 over urban region from the comparison of AOT between AERONET and the closest TANSO-CAI pixel with this method. Those values seem to be better than the current AOT retrieval accuracy in land area by satellite remote sensing, ±0.05±0.2AOT or 5~30% (Kaufman et al., 2002; Chu et al., 2003; Lee et al., 2009).

From the results, I can expect to get a grasp of aerosol properties in urban area where is an emission source of air pollution (anthropogenic) aerosols that includes small and light-absorbing substances and that affects the earth's atmosphere. Then, contribution to the atmosphere and aerosol studies can be expected.

I incorporated radiation transfer model into this inversion algorithm without using LUT, and then we are able to set or specify several wavelengths that I would like to use and retrieval aerosol models. For example, I have tried to add cloud particles in an analysis, and I have been able to retrieve AOTs of cloud and aerosol particles simultaneously and detect cloud AOT and high SSA at wavelength of 674nm in cloud area. From this result, simultaneous cloud screening will become

possible in the future. Furthermore, application of this algorithm to other satellite data is probably easy by the direct use of radiation transfer model compared with LUT method. Therefore, I have been able to develop a versatile algorithm of aerosol remote sensing.

5.2 Future work

In this study, I analyzed GOSAT/TANNSO-CAI imager data of a half year. I will analyze and validate more data including urban area. I will also apply to other satellite data, such as ADEOS-II/GLI and MODIS.

Computation time is mentioned as a problem. This method with radiation model takes a large computaional time compared with LUT method. To derive global aerosol properties, I need to speed up calculation efficiency of the algorithm, so I will use speed-up techniques, such as neural-network or adjoint technique.

In the future, several new satellites will be launched (GOSAT2/TANSO-CAI2, GCOM-C1/SGLI and HIMAWARI 8 and 9), so that I will incorporate multi-angle and detailed polarization, and then will apply the algorithm to new satellites to be launched in the future.

Appendix I

Polarization Correction

I made a polarization correction (Ogawa, Tanaka and Nakajima, 1989) to RSTAR. A polarization correction is as follows,

$$L(\mu,\mu_0;\phi-\phi_0;\tau,\tau_0) = L_{scalar}(\mu,\mu_0;\phi-\phi_0;\tau,\tau_0) + \Delta L(\mu,\mu_0;\phi-\phi_0;\tau,\tau_0), \quad \text{(I-1)}$$

$$\Delta L(\mu,\mu_0;\phi-\phi_0;\tau,\tau_0) = \sum_{m=0}^{M} \Delta L^m(\mu,\mu_0;\tau,\tau_0)\cos m(\phi-\phi_0), \quad \text{(I-2)}$$

where L is corrected radiance; L_{scalar}, scalar radiance calculated by RSTAR, and not including polarization; ΔL, additional sky radiance; F_0, solar radiation; τ_0, a plane-parallel homogeneous atmosphere of optical thickness illustrated by solar radiation propagating toward (μ_0, φ_0); τ, the optical thickness of the observer's position of top of atmosphere; τ_m and τ_a, the optical thickness of molecular atmosphere and aerosol, respectively; ω_m and ω_a, the single scattering albedo of molecules and aerosol, respectively; ρ, depolarization factor of molecular scattering; β_2, truncation factor of phase function. The other parameters are as follos,

I compared values of apparent reflectance $R = (\pi L)/\mu_0 F_0$ calculated by RSTAR with polarization correction and by PSTAR, which is a land-ocean radiation transfer model including polarization (Ota *et al*., 2010) under following conditions: ground surface albedo, 0.05, 0.5, 0.9; Solar zenith angle, θ_0, 0 ~ 70 degree; Satellite zenith angle, θ, 110 ~ 180 degree; Satellite azimuth angle, φ, 0 ~ 180 degree; Aerosol optical thickness, τ, 0.0.

Figure I-1 to I-9 show percentage differences of apparent reflectance between RSTAR and PSTAR, and x-axis and y-axis are satellite azimuth angle and satellite zenith angle, respectively. The result shows that the difference between RSTAR and PSTAR became smaller than the difference before, and the difference was within 2% in solar zenith angle from 0 degree to 60 degree.

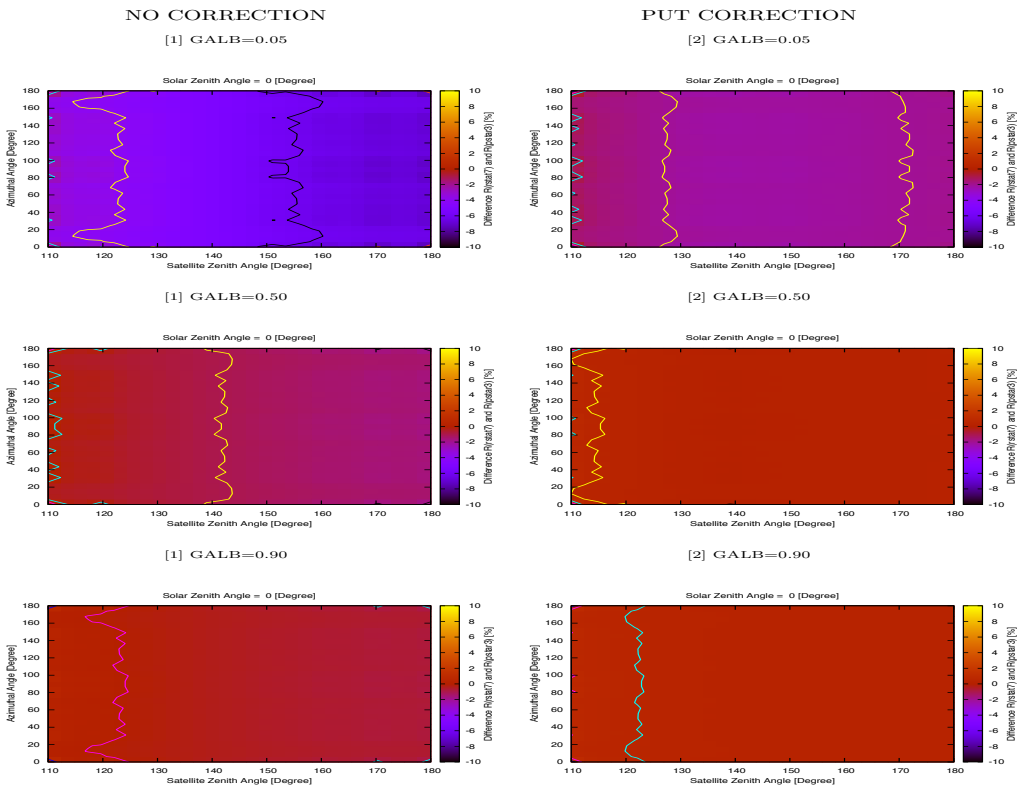

Figure I-1. Percentage difference of apparent reflectance between RSTAR and PSTAR before (left) and after (rigth) polarization correction. X-axis and Y-axis are satellite azimuth angle and satellite zenith angle, respectively. Top panel is the case that surface albedo (GALB) is 0.05; middle, GALB=0.5; bottom, GALB=0.90. In the case of solar zenith angle (θ_0) is 0 degree.

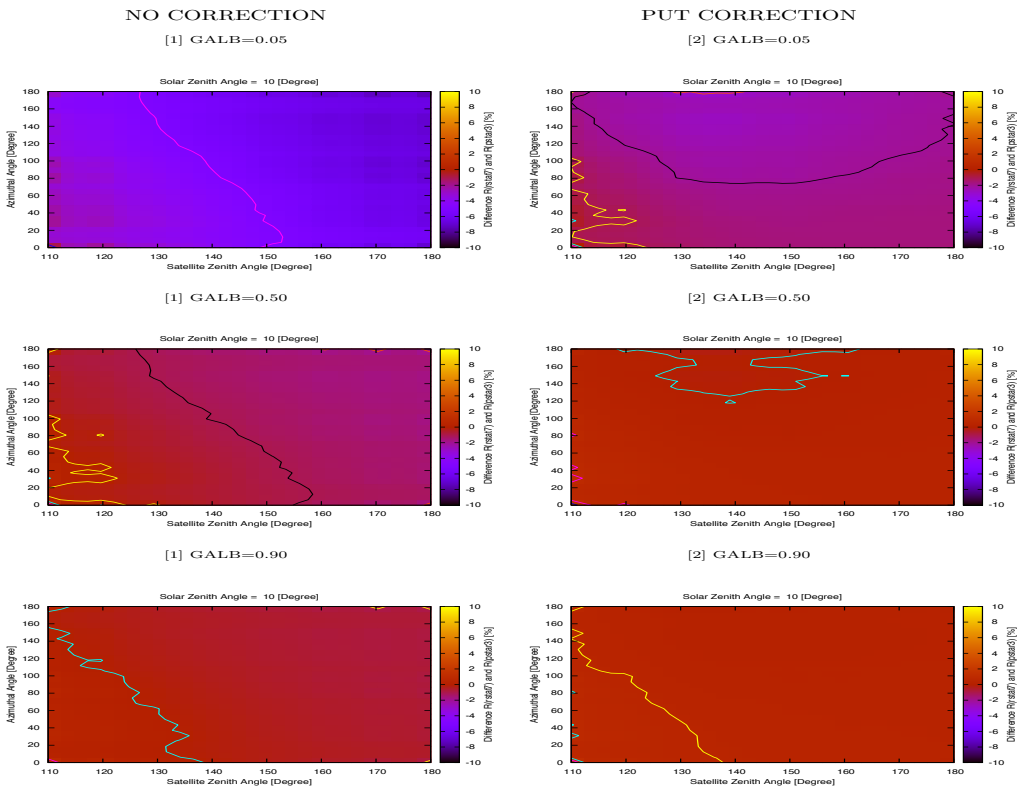

Figure I-2. Same as in Fig. I-1, but solar zenith angle is 10 degree.

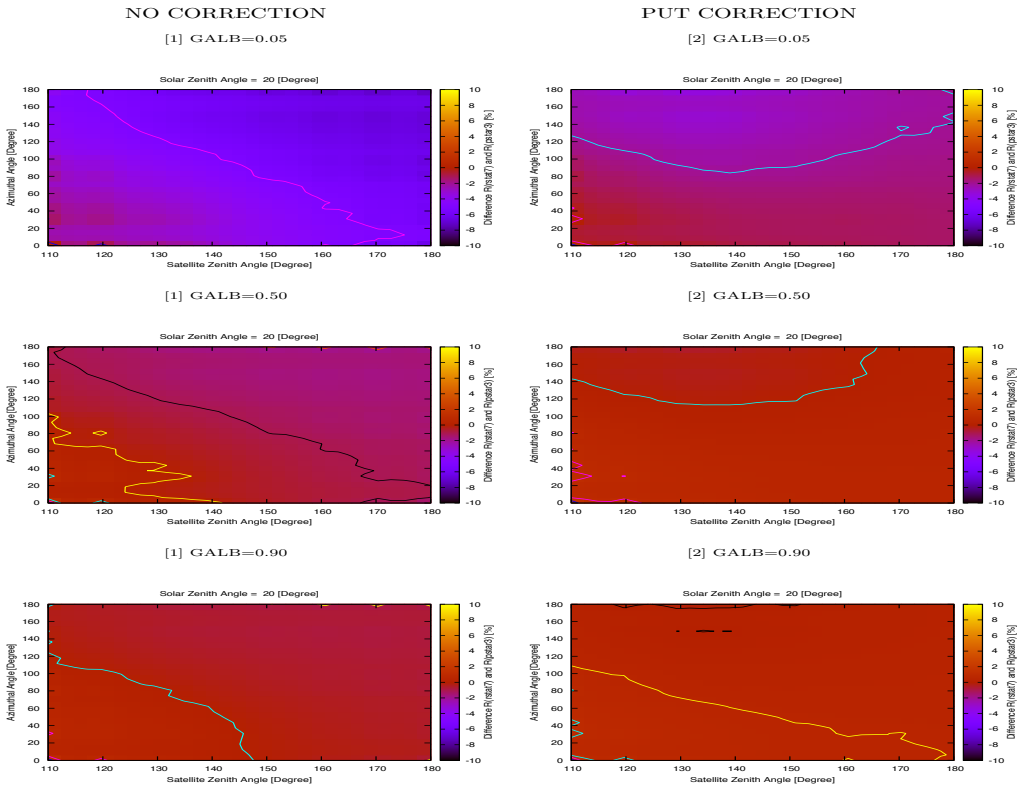

Figure I-3. Same as in Fig. I-1, but solar zenith angle is 20 degree.

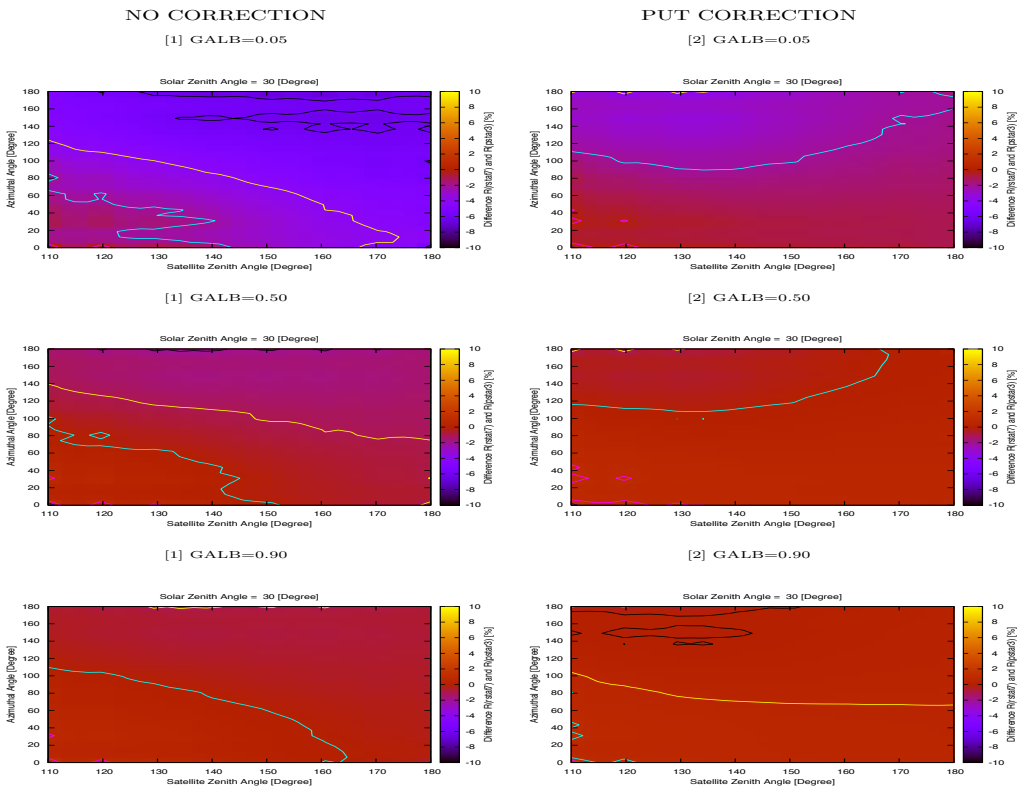

Figure I-4. Same as Figure I-1, but solar zenith angle is 30 degree.

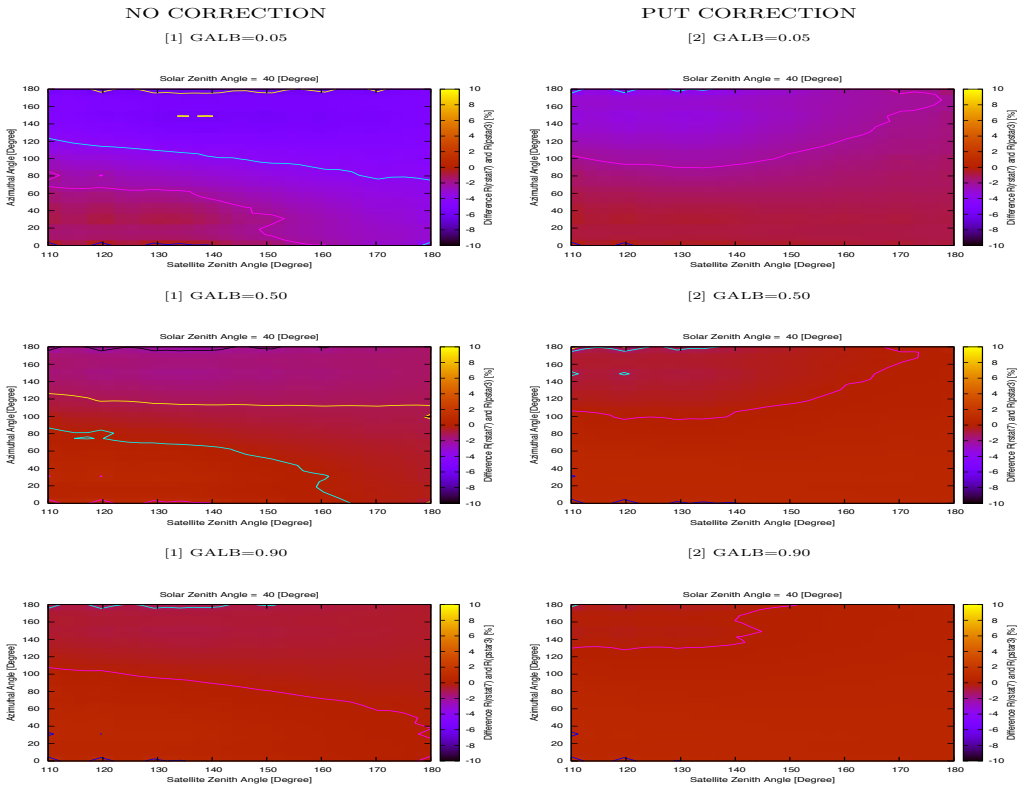

Figure I-5. Same as in Fig. I-1, but solar zenith angle is 40 degree.

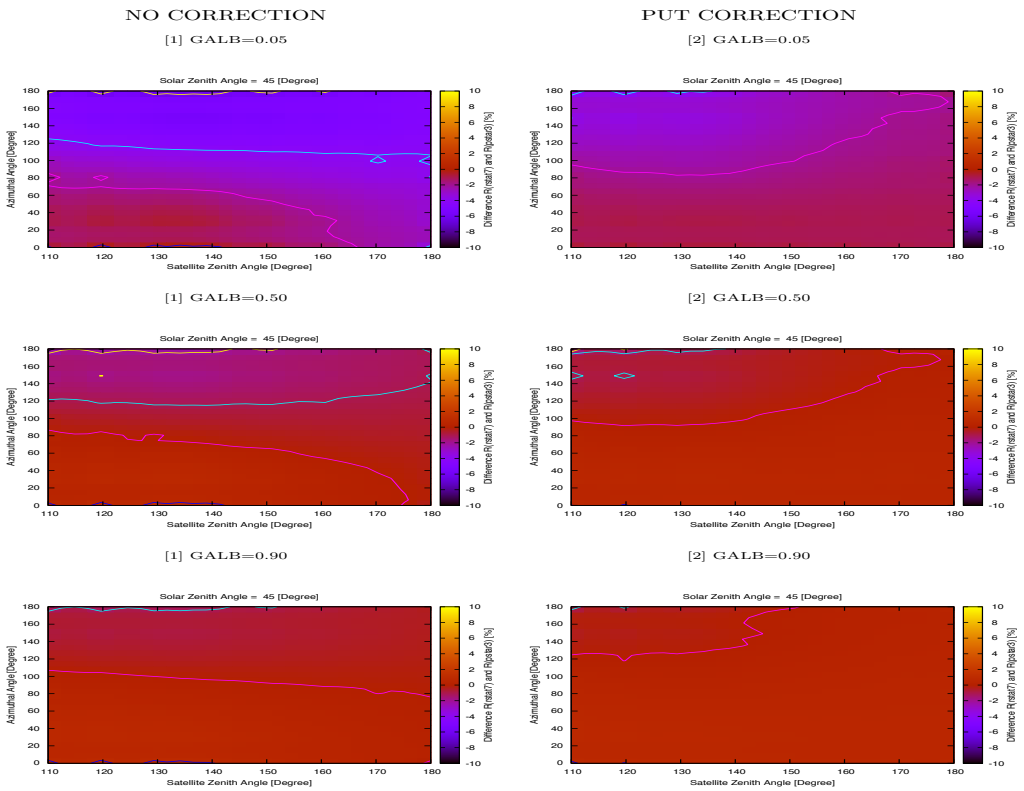

Figure I-6. Same as in Fig. I-1, but solar zenith angle is 45 degree.

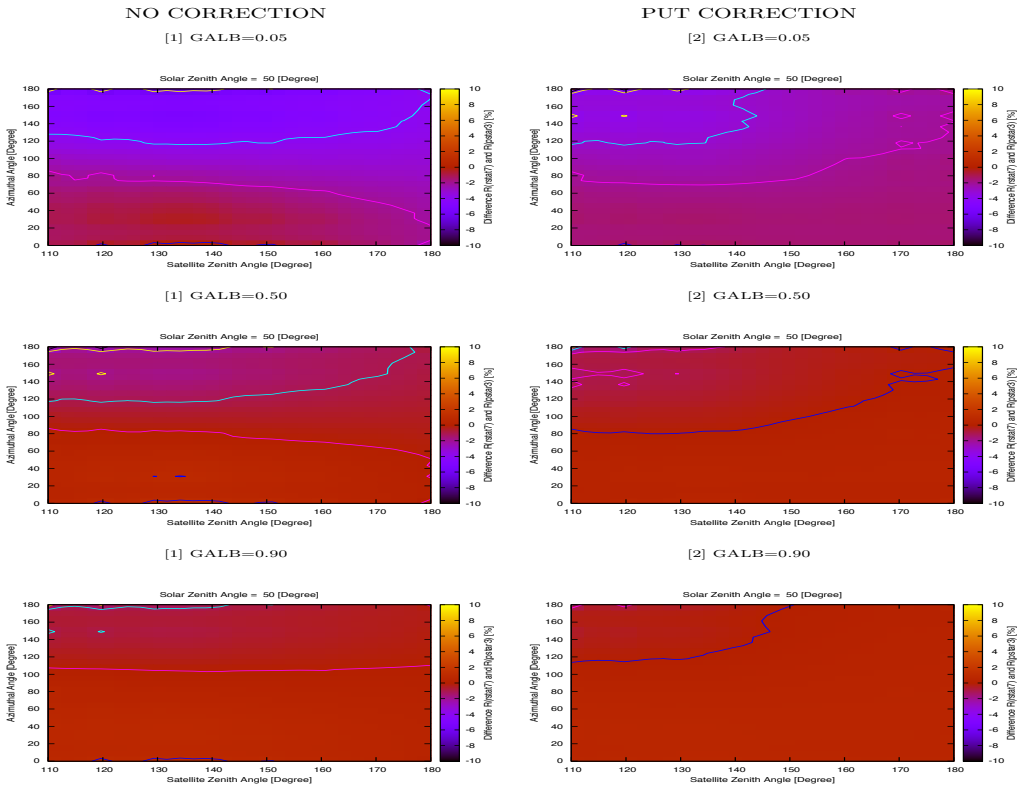

Figure I-7. Same as in Fig. I-1, but solar zenith angle is 50 degree.

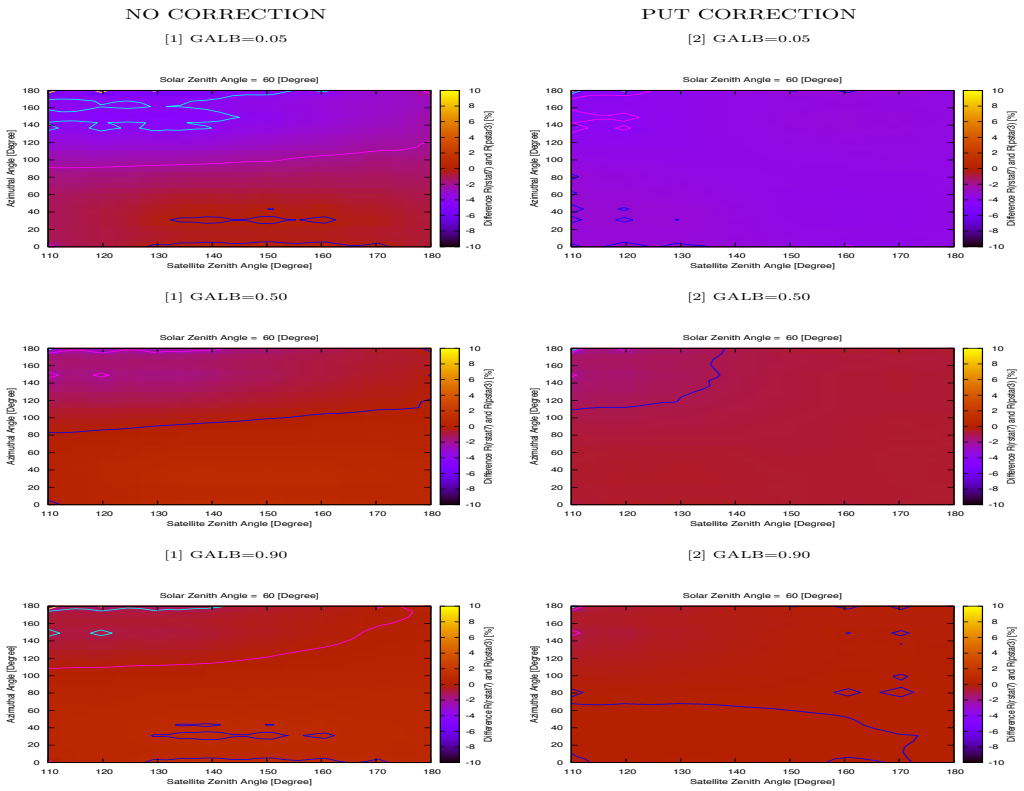

Figure I-8. Same as in Fig. I-1, but solar zenith angle is 60 degree.

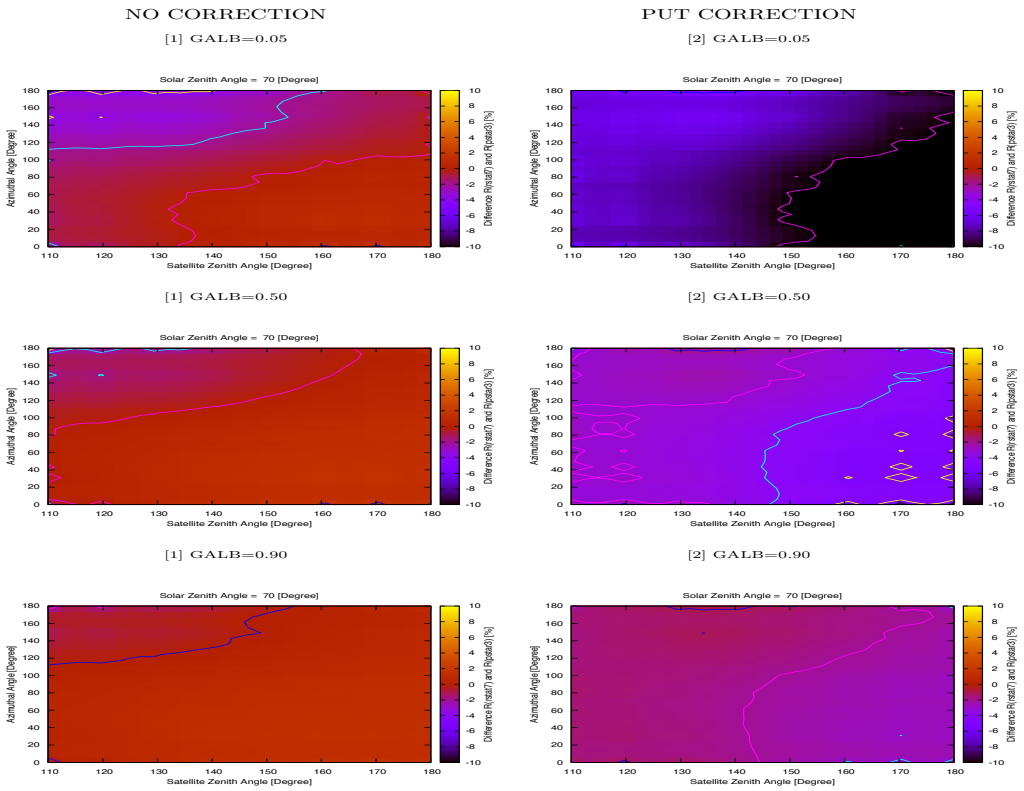

Figure I-9. Same as in Fig. I-1, but solar zenith angle is 70 degree.

References

Ahmad, Z., and Fraser, R. S., 1982: An iterative radiative transfer code for ocean-atmosphere systems. *Journal of the Atmospheric Sciences*, **39**(3), 656-665.

Chen, W. T., Nenes, A., Liao, H., Adams, P. J., Li, J. L. F., & Seinfeld, J. H., 2010. Global climate response to anthropogenic aerosol indirect effects: Present day and year 2100. *Journal of Geophysical Research: Atmospheres (1984–2012)*, **115**(D12).

Chu, D. A., Kaufman, Y. J., Ichoku, C., Remer, L. A., Tanré, D., & Holben, B. N. (2002). Validation of MODIS aerosol optical depth retrieval over land. *Geophysical Research Letters*, **29**(12), MOD2-1.

Chu, D. A., Kaufman, Y. J., Zibordi, G., Chern, J. D., Mao, J., Li, C., and Holben, B. N., 2003: Global monitoring of air pollution over land from the Earth Observing System‐Terra Moderate Resolution Imaging Spectroradiometer (MODIS). *Journal of Geophysical Research: Atmospheres (1984–2012)*, **108**(D21).

Cox, C., and Munk, W., 1954: Measurement of the roughness of the sea surface from photographs of the sun's glitter. *JOSA*, **44**(11), 838-850.

Cox, C., and Munk, W., 1956: Slopes of the sea surface deduced from photographs of sun glitter. *Scripps Institution of Oceanography*.

Dubovik O., and M. D. King, 2000: A flexible inversion algorithm for retrieval of aerosol optical properties from Sun and sky radianve measurements, *J. Geophys. Res.*, **105**, No. D16, 20673-20696.

Dubovik, O., B. N. Holben, T. F. Eck, A. Smirnov, Y. J. Kaufman, M. D. King, D. Tanré, I. Slutsker 2002: Variability of absorption and optical properties of key aerosol types observed in worldwide locations. *J. Atmos. Sci.,* **59,** 590-608.

Dubovik, O., Holben, B. N., Lapyonok, T., Sinyuk, A., Mishchenko, M. I., Yang, P., and Slutsker, I., 2002: Non‐spherical aerosol retrieval method employing light scattering by spheroids. *Geophysical Research Letters*, **29**(10), 54-1.

Dubovik, O., Herman, M., Holdak, A., Lapyonok, T., Tanré, D., Deuzé, J. L., Ducos, F., Sinyuk, A., and Lopatin, A. 2011: Statistically optimized inversion algorithm for enhanced retrieval of aerosol properties from spectral multi-angle polarimetric satellite observations. *Meas. Tech*, **4**, 975-1018.

Fukuda, S., Nakajima, T., Takenaka, H., Higurashi, A., Kikuchi, N., Nakajima, T. Y., & Ishida, H., 2013: New approaches to removing cloud shadows and evaluating the 380 nm surface

reflectance for improved aerosol optical thickness retrievals from the GOSAT/TANSO‐Cloud and Aerosol Imager. *Journal of Geophysical Research: Atmospheres*, **118**(24), 13-520.

Hashimoto, M.; Nakajima, T.; Dubovik, O.; Campanelli, M.; Che, H.; Khatri, P.; Takamura, T.; Pandithurai, G., 2012: Development of a new data-processing method for SKYNET sky radiometer observations. Atmos. Meas. Tech., **5**, 2723–2737, doi:10.5194/amt-5-2723-2012.

Herman, J. R., Bhartia, P. K., Torres, O., Hsu, C., Seftor, C., and Celarier, E., 1997: Global distribution of UV‐absorbing aerosols from Nimbus 7/TOMS data. *Journal of Geophysical Research: Atmospheres (1984–2012)*, **102**(D14), 16911-16922.

Hess, M., P. Koepke, and I. Suhult,, 1998: Optical Properties of Aerosols and Clouds: The Software Package OPAC. *Bull. Amer. Meteor. Soc*., **79**, 5, 831-844.

Hernandez, E., Oo, M. M., Charles, L., Gross, B., Mihailidi, M., & Moshary, F., 2007: Assessing the land albedo model of the new MODIS Aerosol retrieval over land Algorithm for urban scenes. In *11th Symposium on Integrated Observing and Assimilation Systems for the Atmosphere, Oceans, and Land Surface*.

Higurashi, A., and T. Nakajima, 1999: Development of a two-channel aerosol retrieval algorithm on a global scale using NOAA AVHRR, *J. Atmos. Sci.,* **56,** 924-941.

Higurashi, A. and T. Nakajima, 2002: Detection of aerosol types over the East China Sea near Japan from four-channel satellite data, *Geopys. Res. Lett.,* **29**(17)**,** 1836, doi:10.1029/2002GL015357.

Höller, R., Higurashi, A., and Nakajima, T., 2004: The GLI 380-nm channel–Application for satellite remote sensing of tropospheric aerosol. In *Proc. EUMETSAT Meteorological Satellite Conference*.

Holben, B. N., T. F. Eck, I. Slutsker, D. Tanre, J. P. Buis, A. Setzer, E. Vermote, J. A. Reagan, Y. J. Kaufman, T. Nakajima, F. Lavenu, I. Jankowiak, and A. Smirnov, 1998: AERONET—A federated instrument network and data archive for aerosol characterization, *Remote Sens. Environ.,* **66,** 1– 16.

Holben, B, T. Eck, J. Schafer, D. Giles, M. Sorokin: Distributed Regional Aerosol Gridded Observation Networks (DRAGON) White Paper (http://aeronet.gsfc.nasa.gov/new_web/DRAGON-USA_2011_DC_Maryland.html)

Hsu, N. C., S.-C. Tsay, M. D. King, and J. R. Herman, 2004: Aerosol properties over bright-reflecting source regions, *IEEE Trans. Geosco. Remote Sens.,* **42,** 557-569.

Hsu, N. C., S.-C. Tsay, M. D. King, and J. R. Herman, 2006: Deep blue retrievals of Asian aerosol properties during ACE-Asia, *IEEE Trans. Geosco. Remote Sens.,* **44,** 3180-3195.

Ishida, H., and T. Y. Nakajima, 2009: Development of an unbiased cloud detection algorithm for a

spaceborne multispectral imager *J. Geophys. Res.,* **114,** D07206, doi:10.1029/2008JD010710

Ishimoto, H., Zaizen, Y., Uchiyama, A., Masuda, K., and Mano, Y., 2010: Shape modeling of mineral dust particles for light-scattering calculations using the spatial Poisson–Voronoi tessellation. *Journal of Quantitative Spectroscopy and Radiative Transfer*, **111**(16), 2434-2443.

IPCC AR4 (Intergovernmental Panel on Climate Change), (2007), Climate Change 2007: The Physical Science Basis, Contribution of Working Group I to the Fourth Assessment Report of the Intergovernmental Panel on Climate Change, Solomon, S., Qin, D., Manning, M., Chen, Z., Marquis, M., Averyt, K. B., Tignor, M., and H. L. Miller, eds., p.996, Cambridge Univ. Press, Cambridge, United Kingdom and New York, NY, USA.

IPCC AR5 (Intergovernmental Panel on Climate Change), (2013), Climate Change 2013: The Physical Science Basis, Contribution of Working Group I to the Fifth Assessment Report of the Intergovernmental Panel on Climate Change, Cambridge Univ. Press, Cambridge, United Kingdom and New York, NY, USA.

Kahn, R. A., Gaitley, B. J., Martonchik, J. V., Diner, D. J., Crean, K. A., & Holben, B., 2005: Multiangle Imaging Spectroradiometer (MISR) global aerosol optical depth validation based on 2 years of coincident Aerosol Robotic Network (AERONET) observations. *Journal of Geophysical Research: Atmospheres (1984–2012)*, **110**(D10).

Kaufman, Y. J., 1987: Satellite sensing of aerosol absorption. *Journal of Geophysical Research: Atmospheres (1984–2012)*, **92**(D4), 4307-4317.

Kaufman, Y. J., Tanré, D., Remer, L. A., Vermote, E. F., Chu, A., & Holben, B. N., 1997: Operational remote sensing of tropospheric aerosol over land from EOS moderate resolution imaging spectroradiometer. *Journal of Geophysical Research: Atmospheres (1984–2012)*, **102**(D14), 17051-17067.

Kaufman, Y. J., Tanré, D., Dubovik, O., Karnieli, A., & Remer, L. A., 2001: Absorption of sunlight by dust as inferred from satellite and ground‐based remote sensing. *Geophysical Research Letters*, **28**(8), 1479-1482.

Kaufman, Y. J., Tanré, D., & Boucher, O., 2002: A satellite view of aerosols in the climate system. *Nature*, *419*(6903), 215-223.

Kawamura, K., 1999: 有機エアロゾルの組成・分布・生成. *気象研究ノート*, **218**, 11-28.

Khatri, P., and Takamura, T., 2009: An Algorithm to Screen Cloud-Affected Data for Sky Radiometer Data Analysis. *気象集誌. 第 2 輯*, **87**(1), 189-204.

Lee, K. H., Li, Z., Kim, Y. J., & Kokhanovsky, A., 2009: Atmospheric aerosol monitoring from satellite observations: a history of three decades. In *Atmospheric and biological environmental monitoring* (pp. 13-38). Springer Netherlands.

Leroy, M., Deuze, J. L., Bréon, F. M., Hautecoeur, O., Herman, M., Buriez, J. C., Tanré, D, Bouffiès, S., Chazette, P., and Roujean, J. L., 1997: Retrieval of atmospheric properties and surface bidirectional reflectances over land from POLDER/ADEOS. *Journal of Geophysical Research: Atmospheres (1984–2012)*, **102**(D14), 17023-17037.

Levy, R. C., Remer, L. A., Tanré, D., Kaufman, Y. J., Ichoku, C., Holben, B. N., Livingston, J. M., Russell, P. B., and Maring, H., 2003: Evaluation of the Moderate‐Resolution Imaging Spectroradiometer (MODIS) retrievals of dust aerosol over the ocean during PRIDE. *Journal of Geophysical Research: Atmospheres (1984–2012)*, **108**(D19).

Liou, K. N., 2002: An Introduction to Atmospheric Radiaton Second Edition, Academic Press.

Loeb N. G. and W. Su (2010), Direct Aerosol Radiative Forcing Uncertainty Based on a Radiative Perturbation Analysis, *J. Climate*, 23, DOI:10.1175/2010JCLI3543.1.

Lyapustin, A., Wang, Y., Laszlo, I., Kahn, R., Korkin, S., Remer, L., Levy, R., Reid, J. S., 2011: Multiangle implementation of atmospheric correction (MAIAC): 2. Aerosol algorithm. *Journal of Geophysical Research: Atmospheres (1984–2012)*, **116**(D3).

Nakajima, T., and M. Tanaka, 1986: Matrix formulation for the transfer of solar radiation in a plane-parallel scattering atmosphere, *J. Quant. Spectrosc. Radiat. Transfer,* **35,** 13-21.

Nakajima, T., and M. Tanaka, 1988: Algorithms for radiative intensity calculations in moderately thick atmospheres using a truncation approximation, *J. Quant. Spectrosc. Radiat. Transfer,* **40,** 51-69.

Nakajima, T., G. Tonna, R. Rao, P. Boi, Y. Kaufman and B. Holben, 1996: Use of sky brightness measurements from ground for remote sensing of particulate polydispersions, *Appl. Opt*., **35**, 2672-2686.

Ogawa, H., Tanaka, M., and Nakajima, T., 1989: A simple expression for the additional sky radiance produced by polarization effects, *Journal of Meteorological Society of Japan*. Ser. II. **67**(5), 877-888.

太田芳文, 江口菜穂, 吉田幸生, 塩見慶, and 中塚由美子, 2006: 第 3 回宇宙からの温室効果ガス観測に関する国際ワークショップ (3 IWGGMS) 参加報告. *天気*, **53**(9), 707-712.

Ota, Y., Higurashi, A., Nakajima, T., and Yokota, T., 2010: Matrix formulations of radiative transfer including the polarization effect in a coupled atmosphere–ocean system. *Journal of Quantitative Spectroscopy and Radiative Transfer*, **111**(6), 878-894.

Phillips, B. L., 1962: A technique for numerical solution of certain integral equation of first kind, *J. Assoc. Comput. Mach*, **9**, 84-97.

Ramanathan V., P. J. Crutzen, J. T. Kiehl, and D., Rosenfeld, 2001: Aerosols, Climate, and the Hydrological Cycle, *science*, **294**, 2119-2124.

Remer, L. A., Y. J. Kaufman, D. Tanré, S. Mattoo, D. A. Chu, J. V. Martins, R.-R. Li, C. Ichoku, R. C. Levy, R. G. Kleidman, T. F. Eck, E. Vermote, **and** B. N. Holben, 2005: The MODIS aerosol algorithm, products, and validation. *Journal of the atmospheric sciences*, 62(4), 947-973.

Rodgers, C. D., 2000: Inverse Method for Atmospheric Sounding, World Sci., Singapore. 240 pp.

Semenov, V. K., Smirnov, A., Aref'ev, V. N., Sinyakov, V. P., Sorokina, L. I., & Ignatova, N. I., 2005. Aerosol optical depth over the mountainous region in central Asia (Issyk‐Kul Lake, Kyrgyzstan). *Geophysical research letters*, **32**(5)

Shettle, E. P., and R. W. Fenn, 1979: Models of aerosols of lower troposphere and the effect of humidity variations on their optical properties. AFCRL Tech. Rep. 79 0214, Air Force Cambridge Research Laboratory, Hanscom Air Force Base, MA, 100 pp.

Shiomi, K., S. Kawakami, and T. Kina, 2010: Operation Results of Initial CAlibration and Validation of "IUBKI", *Aeronautical and Space Sciences Japan,* **58,** 158-163 (in Japanese).

Song, S., Wu, Y., Xu, J., Ohara, T., Hasegawa, S., Li, J., Tang, L., and Hao, J., 2013: Black carbon at a roadside site in Beijing: temporal variations and relationships with carbon monoxide and particle number size distribution. *Atmospheric Environment*, **77**, 213-221.

Soufflet, V., Tanré, D., Royer, A., and O'Neil, N. T., 1997: Remote sensing of aerosols over boreal forest and lake water from AVHRR data. *Remote Sensing of Environment*, **60**(1), 22-34.

Stowe, L. L., R. M. Carey, and P. P. Pellegrino, 1992: Monitering the Mt. Pinatubo aerosol layer with NOAA/11 AVHRR data, *Geophys. Res. Lett.,* **19,** 159-162.

Tanré, D., Kaufman, Y. J., Herman, M., and Mattoo, S., 1997. Remote sensing of aerosol properties over oceans using the MODIS/EOS spectral radiances. *Journal of Geophysical Research: Atmospheres (1984–2012)*, **102**(D14), 16971-16988.

Thuillier, G., M. Herse, D. Labs, T. Foujols, W. Peetremans, D. Gillotay, P. C. Simon, and H. Mandel, 2003: The solar spectral irradiance from 200 to 2400 nm as measured by the SOLSPEC spectrometer from the ATLAS and EURECA missions, *Solar Physics,* **214,** 1-22.

Twomey, S., 1963: On the numerical solution of Fredholm integral equations of the first kind by the inversion of the linear system produced by quadrature, *J. Assoc. Comp. Mach.,* **10**, 97-101.

Yoshida, M., H. Murakami, Y. Mitomi, M. Hori, K.J. Thome, D.K. Clark, and H. Fukushima, 2005: Vicarious calibration of GLI by ground observation data. *IEEE Trans. Geosci. Remote Sensing,* **43,** 2167-2176.

Yoshida, M., Haywood, J. M., Yokohata, T., Murakami, H., and Nakajima, T., 2013: Spatial distribution of dust's optical properties over the Sahara and Asia inferred from Moderate Resolution Imaging Spectroradiometer. *Atmospheric Chemistry and Physics*, **13**(21), 10827-10845.

Yang, P., Liou, K. N., Mishchenko, M. I., and Gao, B. C., 2000: Efficient finite-difference time-domain scheme for light scattering by dielectric particles: application to aerosols. *Applied Optics*, **39**(21), 3727-3737.

Wanner, W., Strahler, A. H., Hu, B., Lewis, P., Muller, J. P., Li, X., Barker Schaaf, C. L., and Barnsley, M. J., 1997: Global retrieval of bidirectional reflectance and albedo over land from EOS MODIS and MISR data: Theory and algorithm. *Journal of Geophysical Research: Atmospheres (1984–2012)*, **102**(D14), 17143-17161.

WCP (World Climate Programme) 1983: Report of the experts meeting on aerosols and their climatic effects, Williamsburg, Virginia, 28-30 March 1983 (Edited by Deepak, A. and H. E. Gerber) WMO-ICSU WCP-55

Wilcox, L. J., Highwood, E. J., & Dunstone, N. J., 2013. The influence of anthropogenic aerosol on multi-decadal variations of historical global climate. *Environmental Research Letters*, **8**(2), 024033.

WMO Global Ozone Research and Monitoring Project Report No. 53, Report of the Eighth Meeting of the Ozone Research Managers of the Parties to the Vienna Convention for the Protection of the Ozone Layer (Geneva, Switzerland, 2 to 4 May 2011) ISBN: 978-9966-20-019-8

Zhang, Y., Yu, H., Eck, T. F., Smirnov, A., Chin, M., Remer, L. A., Bian, H., Tan, Q., Levy, R., Hoben, B. N., and Piazzolla, S., 2012: Aerosol daytime variations over North and South America derived from multiyear AERONET measurements. *Journal of Geophysical Research: Atmospheres* (1984–2012), **117**(D5).